EXPLORING NEW FIELDS

NSK

NSK Technical Journal

Motion & Control
No. 35
June 2024

NSK

Contents

Technical Papers

New Products

Reduction of Cage Noise in Fan Motor Bearings

Masayuki Sato, Takatsune Onozawa
Electrical & Electrification Bearing Technology Center

Abstract

The expansion of the Internet of Things (IoT) and other IT developments in recent years has increased demand for cooling fan motors used in communication base stations and data center server rooms. Bearings for fan motors may generate cage noise (CG noise) due to environmental factors, and though countermeasures exist, their effectiveness has been limited. For this report, we visualized cage whirl, generally considered to be the cause of CG noise, and clarified the correlation between whirl and noise. Furthermore, we reproduced cage whirl by modeling a bearing and conducting a mechanism analysis. Visualization and analysis results were correlated with each other based on the friction coefficient used, suggesting the presence or absence of CG noise can be predicted to some extent. Using this method, we succeeded in developing a prototype cage that does not generate CG noise.

1. Preface

Recent years have seen the development and advancement of 5G communication systems, enabling numerous simultaneous connections and real-time communication from remote locations. The prevalence of IoT in society is also on the rise. The expansion of IoT applications leads to an increase in transmitted data volume, necessitating enhanced high-capacity and high-speed communication capabilities. This, in turn, results in more communication base stations and data center server facilities. The amount of data that servers handle is also growing dramatically, increasing the demand for fan motors to cool the heat generated during calculations.

Bearings for cooling fan motors should be able to withstand higher temperatures and operate at higher speeds to enhance cooling capacity. In addition, there is a universal demand for fan motors that operate with lower power consumption and produce less noise during rotation, especially considering the continuous rotation of multiple fan motors for cooling.

A jarring sound, called CG noise, can occur from the bearings in fan motors, and this is attributed to the cage. CG noise, extensively researched by the bearing industry, is said to be more likely to occur in low-temperature environments.

In 1994, E. Kingsbury et al. conducted experimental studies to observe cage whirl[1], a phenomenon that causes noise, using sensors. The research showed that the mechanism stems from the friction between the balls and the cage. Outer ring rotation was also considered for that paper.

Figure 1 shows the application of this mechanism to a ball guideway cage with the same inner ring rotation as that of a fan motor bearing. In the figure on the left, the cage is tilted toward the upper side, making ball 2 and 4 in contact with the lower side of the pocket, with frictional force pushing the entire cage to the right side. The result is shown in the figure on the right, where ball 1 and 3 now come into contact with the left side of the pocket,

with frictional force pushing the cage downward. This repetition is the mechanism by which the cage whirl in the same direction as the inner ring rotation. Also, Momono's 2001 paper describes CG noise with his views on measures to reduce the clearance between the balls and the pocket[2]. In 2018, Nogi et al. performed an analysis under the same conditions as the experimental results of E. Kingsbury et al. They showed that the whirl of the cage could be reproduced well[3].

In this report, we experimentally and analytically elucidated the phenomenon of CG noise and devised a method to predict the ease of CG noise generation without prototyping and testing.
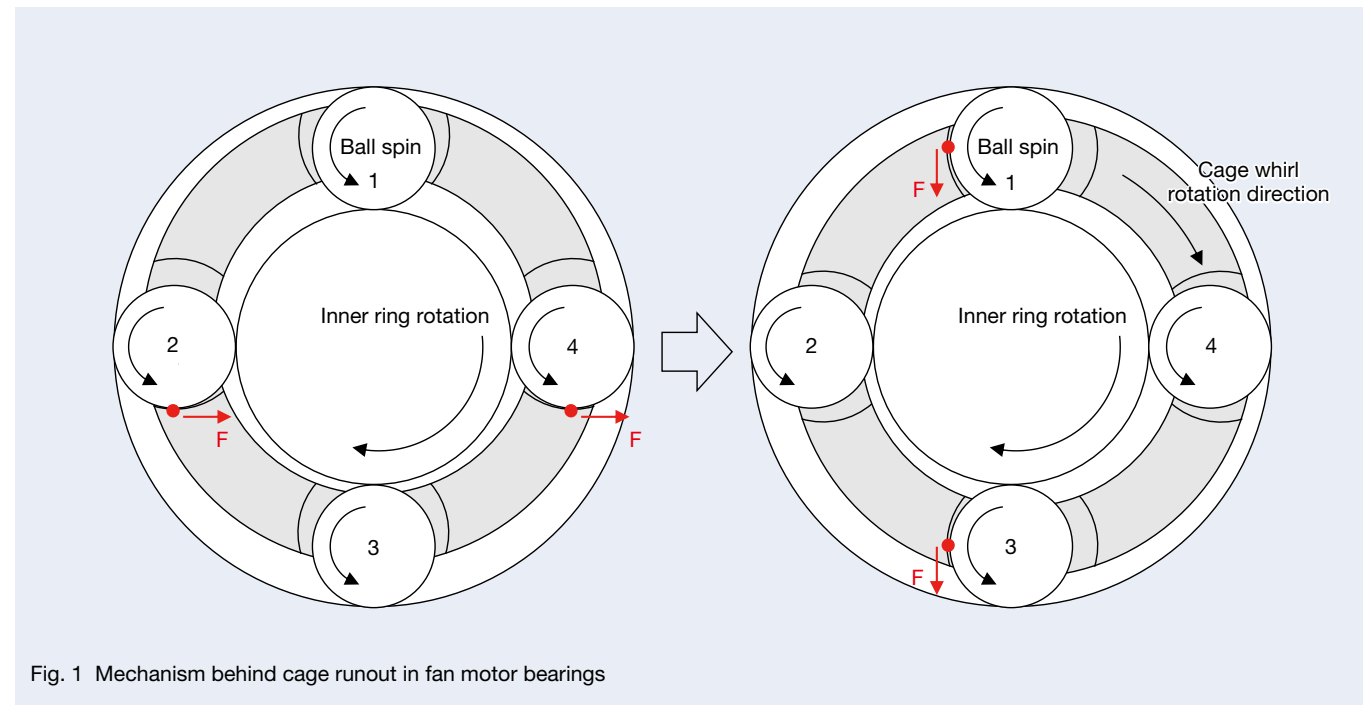

Fig. 1 Mechanism behind cage runout in fan motor bearings

2. Visualization of Cage Behavior

2.1 Configuration of the visualization system

A high-speed camera photographed the bearing incorporated in the fan motor while the cage was generating CG noise, in an attempt to observe the behavior of the cage. Figures 2 and 3 show the configuration of the visualization system. A fan motor was placed in the thermostatic chamber so the bearings were visible, and a microphone was installed to record the noise generated. With the transparent door closed, a high-speed camera photographed the behavior of the cage while adjusting the LED lighting. The outputs of the high-speed camera and the microphone are connected to a data logger. The trigger signal output at the time of shooting is set to start the microphone data collection. This allows synchronization of the microphone signal with the video being shot. Removing the shield on the observation side enabled observation of the fan motor bearings used while filming.

Figure 4 shows the condition of the bearing for observation, with the cage marked in white. Image analysis using these marks elucidated the cage behavior.

For the current operating conditions, it was known that CG noise occurs in the case of grease lubrication but not in that of oil lubrication. Therefore, the support bearing was filled with lubricating oil to prevent CG noise generation.
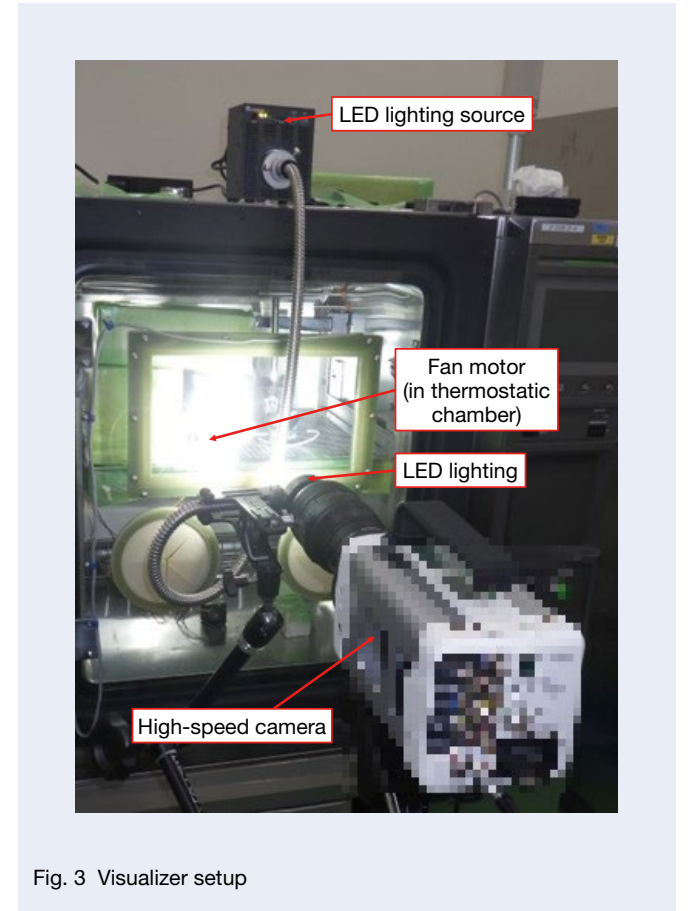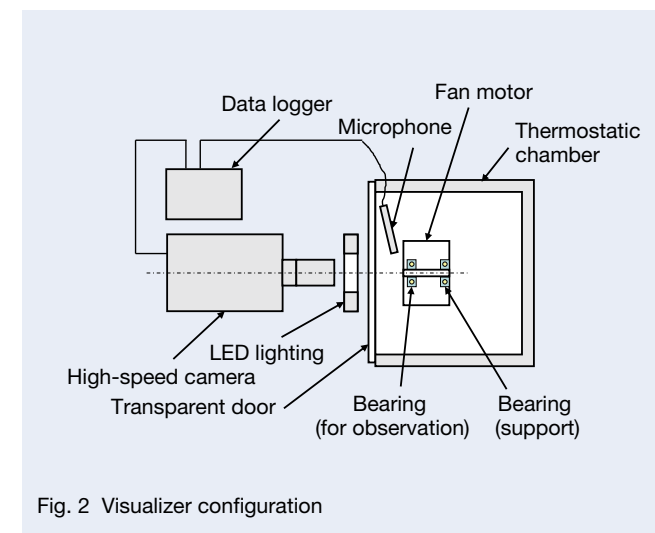

Fig. 3 Visualizer setup

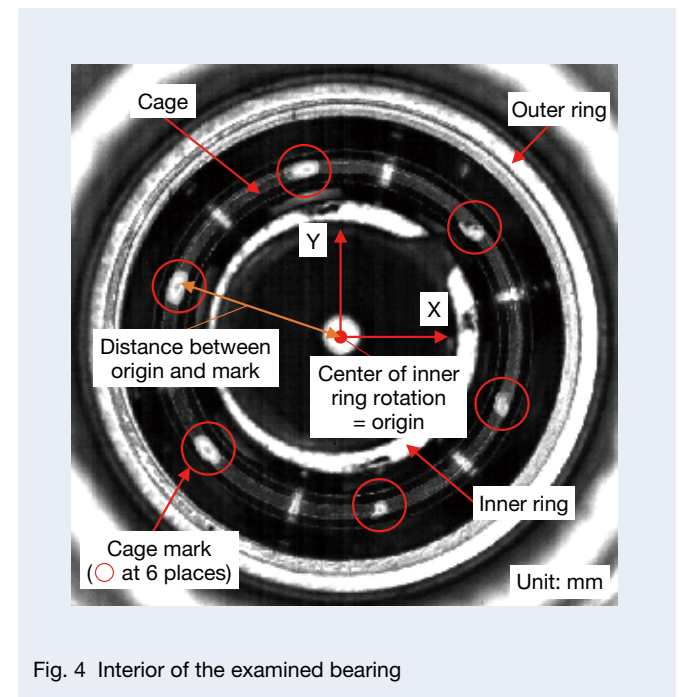Fig. 2 Visualizer configuration

Fig. 4 Interior of the examined bearing

2.2 Visualization results

Table 1 shows an example of the test and recording conditions. A test conducted at a low temperature confirmed continuous or intermittent CG noise from the fan motor. Additionally, it confirmed abnormal cage vibrations in what should be a smooth rotation. Figure 5 shows the image taken. Figure 6 shows the trajectory of the cage mark. Figure 6 (a) shows continuous whirl of the actual trajectory of the cage mark when the bearing in Figure 5 is rotated.

Figure 6 (b) shows intermittent whirl generated in the same test on a cage with different specifications. The trajectories of the other cage marks were similar, indicating that the entire cage was whirling. The whirl was in the same direction as the inner ring rotation (and cage rotation).
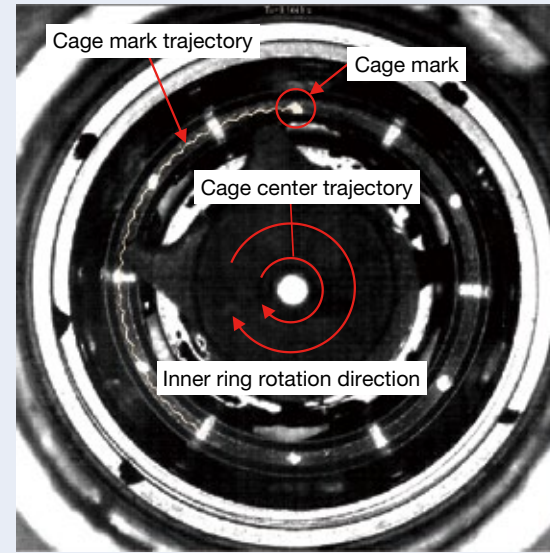

Fig. 5 Video observation

Table 1 Testing and recording conditions

Bearing size	693
Grease base oil	Ester
Grease thickener	Urea
Inner ring speed	11 500 rpm
Preload	3 to 5 N (spring)
Temperature	−20°C
Frame rate	50 000 fps
Shutter speed	1/66 667 sec

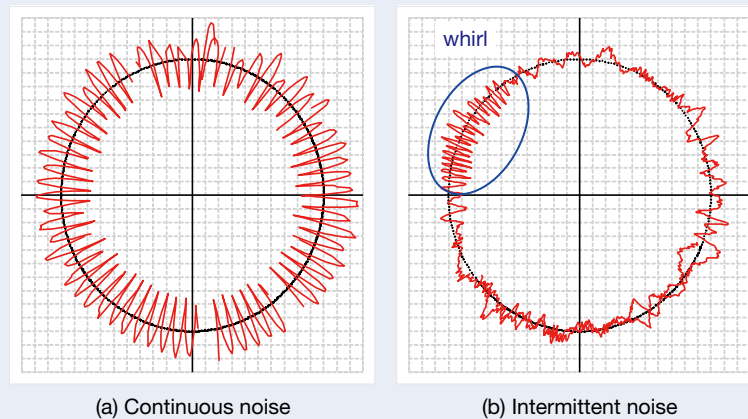(a) Continuous noise   (b) Intermittent noise

Fig. 6 Mark trajectory (magnified)

2.3 Image analysis

To quantify the cage behavior, a coordinate system was created with the origin set at the rotation center of the inner ring, shown in Figure 4, to obtain the barycentric coordinates of the luminance of the cage mark. With these coordinates obtained for each frame, the coordinates of the cage mark were tracked. Figure 7 shows the trajectory of a single cage mark. Figure 7 corresponds to Figure 6 (a). The horizontal axis is time, while the vertical axis is the distance between the origin and the cage mark.

The following formula is used for the distance d.

$$d = \sqrt{X^2 + Y^2}$$

FFT processing of the time waveform yielded the amplitude and frequency of the vibration.

Figure 8 shows the microphone output acquired simultaneously. Comparing Figures 7 and 8 indicated the agreement between the whirl frequency of the cage and the noise frequency. Therefore, it was found that CG noise is heard when the cage vibration vibrates the air. The same test was conducted for other cages, as described in detail in Section 2.4, showing the consistency between the cage whirl frequency at the noise occurrence and the noise frequency. The frequency of CG noise and whirl varied with the type of cage. However, it was high in relation to the inner ring rotational speed, ranging from 1 000 to 12 000 Hz (5 to 55 times the inner ring rotational speed).

2.4 Relationship between the cage whirl and noise

The same experiments were conducted as before, with the cage shape and grease changed to prevent CG noise. Figure 9 plots the amplitude (mm) and frequency (Hz) of the vibration for several combinations of cages and grease. Cage A is the standard cage we have been discussing in the examples. If hearing recognizes noise, it was marked as ×. If not, it was marked as ○. The figure shows that the higher the amplitude and frequency of the vibration, the more likely the CG noise is recognized as noise. The red dashed line in this plot shows a threshold for the presence or absence of noise.
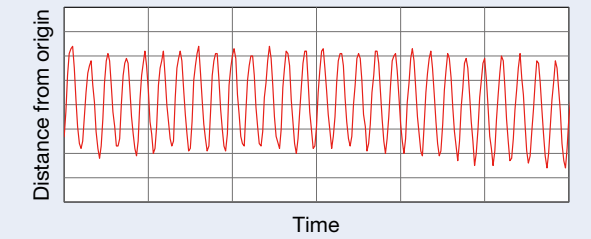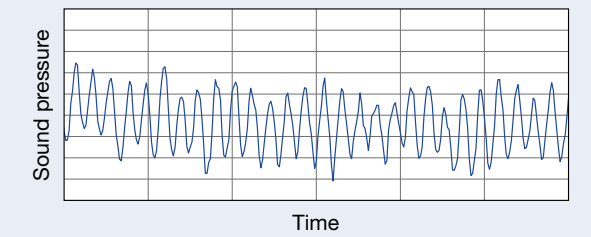

Fig. 7 Change in cage mark position

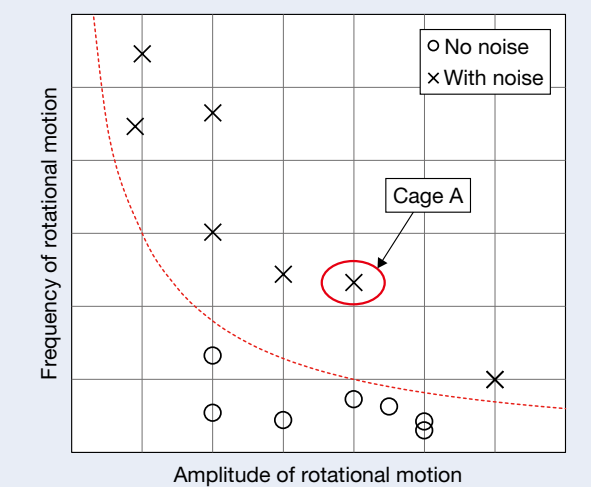Fig. 8 Variation in microphone output

Fig. 9 Relationship of generated noise and frequency to amplitude of rotational motion

3. Mechanism Analysis of Cage Behavior

3.1 Mechanism analysis model

Section 2 shows that the cause of the CG noise is the cage whirl and that noise is not recognized if the amplitude and frequency of the whirl are small or if the whirl does not occur. However, since prototype making and experimental confirmation would be time consuming and costly, so we tried a prediction based on mechanism analysis. Mechanism analysis, creating a CAD model behaving in the same way as it actually does, can analyze displacement, load, and stress of an arbitrary part.

Analyzing the mechanism revealed the trajectory of the cage's barycenter. The analysis, presented in Figure 10 and Table 2, simulated a bearing model identical to the actual one in terms of dimensions and geometry, subjecting it to the same rotational speed and preload. The outer ring was fully restrained, and the inner ring was rotated under preload.
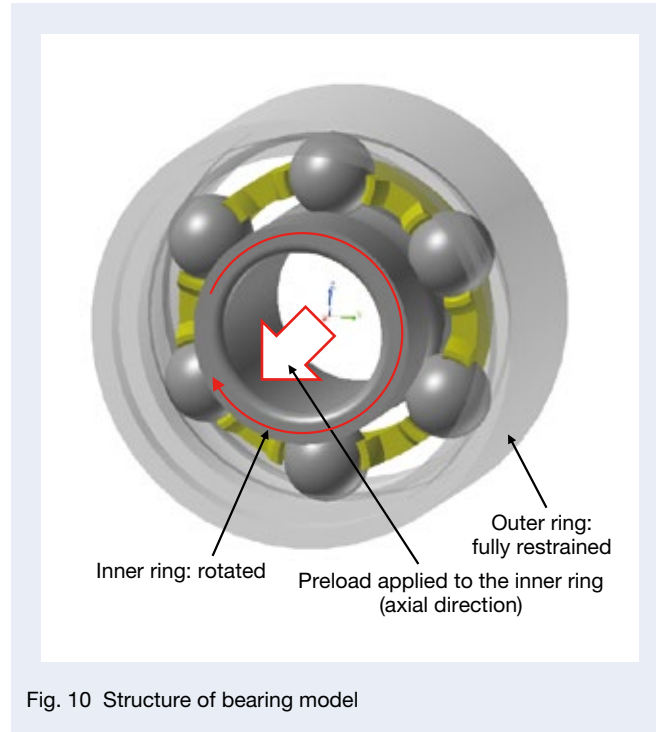
3.2 Mechanism analysis results

Actual whirl tends to occur at low temperatures. This can be explained as follows. Low temperatures can cause the grease to harden, hindering its flow into the cage pocket. This results in increased friction between the balls and the pocket. Scanning the friction coefficient and analyzing the calculated whirl motion demonstrated a clear link: increased whirl with a higher friction coefficient. Figure 11 plots the amplitude and frequency of whirl revealed in the analysis of the model of cage A with varying friction coefficient μ. The red dotted line in Figure 9 represents noise presence/absence. The analysis was performed with five levels of friction coefficients from a to e. When the friction coefficient was less than μ:c, the frequency was low and varied widely. However, when the friction coefficient exceeded μ:d, the frequency changed little but was significantly higher.

Fig. 10 Structure of bearing model

Table 2 Analysis conditions

Bearing size	693 (same as actual)
Inner ring speed	11 500 rpm
Outer ring speed	0 rpm (fully restrained)
Preload	5 N
Analysis speed	50 000 fps
Rigidity of each component	Rigid body model
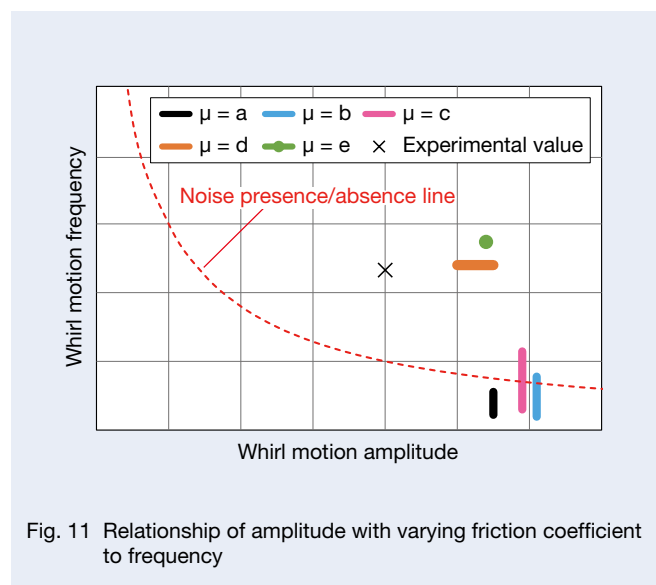
Fig. 11 Relationship of amplitude with varying friction coefficient to frequency

Figure 12 shows the results of the mechanism analysis, where the horizontal axis is the friction coefficient and the vertical axis is the amplitude × frequency of whirl. The red dotted line indicates the tentative noise presence/absence line in Figure 9.

As can be seen from the graph, increasing the friction coefficient used in the analysis increases the amplitude × frequency of whirl, and the noise becomes more likely to occur. In the actual measurement, the amplitude × frequency of the whirl was in the range shown in blue in Figure 12, which is consistent with the analytical results with the friction coefficient set to μ:d. Figure 13 shows the analytical results with a friction coefficient set to μ:d. The vertical axis is the Y-directional displacement of the cage barycenter (mm), and the horizontal axis is the time (sec), corresponding to Figure 7 in the experiment. The amplitude and frequency close to the actual whirl were reproduced. In this example, the analysis results agreed not only with the experimental data around μ:d but also with that around μ:d for the other cages. This mechanism analysis therefore offers a powerful tool for developing new cages, and it allows designers to predict noise presence or absence without the need for prototyping and experimentation.
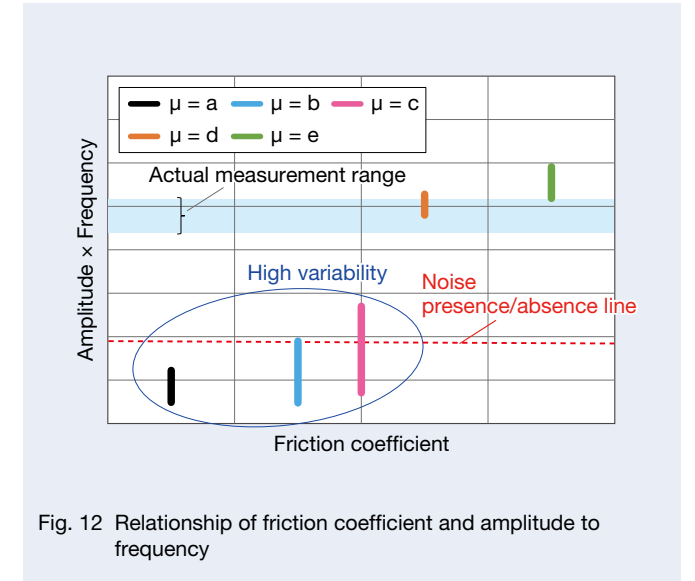
Fig. 12 Relationship of friction coefficient and amplitude to frequency
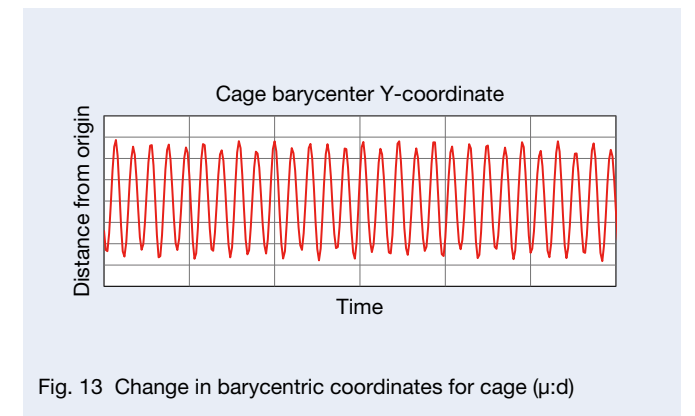
Fig. 13 Change in barycentric coordinates for cage (μ:d)

4. Low Noise Cage Development

An investigation of the low-noise cage was also conducted. Figure 14 shows the pocket shape of the conventional single spherical surface we have used as an example. Figure 15 shows the pocket shape of the low-noise-cage.

The cage has the curvature of the pocket surface increased relative to the ball diameter in order to suppress friction between the balls and cage. To prevent the gap between the balls and the pocket from widening, the pocket surfaces have an elongated sphere. The centers of the right and left radii of the pocket surfaces are offset in the circumferential or radial direction, respectively. Rotation around a virtual line connecting the intersection of the right and left radii and the cage center axis forms an elongated sphere. Compared to a conventional product, the pocket surface of the low-noise cage has a shape in which the gap between the ball and the pocket surface increases in the direction toward the inner and outer diameters, facilitating the flow of lubricant into the pocket. Furthermore, the ball is less likely to come into contact with the edges of the inner and outer diameter side of the pocket. This prevents scraping of the lubricant and suppresses the increase in frictional force on the pocket surface.
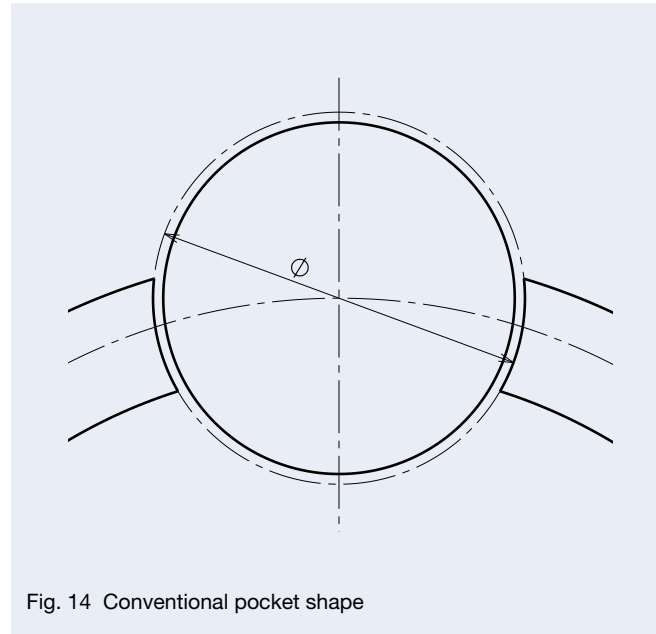
Fig. 14 Conventional pocket shape
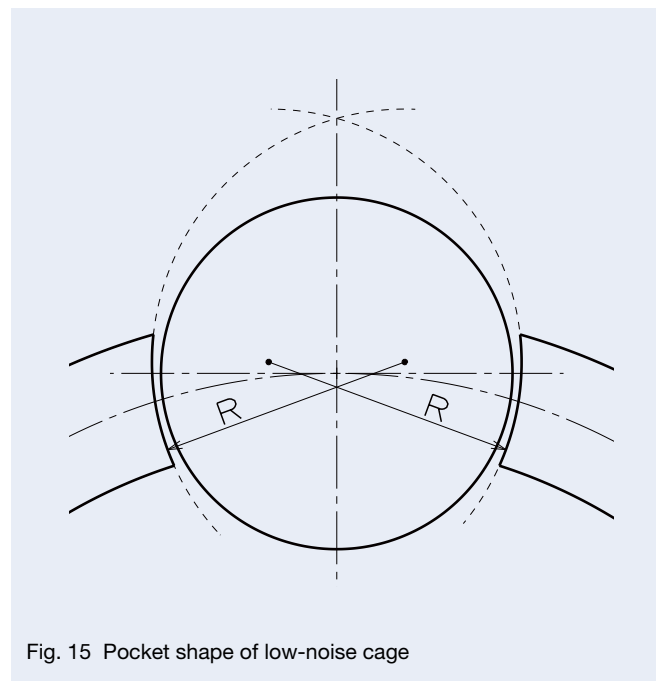
Fig. 15 Pocket shape of low-noise cage

Figures 16 and 17 are the results of the mechanism analysis using the same low-noise cage as that shown in Figures 11 and 12. The amplitude and frequency of the low-noise cage are reduced compared to the conventional cage, and μ:d is below the threshold for noise generation, suggesting the possibility of suppressed noise. Figure 18 shows the change in the barycentric coordinates of the cage, as in Figure 13. Compared to Figure 13, the whirl is clearly not stable. This time, to confirm the correctness of the analysis, a low-noise cage prototype was produced. Figure 16 shows the experimental results as white circles. The amplitude and frequency of the whirl were suppressed beyond the analysis prediction, and no noise was detected.
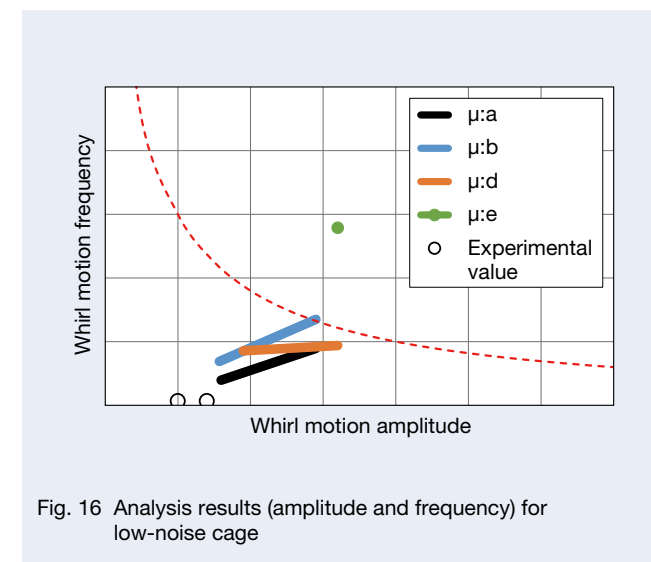
Fig. 16 Analysis results (amplitude and frequency) for low-noise cage
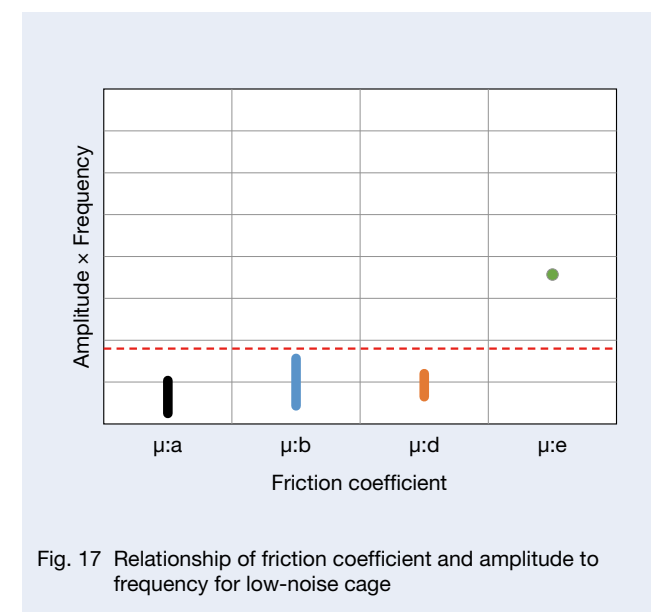
Fig. 17 Relationship of friction coefficient and amplitude to frequency for low-noise cage
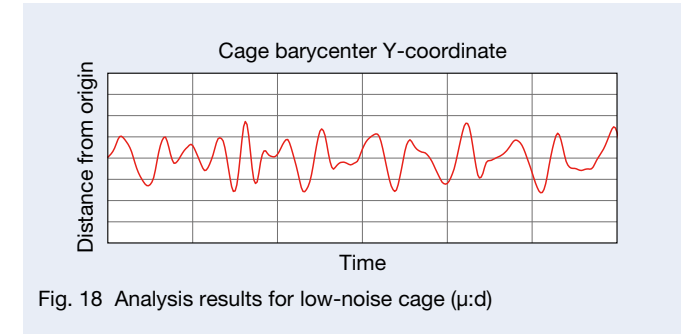
Fig. 18 Analysis results for low-noise cage (μ:d)

5. Summary

In this report, we observed the behavior of the bearing retainer for fan motor bearings where CG noise is occurring. It was clear that cage whirl was occurring and generating CG noise. Next, we conducted a test for various types of cages and found the amplitude and frequency identified as cage noise. By analyzing the mechanism, we also devised a method to reproduce the cage behavior when CG noise is generated and to predict the presence or absence of CG noise without prototyping or experimentation. Using this method, we succeeded in developing a bearing that can reduce CG noise.

References

1) E. Kingsbury and R. Walker, "Motions of an Unstable Retainer in an Instrument Ball Bearing," *Transactions of the ASME*, Vol. 116 (April 1994), pp. 202–208.
2) T. Momono and B. Noda, "Sound and Vibration in Rolling Bearings," *NSK Technical Journal,* No. 661 (1996), pp. 13–22.
3) Takashi Nogi, Kazuaki Maniwa, and Noriko Matsuoka, "A Dynamic Analysis of Cage Instability in Ball Bearings," *Transactions of the ASME* Vol. 140 (January 2018), 011101-1/12.

Masayuki Sato

Takatsune Onozawa

Condition Monitoring Solution

Nozomu Harada, Akihide Sakano
Industrial Machinery Business Division Headquarters
Condition Monitoring System Division Headquarters CMS Development Center

Abstract

Digital technologies are increasingly being used to realize a sustainable society based on the concept of a circular economy. For industrial machinery, condition monitoring has been used to maintain equipment and reduce unexpected downtime, and these capabilities are expected to play a key role as essential technologies for circular economies. This article introduces the condition monitoring technologies and solutions of Brüel & Kjær Vibro (BKV), which joined the NSK Group in 2021.

1. Preface

NSK has set a goal of achieving carbon neutrality by 2035 in order to realize a sustainable society and is promoting various initiatives (Figure 1) from the perspectives of "making" (technology development and production) and "using" (products and services).

NSK's Product Lifecycle Management (PLM) strategy represents this from the perspective of its business activities in the industrial machinery field. The PLM provides various values to end users' "use" beyond the conventional business that focuses on product sales. It also contributes to the efficiency of end users' use of the equipment and utilization of resources by detecting equipment problems through condition monitoring, proposing on-site actions based on a diagnosis of deterioration and remaining service life through analysis, and proposing optimal maintenance such as product repairs and replacement. Furthermore, the discovery of new issues and the creation of new technologies based on the data obtained here are expected to improve products and production further.

Brüel & Kjær Vibro (hereinafter BKV), which has more than 30 years of achievements in the field of condition monitoring, an important part of PLM, was added to the NSK Group in 2021. By combining its technological and business experience and achievements with NSK's tribology-based product technology and business footprint, NSK is creating and proposing new value to society. This report introduces BKV's condition-monitoring technology and the condition-monitoring solutions that are based on that technology.

2. Brüel & Kjær Vibro (BKV)

BKV is one of the world's top ten condition monitoring service providers, with more than 30 years of experience in condition monitoring for critical infrastructure such as wind power generation and petrochemical plants. It provides condition monitoring solutions with its products and technical services, from its production and development bases in Germany, where the company is headquartered, and in the United States, as well as a service structure centered on a remote monitoring center in Denmark.

Environmental contribution using "tribology"

Deepen tribology technology to realize further energy savings For example, development of electrical impedance method* using electrical circuit to visualize the inside of bearings ⇒ Contribute to reducing torque by making oil film as thin as possible

*Received Best Paper Award, Japanese Society of Tribologists

The oil film thickness is calculated by measuring the ease with which an electrical current flows.

Reducing CO_2 emissions from business activities

Reduce CO_2 emissions from business activities through three measures: energy saving, technological innovation, and renewable energy

Coating plant roofs with thermal insulation paint

Improving efficiency of heat treatment

Adopting renewable energy

Environmental contribution utilizing CMS/reconditioning

Improve reliability and conserve resources by utilizing product lifespan diagnostics, condition monitoring system (CMS), and repair

Conserving resources by repairing and reusing products that are typically discarded after use

Benefit the environment through our products

Contribute to reducing CO_2 emissions of society as a whole by providing environmentally-friendly products

Low-friction hub unit bearings

Ultra high-speed ball bearings for EV motors

Bearings for wind turbine gearboxes

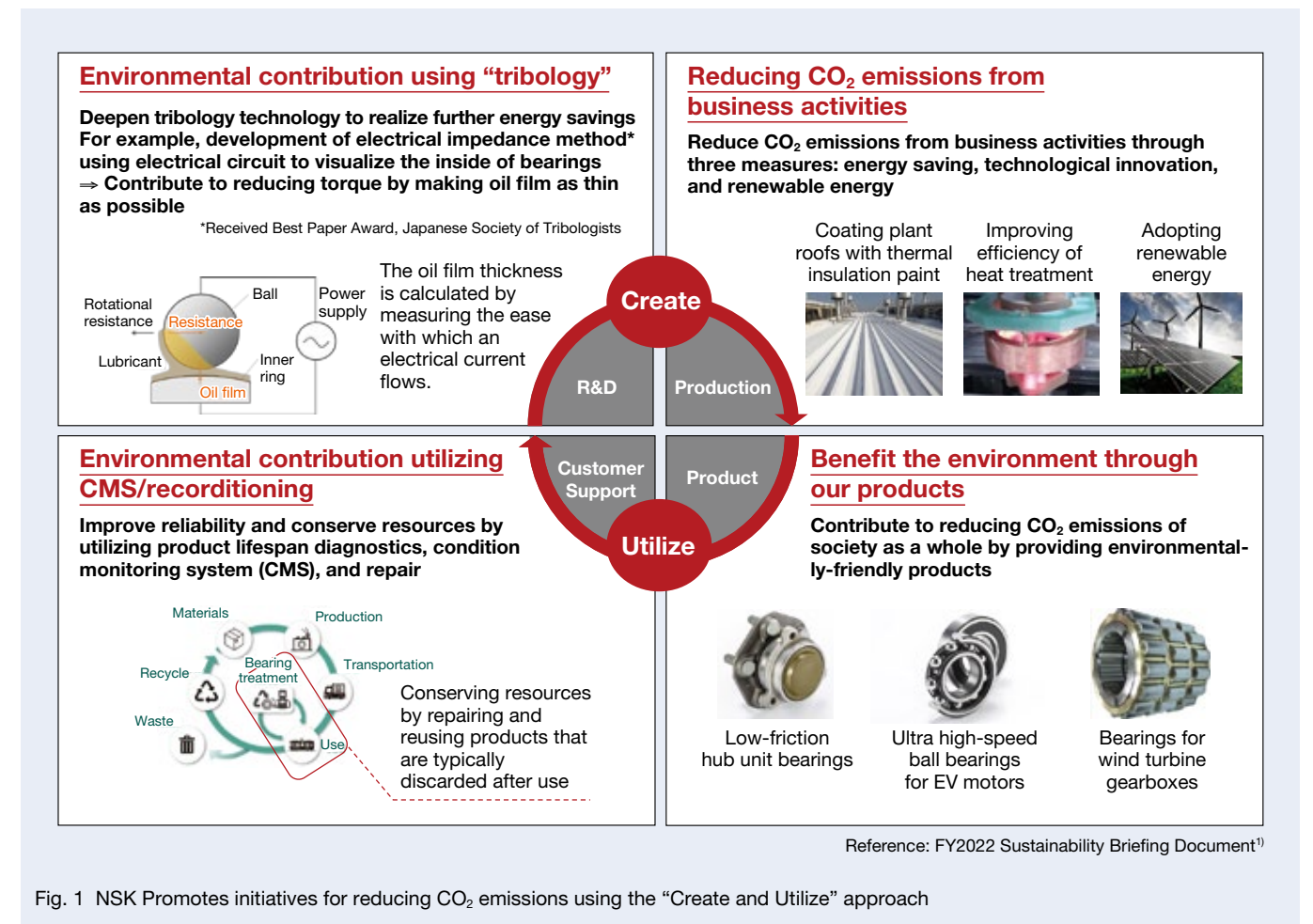Reference: FY2022 Sustainability Briefing Document[1]

Fig. 1 NSK Promotes initiatives for reducing CO_2 emissions using the "Create and Utilize" approach

3. Condition Monitoring Technology for BKV

3.1. Monitoring and diagnostic technology

Sensors measure vibrations generated mainly from machinery and capture changes in indicators (descriptors) derived using mathematical processing to monitor the condition of machinery equipment (Figure 2). When signs of abnormality are detected, the condition of the machinery equipment is diagnosed in detail using time waveform analysis and frequency analysis. The system targets problems in all machinery equipment, such as

deterioration and damage of not only rolling bearings but also elemental parts such as sliding bearings and gears, and components such as motors and gearboxes, as well as faulty assembly and installation of these components.

Diagnosing the conditions of rotating machinery by vibration has a long history and is established as an international standard. BKV has contributed to the development of international standards (ISO 16079-1, 2, and ISO 19283). It is also an educational institution for machine condition monitoring and diagnostic technicians, providing training globally by licensed individuals at the highest level of Cat. IV.
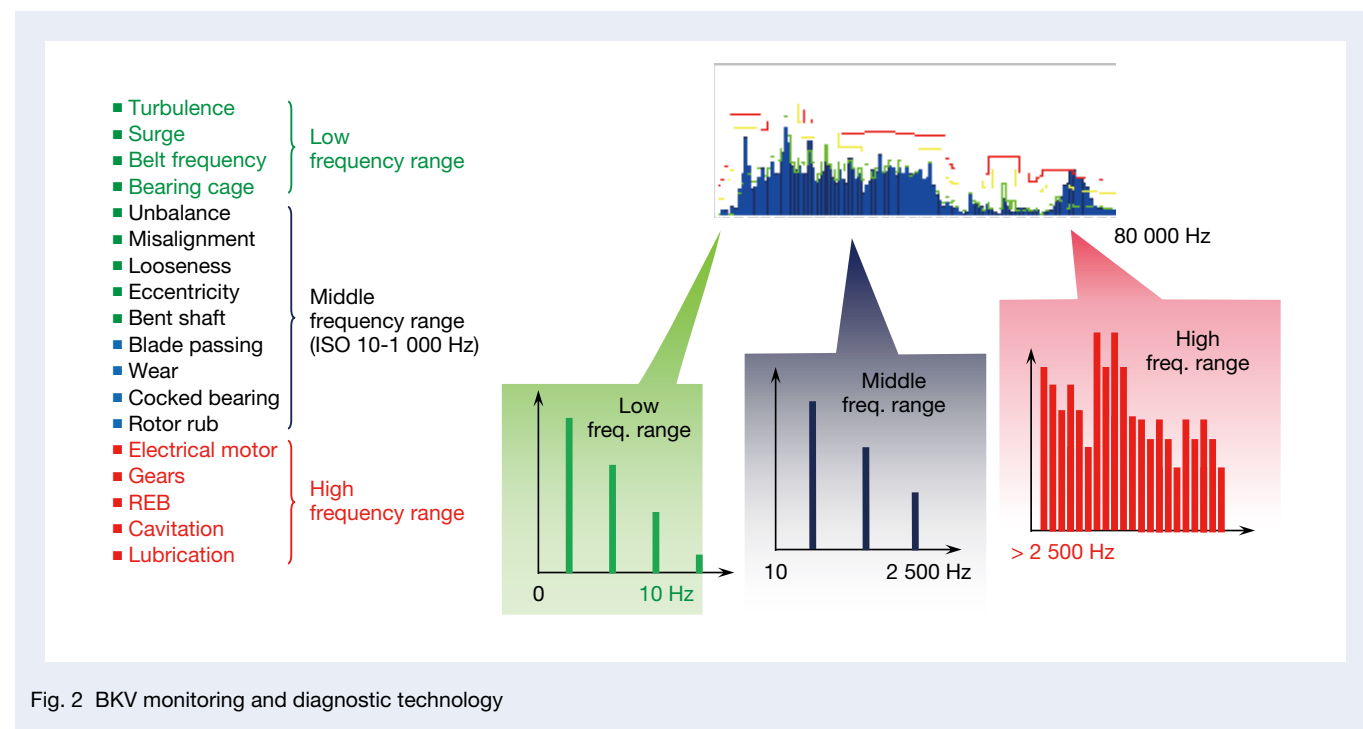

Fig. 2 BKV monitoring and diagnostic technology

3.2 Product technology

BKV develops products and provides services according to the importance of the equipment (Figure 3). The most critical facilities that have a large impact on society or require very high restoration costs need a Machine Protection System (MPS) that can immediately stop the equipment after detecting an abnormality. VC-8000 and other products are provided mainly to petrochemical plants. The system is designed based on the PI System™ (AVEVA), a standard backbone system for this industry[2], and is analyzed by the software SETPOINT, which incorporates the monitoring and diagnostic technologies mentioned above.

Critical equipment with high restoration costs and general equipment that aims at labor saving and stabilization through the use of IT technology require condition monitoring systems for predictive maintenance based on diagnosis through constant monitoring. The product range includes the DDAU III for wind turbines and VCM-3 for general industrial machinery. These systems are similarly designed based on the linkage with the backbone and control systems of the equipment.

VibroSuite is provided for wind power generation, the company's core business. This monitoring and diagnostic software has been developed specifically for BKV's remote monitoring team.

These monitoring devices are similar to edge devices and are equipped with a CPU that digitizes analog signal input from various sensors, calculates index values for monitoring and diagnosis internally, and then transmits the data to the backbone system. This reduces the number of transmissions of large vibration waveform data to the backbone system for detailed analysis, thereby reducing communication and calculation costs.

For other general equipment, NSK offers the VST-100, a handheld device for predictive maintenance through periodic patrol monitoring. This involves capturing and managing data when customers regularly visit and inspect their equipment, and NSK's Wireless Vibration Diagnostic Device is in this category.

NSK also produces its own sensors for vibration measurement and develops them according to the environment in which the equipment is used, with consideration for temperature and humidity.
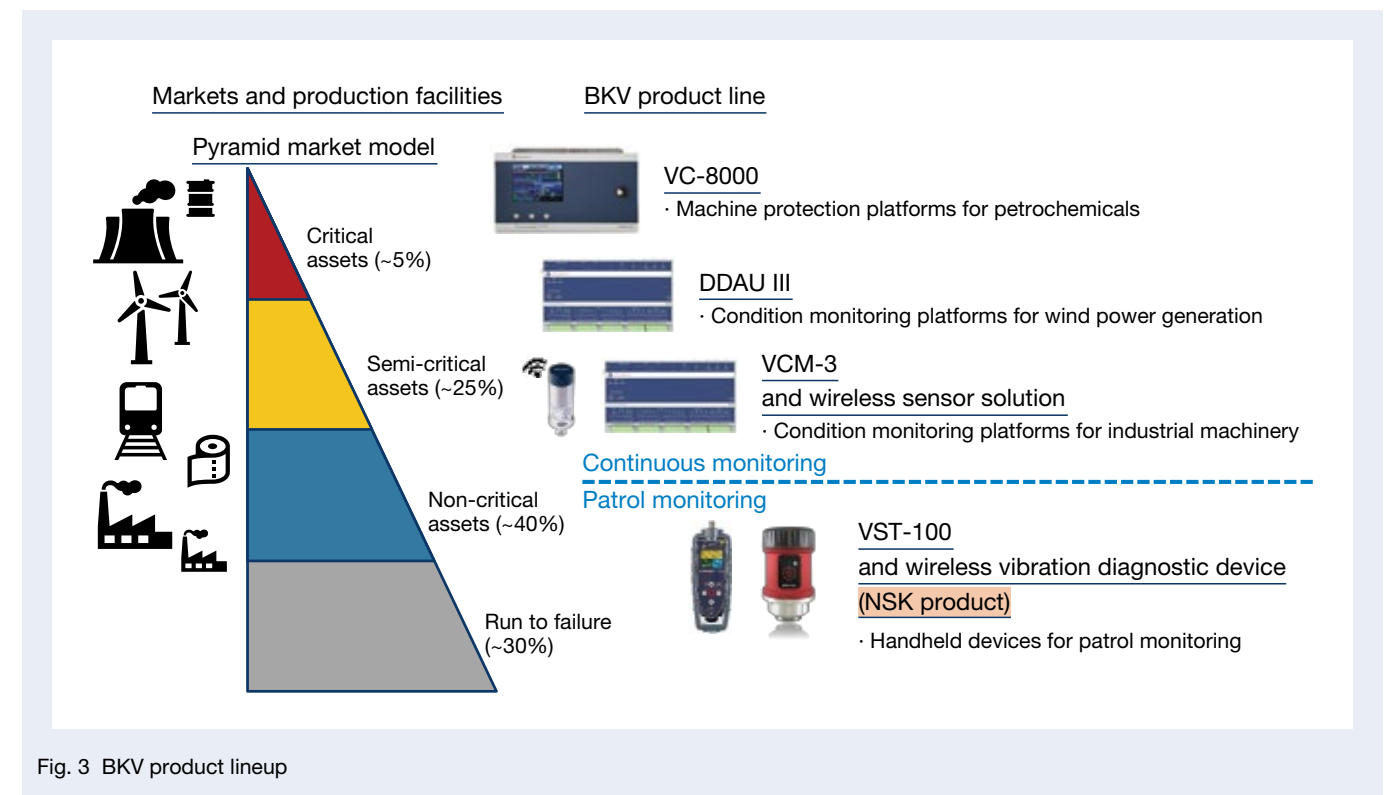

Fig. 3 BKV product lineup

3.3 Engineering technology

Installing a condition monitoring system requires a certain level of monitoring and diagnostic technology. For this reason, the company also supports system integration, from specification studies for appropriate condition monitoring and installation of equipment to startup. For large plants with more than 100 monitoring devices, the customer installs the monitoring system. We also provide installation training for the customer's staff.

After the condition monitoring system is installed, the company provides remote monitoring services upon customer request. This includes monitoring data sent from the monitoring devices 24 hours a day, 365 days a year, and issuing alarm reports that offer suggestions for actions to be taken by on-site workers after detailed analysis of automatically detected abnormalities by diagnostic technicians.

4. Condition Monitoring Solutions

Condition monitoring solutions provided by condition monitoring technologies, products, and services allow for the early detection of potential failures in plants, machinery equipment, and mechanical components and effective predictive maintenance. In this section, we introduce condition monitoring solutions for wind power generation and petrochemicals.

4.1 Wind power generation

Wind turbines are often affected by fluctuating loads due to changing weather conditions, which accelerate the deterioration of mechanical components. Condition monitoring is therefore necessary to achieve the required uptime. Monitoring wind turbines requires early damage detection, achieved by taking into account low-speed rotation, complex gearbox structures, low-stiffness foundations, and constantly changing wind conditions. In addition to identifying the site and type of damage, the severity of the damage must also be diagnosed in order to estimate the lead time to maintenance.

As shown in Figure 4, BKV performs the condition monitoring using a monitoring device installed in the wind turbine nacelle, which collects and analyzes vibration data from the drive train, consisting of a main shaft bearing, gearbox, and generator, and from acceleration sensors installed on the tower. The results of the analysis are transmitted via the Internet to a remote monitoring center in Denmark. Since the load on each part of the system varies according to changes in wind conditions, BKV monitors and analyzes the data by power output, makes a comprehensive diagnosis based on these results, and issues an alarm report. Diagnostic results are expressed in five levels of severity, and a timeframe is defined according to the severity (e.g., within two weeks for severity 2). The report also suggests actions that should be taken, such as an immediate internal inspection of the high-speed stage of the gearbox or careful observation of the intermediate shaft side gears. The remote monitoring service by BKV is optional. It can be provided by the user or by the wind turbine builder or maintenance service provider.

To date, approximately 40 000 BKV condition monitoring systems have been installed on wind turbines worldwide, and remote monitoring services have been provided for more than 10 000 of them.

4.2 Petrochemicals

In petrochemical plants, especially in natural gas liquefaction processes, equipment is subjected to extreme operating conditions. Refrigerant compressors, pumps, and hydraulic turbines undergo severe thermal expansion during startup and full production at cryogenic temperatures, and bearings and other mechanical components are subjected to extreme loads during startup and shutdown. The process also involves a variety of equipment operating at different speeds and load conditions, so even small variations in natural gas composition can have a significant impact on the entire facility. Minimizing the unplanned downtime of the most critical equipment beyond routine inspections and maintenance requires a condition monitoring solution— that is, a machine protection system—to detect initial anomalies early and automatically shut down the equipment.

Figure 5 shows an overview of the condition monitoring solution for petrochemical plants. The main shafts of machinery equipment used in petrochemical plants, such as refrigeration compressors for the liquefaction process, are mainly supported by sliding bearings. Shaft vibration measurement is necessary for monitoring and diagnosing sliding bearings, and displacement sensors are used. The specifications and installation requirements for sensors are standardized in API 670 of the American Petroleum Institute, and BKV's products also conform to this standard. Similarly, monitoring equipment conforms to API670. This satisfies various regulations such as measurement accuracy, time from abnormality detection to alarm operation, and redundancy of power supply.

For large projects, more than 100 monitoring devices are installed. To date, approximately 10 000 BKV condition monitoring systems have been installed in petrochemical plants worldwide.

(a) System architecture

(b) Monitoring method based on generator power

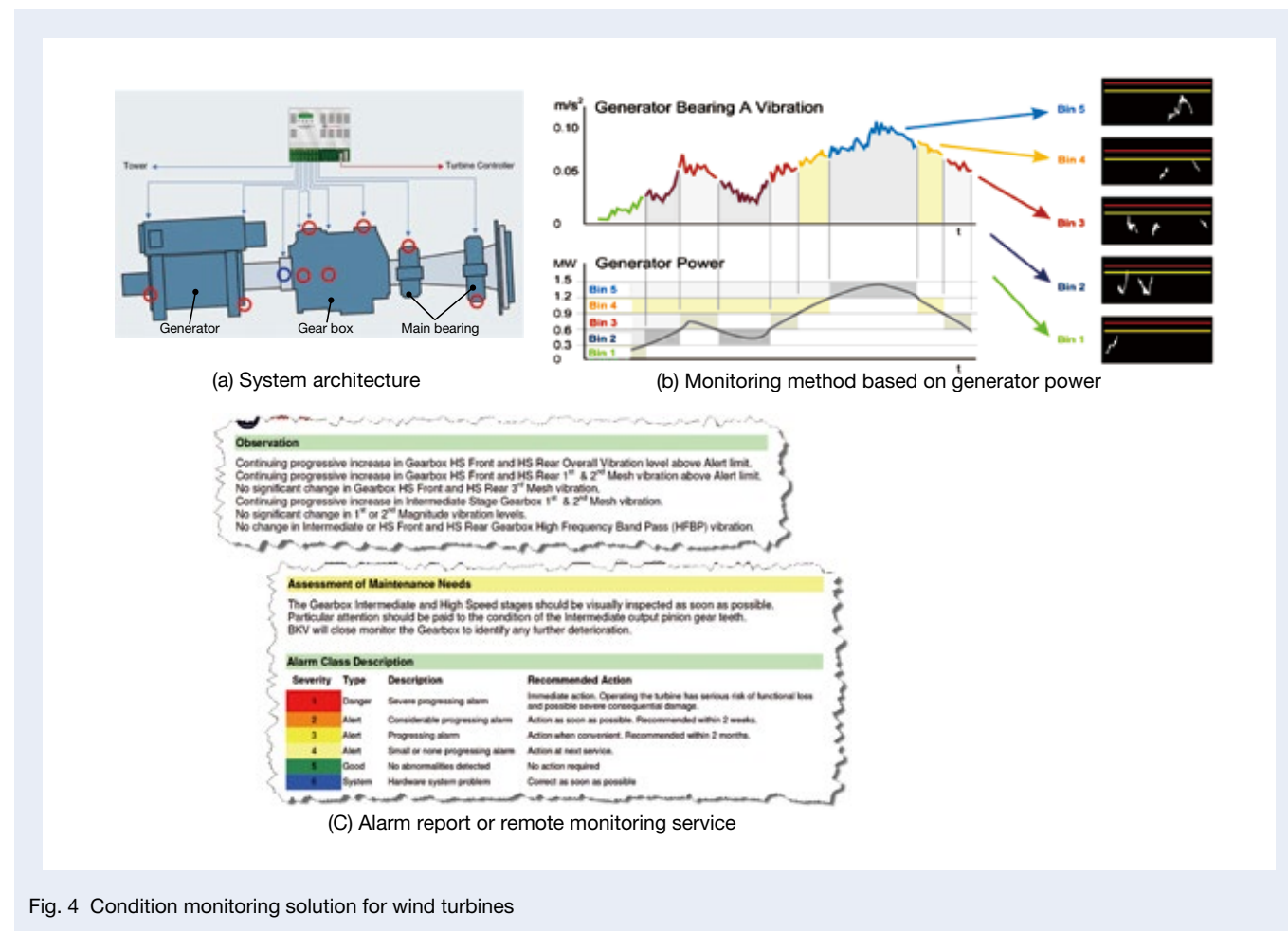(C) Alarm report or remote monitoring service

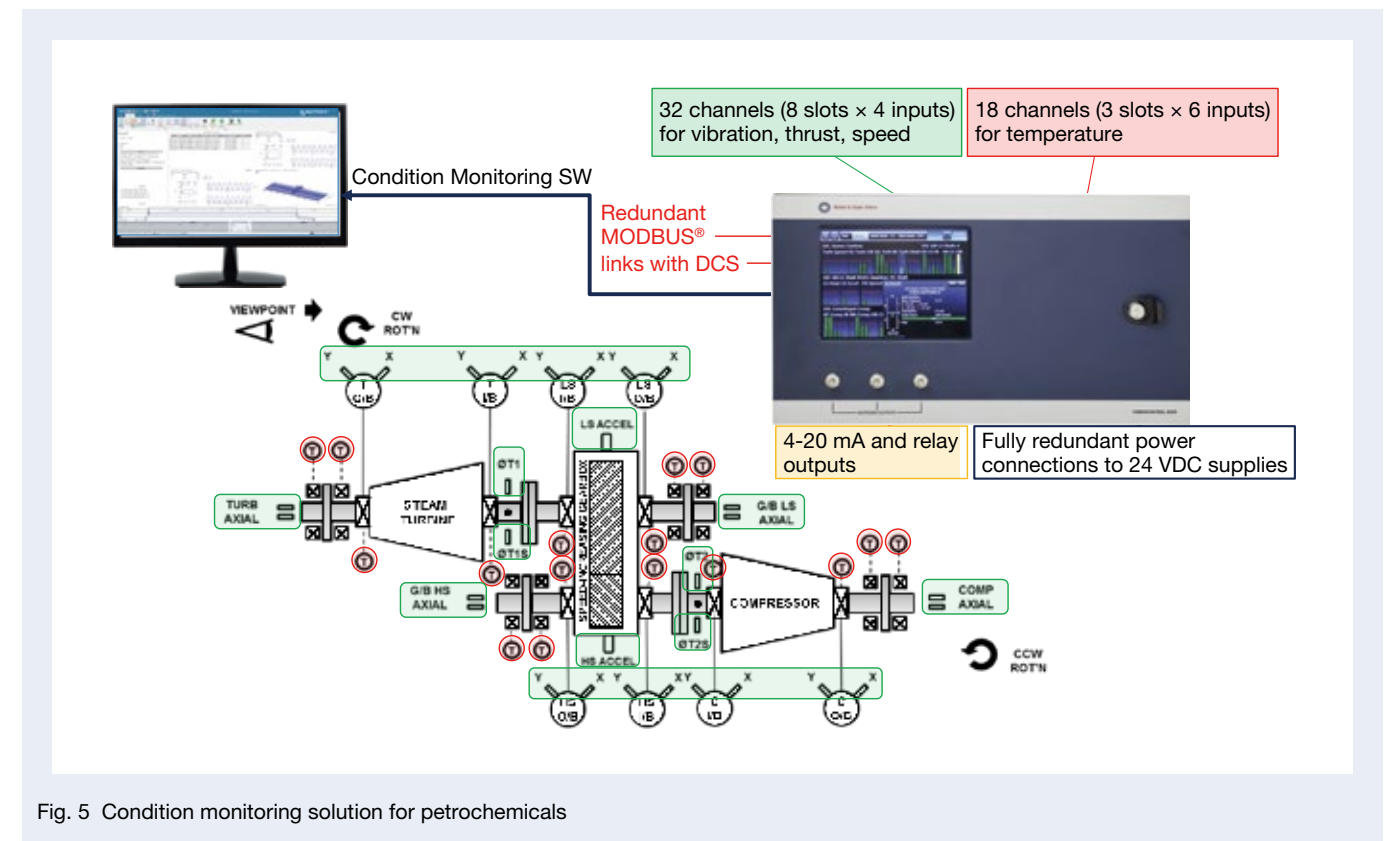Fig. 4 Condition monitoring solution for wind turbines

Fig. 5 Condition monitoring solution for petrochemicals

5. New Technology and Product Development

BKV's conventional products and services have been mainly designed for critical infrastructure facilities. They required expertise in machinery equipment as well as advanced knowledge and technology related to condition monitoring. However, these products and services are expected to be more user-friendly and flexible, as requirements will be a barrier to the introduction of BKV in new markets, where demand for condition monitoring is anticipated. In response, we launched BKV Beyond in 2023. This condition monitoring solution combines wireless sensors for easy installation in machinery equipment with a cloud-based condition monitoring infrastructure.

Moreover, NSK is developing the Condition Monitoring System for Linear Motion Machinery, which implements NSK's diagnostic technology for linear motion machinery into BKV's condition monitoring solution for rotating machinery. The objective is to expand the scope of application from process plants, which have mainly handled condition monitoring, to processing and assembly plants, primarily for machine tools and transport machinery. The rapid IT expansion is driving the joint development of BKV in Europe and NSK in Japan, as well as business development by integrating the global customer networks of both companies.

5.1 Cloud-based condition monitoring solution

Figure 6 shows the BKV Beyond system configuration. The use of wireless sensors facilitates monitoring in large-scale environments through mesh network technology. BKV Beyond also incorporates a 3-axis accelerometer that analyzes vibration data up to 6.3 kHz and transmits the data to the cloud. The software on the cloud sets up the condition monitoring, and workers perform the installation according to the setting information via an application on a mobile terminal. The remote monitoring system uses AI to detect condition changes automatically. All notifications are also reviewed by a vibration diagnostician, who performs a detailed diagnosis and suggests a response to the on-site maintenance team. The combination of cloud and AI improves the accuracy of diagnosis on a daily basis, and new technologies and capabilities are provided as needed.
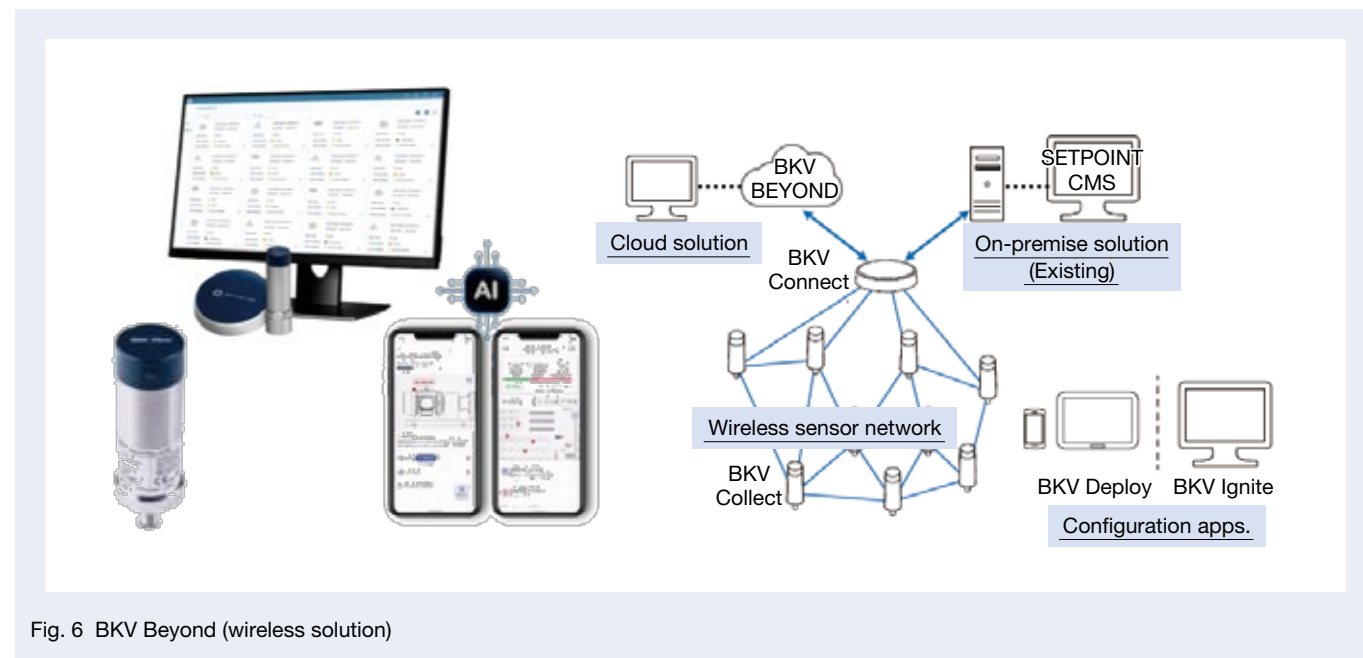

Fig. 6 BKV Beyond (wireless solution)

5.2 Condition monitoring system for linear motion machinery

In power generation facilities and process plants, machinery equipment operates under constant conditions for long periods, so condition monitoring is performed at regular intervals. In processing and assembly plants, machinery equipment is repeatedly operated and stopped in a complex machining process, to which condition monitoring must correspond. As shown in the system configuration of the condition monitoring system for linear motion machines in Figure 7, the condition monitoring device VCM-3 works with machine tools and other machinery equipment to perform measurements under conditions appropriate for condition monitoring. The VCM-3 is also equipped with a diagnostic algorithm developed based on NSK's tribology technology to detect deterioration and damage of ball screws and linear guides. These represent some of the new value propositions that result from the synergy of BKV's condition monitoring products and technologies and NSK's achievements and technologies in linear motion machinery.

6. Postscript

This article introduces the condition monitoring technology of Brüel & Kjær Vibro, which joined the NSK Group in 2021. NSK has been providing reliable condition monitoring solutions to customers who deal with critical infrastructure equipment and will propose this technology to customers involved with NSK to expand the possibilities of condition monitoring. Furthermore, NSK will contribute to the sustainable development of society by creating new value through the fusion of NSK's tribology technology and new condition monitoring technology.

References

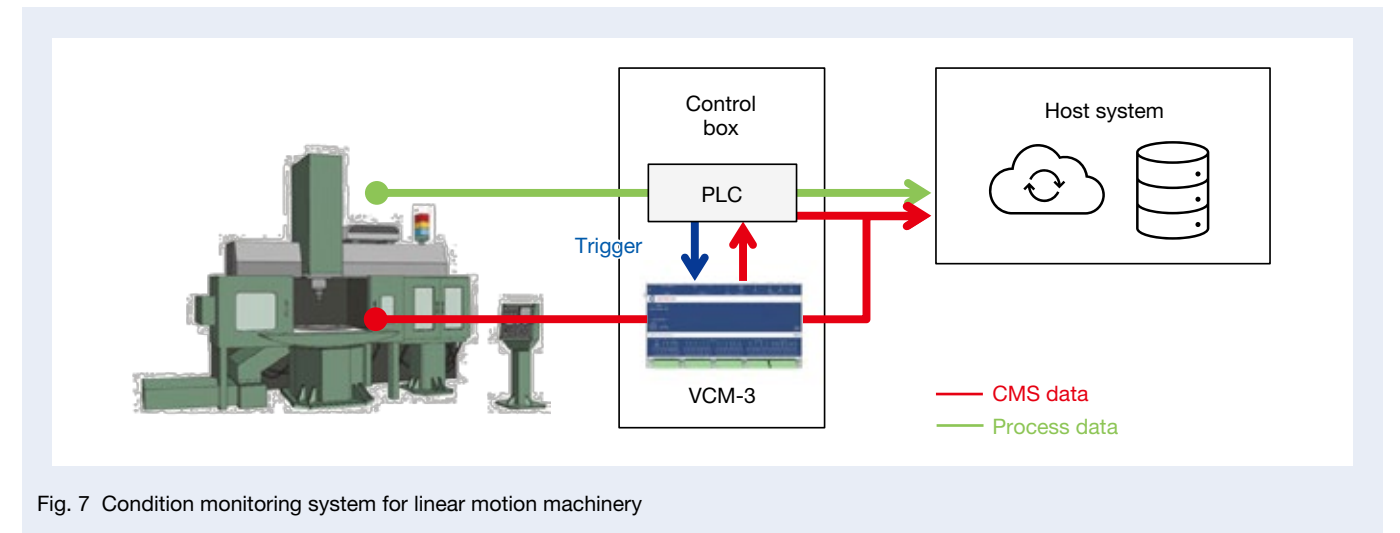1) Presentation Material of FY2022 Sustainability Conference Call
2) AVEVA PI System
   https://www.aveva.com/en/products/aveva-pi-system/

Fig. 7 Condition monitoring system for linear motion machinery

Nozomu Harada

Akihide Sakano

Technologies for Resisting Electrical Erosion in EVs

Junji Ono
Automotive Technology Development Center, Powertrain Bearing Technology Department

Abstract

Electric vehicles (EVs) are playing a crucial role in endeavors to prevent global warming, realize a sustainable society, and work toward carbon neutrality. As EV use continues to increase, bearing manufacturers must provide bearings suited to their unique requirements. In this article, we explore the latest trends related to electrical erosion in EVs and report on NSK's countermeasure technologies that are addressing that damage. While until recently ceramic balls have served as the main countermeasure against electrical erosion, NSK is continuing to optimize and develop new solutions, providing more choices to accommodate a wider spectrum of costs and applications.

1. Preface

Addressing global warming and creating a sustainable future require substantial efforts in decarbonization and achieving carbon neutrality. In the automotive field, the replacement of vehicles powered by internal combustion engines with EVs has been proposed and promoted[1]. EV drive units are becoming more sophisticated and efficient to promote the widespread adoption of EVs and enhance their market appeal. Higher system voltages has led to increased efficiency and reduced recharging durations. After smaller vehicles, larger ones are now being electrified. Figure 1 shows the actual and projected production volumes of EVs worldwide, as well as the proportion of high-voltage units with a system voltage of 700 V or higher, from 2021 to 2028. EV production is increasing year by year, and at the same time the proportion of EVs with higher system voltages is increasing. On the other hand, as EV drive units have higher system voltages and become more powerful, reports of electrical erosion damage to the motor support bearings have been emerging.
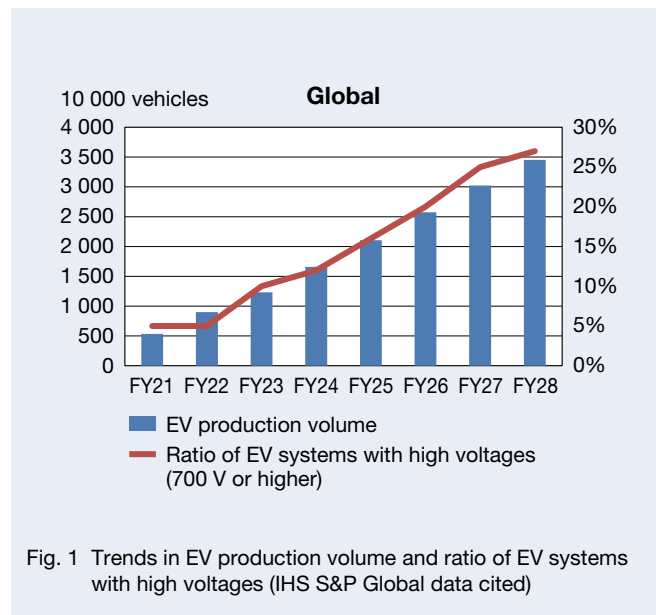

Fig. 1 Trends in EV production volume and ratio of EV systems with high voltages (IHS S&P Global data cited)

As a result, unit manufacturers now require bearings with high resistance to electrical erosion for use in EV drive systems. NSK has developed a variety of countermeasure products against electrical erosion but has decided that it is necessary to expand its lineup of countermeasure products against electrical erosion further. It is also continuing with this development in response to electrical erosion problems that are becoming increasingly diverse.

This article describes the phenomenon of electrical erosion of bearings in EV drive units, trends in countermeasure technologies against electrical erosion, and the latest electrical erosion countermeasures developed by NSK for EV drive units.

2. Electrical Erosion of Bearings in EV Drive Units

When electricity flows through bearings, damage called electrical erosion occurs. When there is little of this erosion, the raceway surface becomes slightly roughened and cloudy. But when the erosion becomes severe, ridge marks eventually develop. These marks are wavy, washboard-like bumps on the bearing raceway surface. Under normal operating conditions, the raceway rings and rolling elements of a bearing are slightly separated by an oil film based on the EHL theory, and since the oil film is an insulator, the inner and outer rings of the bearing are insulated from each other. A voltage higher than the dielectric strength of the bearing oil film would cause a breakdown, and sparks accompanying electrical discharge would occur between the raceway rings and rolling elements, causing electricity to flow. At the point where the spark occurs, the electricity is concentrated at a single point. Joule's heat raises the temperature, slightly melting the raceway surface and generating minute craters. As the current flow and cumulative number of sparks increase, small individual craters are considered to accumulate and develop into ridge marks (Photo 1). With ridge marks on bearings, the rolling elements riding over the bumps generate noise and vibration. These are eventually detected by the driver as noise and vibration in the EV drive unit, resulting in a failure.

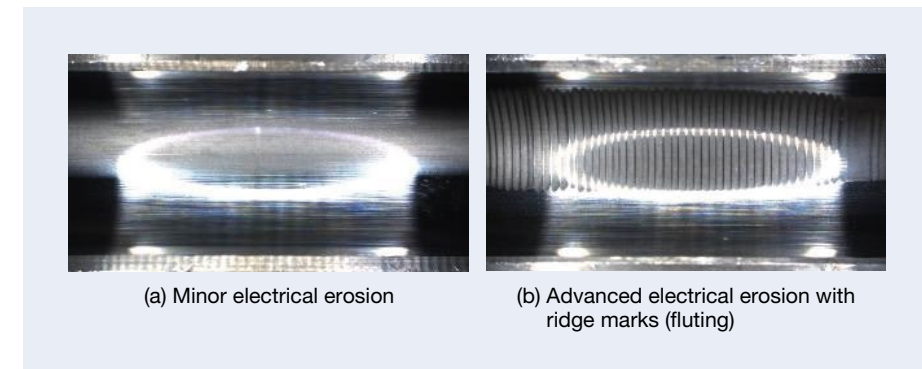(a) Minor electrical erosion (b) Advanced electrical erosion with ridge marks (fluting)

Photo 1 Electrical erosion on the bearing raceway

In EV drive units, there are several modes of electricity flow in bearings. Typical bearing current modes are the common mode current and the circulating current during motor drive. Figure 2 shows a schematic diagram.

Common mode currents are generated when the neutral point potential is not zero and a voltage of ±1/2 of the drive voltage acts between the coil end, rotor/stator, bearing, and case, synchronizing with the carrier frequency when the motor is driven. The equivalent circuit around the bearing is roughly a circuit connecting the capacitance components of each element, and the voltage is divided according to each capacitance component. The voltage is also divided in the bearing according to the capacitive component of the bearing. When the voltage exceeds a certain value, dielectric breakdown occurs, and the electric charge stored in the capacitance components is considered to be instantaneously discharged.

On the other hand, the circulating current is considered to be generated by the magnetic imbalance caused, for example, by the misalignment of the rotor and stator. It flows circulating in the shaft, bearing, and case. When a circulating current occurs, the bearing oil film maintains and sustains the electrical discharge, leading to early electrical erosion damage such as ridge marks.

Unit manufacturers sometimes find that electrical erosion occurs in bearings after the mid-term development of EV drive units, leading to the need for countermeasures. In such cases, where the bearing size is fixed due to the predetermined shaft layout for the unit and there is a necessity to minimize impact on the unit development schedule, ceramic ball bearings with ceramic rolling elements, which provide reliable protection against electrical erosion without changing the bearing dimensions, are often employed. However, using ceramic ball bearings without clarifying the factors causing electrical erosion could shift the site of electrical erosion to other areas where no countermeasures have been taken. In this situation, expensive ceramic ball bearings should be installed in many locations, resulting in high countermeasure costs. It is therefore very important that we understand the mechanism of electrical erosion correctly and apply countermeasures in the appropriate locations according to the particular electrical erosion of each unit.

3. Trends in Countermeasure Technologies against Electrical Erosion

As mentioned earlier, when electrical erosion becomes a problem in the middle stage of EV drive unit development, ceramic ball bearings are required as a remedial measure against electrical erosion. These bearings have a good track record as an electrical erosion countermeasure and are regarded as highly reliable against electrical erosion. Despite their high cost, their use in EVs is rapidly increasing, while the need for electrical erosion countermeasures have resulted in a high demand and a supply shortage. Subsequently, there is a significant demand for countermeasures against electrical erosion that are more cost-effective and can be more stably supplied compared to ceramic ball bearings.

In the area of bearings for railways running on electric motors, insulated bearings with ceramic sprayed on the outer diameter of the raceway ring or with resin over-molded on the outer diameter of the raceway ring have been used to prevent electrical erosion. Ceramic-sprayed insulated bearings have also been developed for general industrial motors and are already on the market. On the other hand, conductive bearings filled with conductive grease are used in office equipment applications. Countermeasures that have been developed and sold other than bearings include earthing parts, such as carbon brushes, conductive brushes, and conductive rubber, which are used to lower the shaft potential to the GND potential or to bypass the electricity flowing in the bearing.

In applying countermeasures against electrical erosion to EV drive units, optimization in specifications and costs is in progress based on the performance required of the countermeasures. Specifically, the target insulation capability, durability, cost, and production method are being optimized based on differences in operating conditions, performance against electrical erosion, bearing size, and planned quantity. In addition, to accommodate a wide range of electrical erosion phenomena and various unit layouts, the number of countermeasures against electrical erosion is continuously expanding (Figure 3).
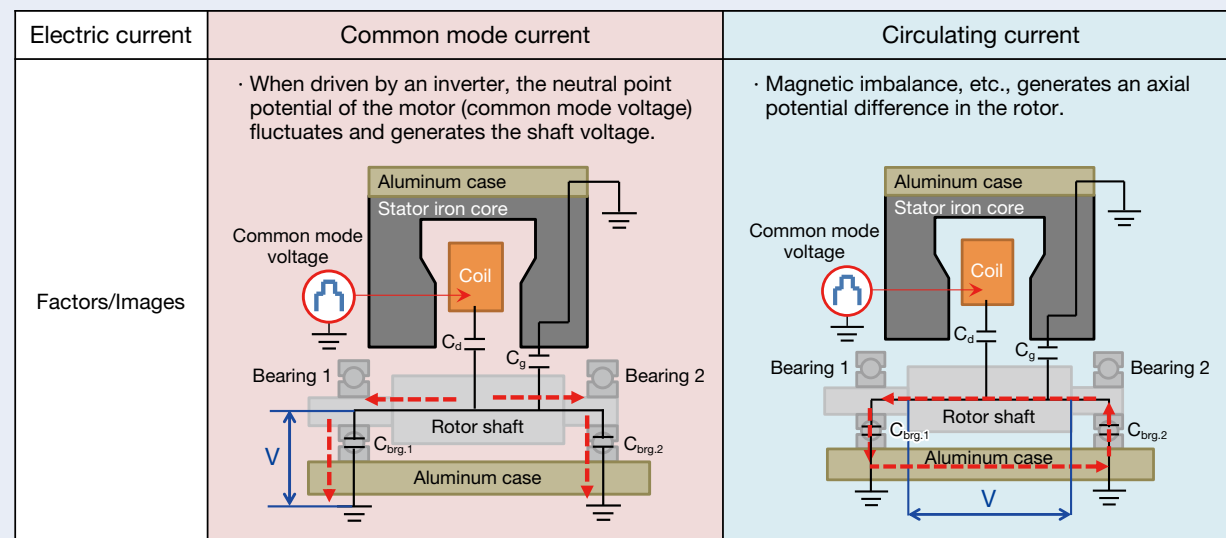

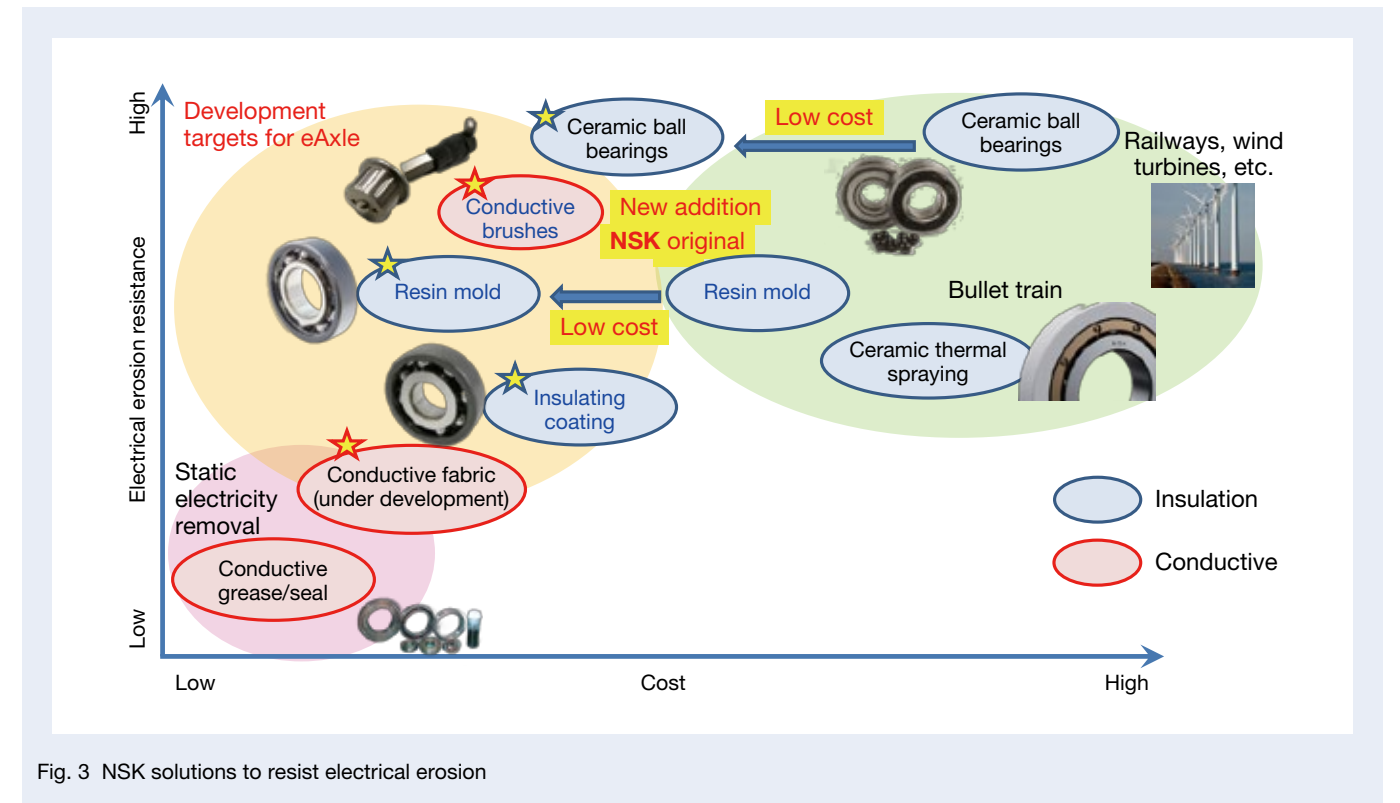Fig. 2 Schematic diagram of common mode current and circulating current

Fig. 3 NSK solutions to resist electrical erosion

4. Electrical Erosion Countermeasures

Electrical erosion occurs when electricity flows through the bearing. Consequently, protecting bearings from electrical erosion requires preventing electricity from flowing through the bearing oil film. Two countermeasures are possible: (1) stop the electricity and (2) bypass the electricity (Figure 4). The effective measures depend on the mode of bearing current generation and construction of the unit, among other factors. NSK aims to solve various EV drive unit problems by developing both insulation measures to stop electricity and conductive measures to bypass electricity. For instance, for common mode currents, the shaft potential is controlled near the GND using conductive elements so that the neutral point potential does not exceed the electrical voltage resistance of the bearing. For circulating currents, using insulating elements to block large loops of electrical circulating paths, including those in front of and behind the motor shaft, is considered effective. In the next section, we introduce representative countermeasures.
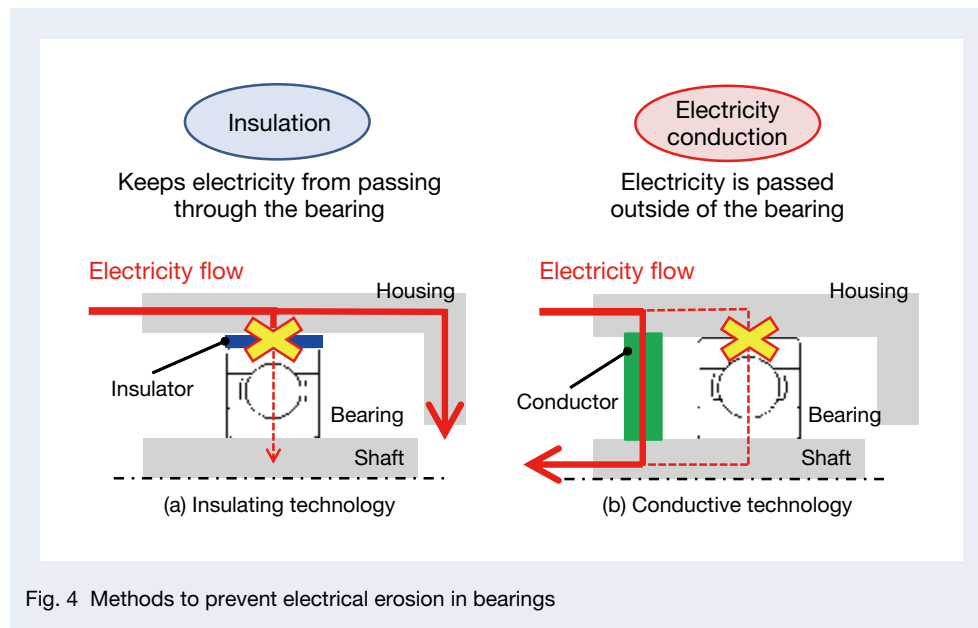

Fig. 4 Methods to prevent electrical erosion in bearings

4.1 Insulation countermeasures

4.1.1 Insulating coating bearings

A sintered resin coating with insulating properties was applied to the outer diameter of the raceway ring[2]. Photo 2 shows the insulating coating bearings and the results of electrical erosion tests with and without the insulating coating. The test conditions for the standard bearing without insulating coating were bearing: 6206, voltage: 3 Vp-p, frequency: 1 kHz, and test duration: 20 hours. The test conditions for the insulating coating bearing were bearing: 6206 (insulating coating), voltage: 50 Vp-p, frequency: 100 kHz, and test duration: 20 hours. Ridge mark-like electrical erosion occurred in the standard bearing (without insulating coating). However, no electrical erosion damage occurred in the insulating coating bearing tested under more severe electrical conditions. This test confirmed that the application of an insulating coating to the bearing interrupts the flow of electricity and is effective as a countermeasure against electrical erosion. NSK offers multiple technologies in the field of insulating coatings so that it can make optimal proposals according to the user's operating environment and the unit's production site. All specifications allow for sufficient performance in preventing electrical erosion under the assumed electrical conditions. Insulating coatings can be produced thinly, so insulation measures can be taken without changing the bearing's dimensions. It is also an effective countermeasure when there is a strong need to downsize the bearing, such as when the overall size of the drive unit needs to be reduced.

Photo 2 Insulating coating bearing and result of electrical erosion test

4.1.2 Resin-mold bearings

The outer circumference of the raceway ring was over-molded with a resin having insulating properties. Photo 3 shows the results of the electrical erosion test with and without a resin mold. The test conditions for the standard bearing without a resin mold were as follows: bearing: 6206, voltage: 3 Vp-p, frequency: 1 kHz, and test duration: 20 hours, and as for the resin-mold bearing, bearing: 6206 (resin mold), voltage: 50 Vp-p, frequency: 100 kHz, and test duration: 20 hours. As with the insulating coating, the resin over-molding can suppress electrical erosion damage to the bearing (Photo 3). The resin mold can be thicker than the coating, allowing a higher breakdown voltage to be set. In addition, the parasitic capacitance of the resin layer can be made smaller, which allows the effective impedance value to be maintained up to higher frequencies compared to that of the coating. Figure 5

shows a comparison of impedance measurements for 6207 bearings with various insulation measures.

When the resin is over-molded onto bearing raceway rings, if the joint strength is weak, there is concern that the resin may peel off or float on the bearing end face. Resin-mold bearings for railway applications have a special anchor groove shape to ensure joint strength[3]. As for resin-mold bearings for EV vehicles, the resin is trapped in a seal groove to act as an anchor. The resin layer and raceway ring are successfully and firmly joined (Figure 6). Using the seal groove as an anchor groove allows for the required strength, mass production, and cost reduction. The sufficient joint strength makes assembly possible even with an insulating layer if a light press-fit is used, and thus widens the range of options for bearing handling and installation. The following press-fit tests were conducted. The resin-mold bearing was press-fitted into an aluminum jig, simulating the bearing mating surface

of an EV drive unit to check for damage to the resin part and dimensional changes. The bore diameter of the jig was ϕ 63 (−0.067/−0.072), the tightening allowance was 0.054 to 0.072 mm, and the test N number was N = 5 (separate unit). The bearings were press-fitted into the housing jig

and then taken out to check for damage and dimensions. None of the bearings pulled out after press-fitting was damaged, and no significant change was observed in the outer diameter dimensions after press-fitting. The bearings were slightly shinier than the new bearings, and press-

Photo 3 Resin-mold insulated bearing and electrical erosion test results
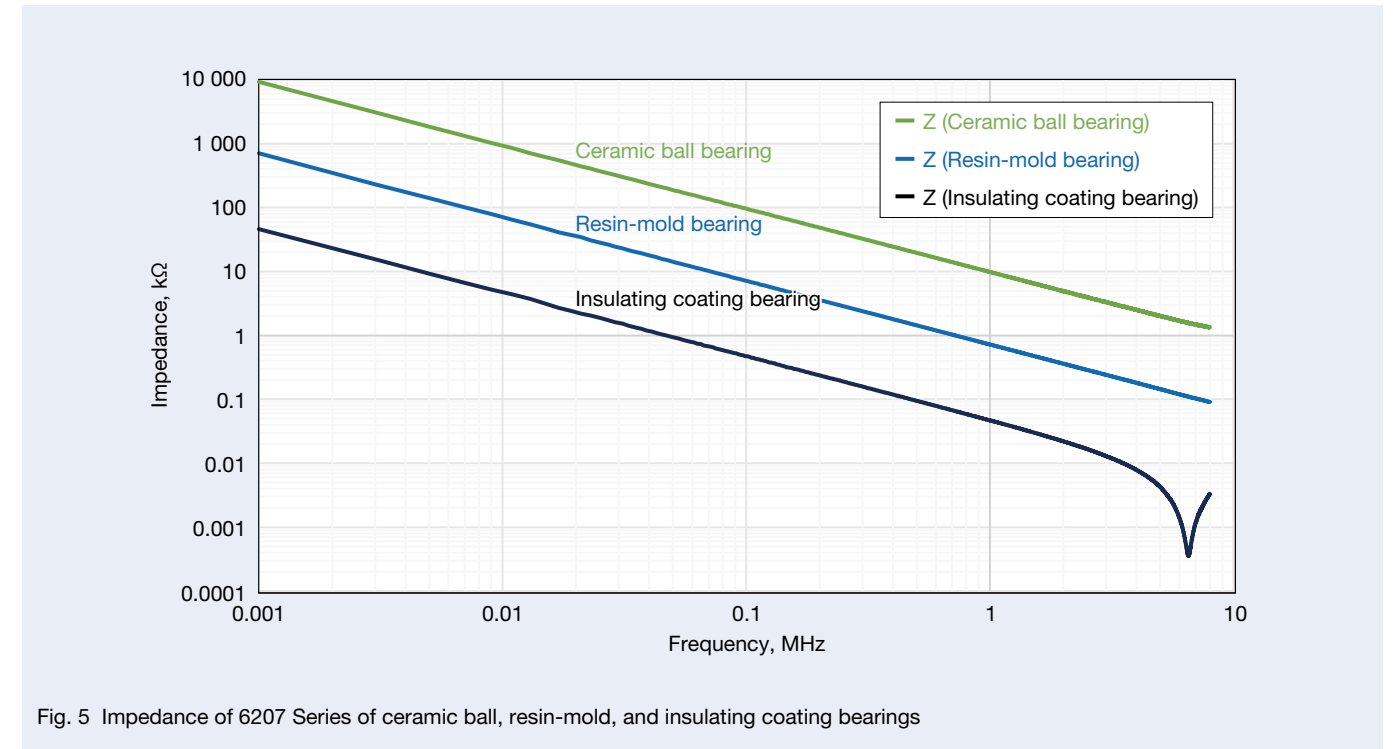

Fig. 5 Impedance of 6207 Series of ceramic ball, resin-mold, and insulating coating bearings
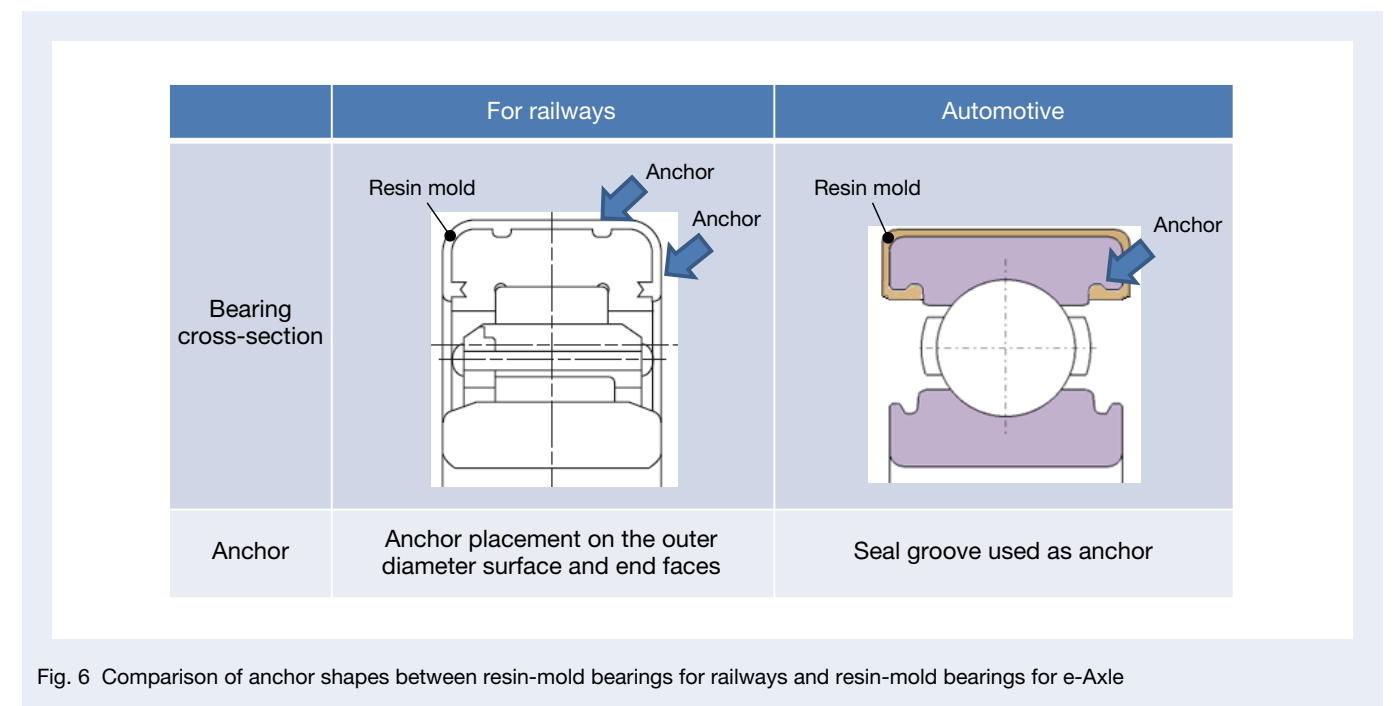

Fig. 6 Comparison of anchor shapes between resin-mold bearings for railways and resin-mold bearings for e-Axle

fit scratches caused by housing edges were observed, but these were within an acceptable range in terms of avoiding any functional issues (Photo 4).

Using a resin softer than the aluminum used for the housing makes it less likely to wear the housing mating surface, even if rotational creep occurs. Figure 7 shows the results of the rotational creep test. Rotational creep tests were conducted under two loading conditions: rotational loading and unidirectional loading. The test results showed that the resin-mold bearing suppressed housing wear compared to the standard bearing regardless of rotational load or unidirectional load. The resin mold itself shows little wear and is effective as a countermeasure against rotational creep.

The resin layer is set with a thickness of about 0.5 to 2.0 mm, which increases the bearing size by about 1.0 to 4.0 mm in both outer diameter and width. Therefore, if the bearing size cannot be changed during or late in the development of the unit, it is necessary to adjust the raceway ring thickness and, in some cases, the bearing internal specifications.
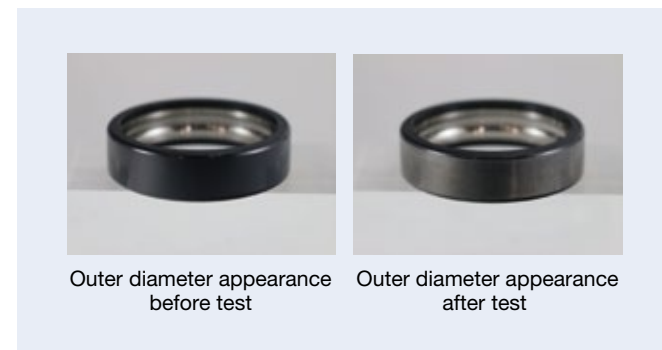

Photo 4 Appearance of resin-mold bearing after press-fit test

4.2 Conductive countermeasure items

4.2.1 Conductive brushes

NSK's development concept was to create a conductive brush that can be used in oil. Conventional conductive brushes are often used in radial contact, and it is difficult to ensure conductive performance in oil because an oil film is formed between the brush and shaft. Applying them to oil-cooled motors therefore necessitates the use of such measures as installing oil seals and preparing a dry space where the oil does not enter the brush section.

The conductive brush developed by NSK (Photo 5, Figure 8 (a)) uses a configuration in which the brush and shaft rotational center axis are in axial contact via steel balls. In this configuration, the relative velocity at the point of contact between the shaft and brush is zero, which ideally prevents the formation of an oil film (Figure 8 (b)) and thus ensures stable conductive performance even in oil.

Photo 5 Conductive brush under development (initial prototype)

Conditions	Resin mold
Test bearings	6206
Radial load, N	1 000
Radial load direction	Rotational load
Axial load, N	0
Rotation speed, rpm	7 000
Temperature, °C	Room temperature, naturally developed
Current waveform	Alternating current
Frequency, kHz	10
Testing time, hour	Approx. 404

(a) Test conditions and test results under rotating load

Conditions	Resin mold
Test bearings	6206
Radial load, N	7 800
Radial load direction	Unidirectional load
Axial load, N	0
Rotation speed, rpm	7 000
Temperature, °C	Room temperature, naturally developed
Current waveform	Alternating current
Frequency, kHz	10
Testing time, hour	74 ($L_{10} \times 2$)

(b) Test conditions and test results under static load

Fig. 7 Creep test conditions and results for resin-mold bearings
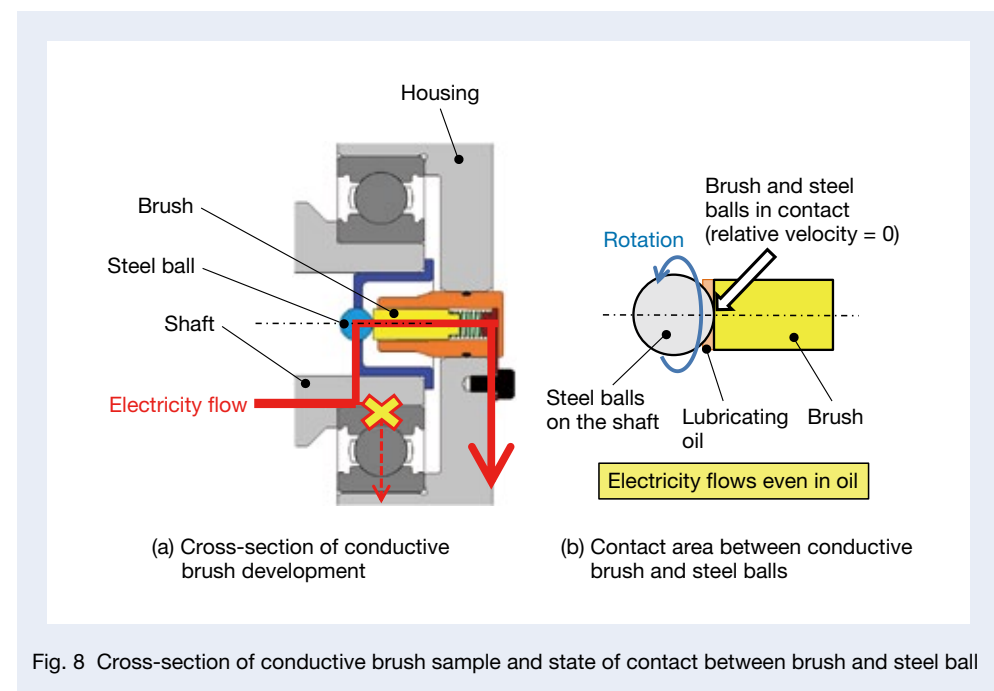

Fig. 8 Cross-section of conductive brush sample and state of contact between brush and steel ball

Figure 9 shows the results of the conductivity verification tests. When a general radial contact brush was used in oil, electricity flowed through the bearing. However, when an NSK-developed conductive brush was installed, the current flowed through the conductive brush, confirming that the brush bypassed the electricity flowing in the bearing as intended.

Figure 10 shows the impedance measurement results of the conductive brush. The measurement conditions were a shaft rotation speed of 5 000 rpm, oil lubrication, and an oil temperature of 60°C. A HIOKI IM3563 LCR meter was used for the measurement. The measurement results show that an impedance performance of less than 1 Ω was achieved at a frequency of 10 kHz.

Conductive brushes can be applied as an EMC countermeasure in addition to their countermeasure effect against electrical erosion. A spark in a bearing would cause a sudden change in current. The consequent generation of electromagnetic waves is problematic. Applying conductive brushes bypasses the current, dropping the shaft voltage to below the dielectric strength of the bearing oil film. Consequently, electromagnetic disturbances caused by sparks in the oil film can be reduced.
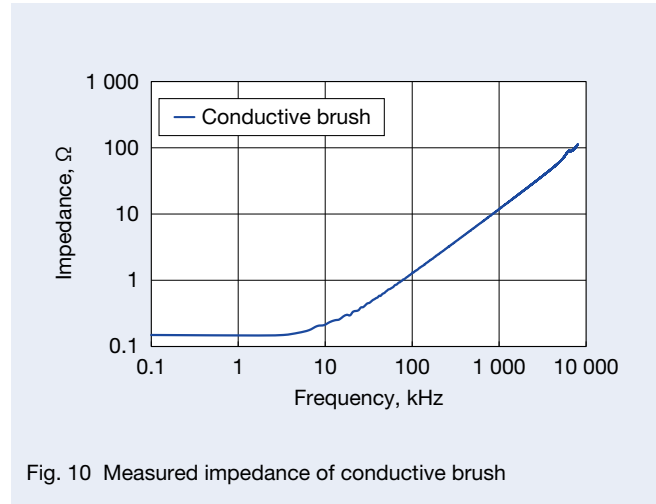

Fig. 10 Measured impedance of conductive brush

5. Postscript

The automotive industry is witnessing the spread of EVs, leading to accelerated development by unit manufacturers and shortened lead times. NSK is committed to staying aligned with these trends and will continue to develop products that meet user requirement while promptly adapting to evolving market demands.

This article introduces the latest countermeasure technologies against electrical erosion for EVs, including those currently under development at NSK. Through the development of these products, NSK will contribute to the realization of a sustainable society by providing value in the form of improved reliability, low vibration, and low noise for EVs and by reducing environmentally hazardous materials and energy consumption.

References

1) Ministry of Economy, Trade and Industry, "Mobiritei no kouzou-henka to 2030nen ikou ni muketa jidousha-seisaku no houkousei ni kansuru kentoukai sankou-shiryou," (Reference materials for the study commission on structural changes in mobility and the direction of automobile policy for 2030 and beyond).
2) S. Katto, "Development of Bearings with Insulating Coating to Resist Electrical Corrosion in HEV/EV Units," *NSK Technical Journal*, No. 695 (2023), pp. 2–7.
3) T. Yamada and T. Uchiyama, "Insulated Bearings for Railway Traction Motors," *NSK Technical Journal*, No. 675 (2003), pp. 9–13.
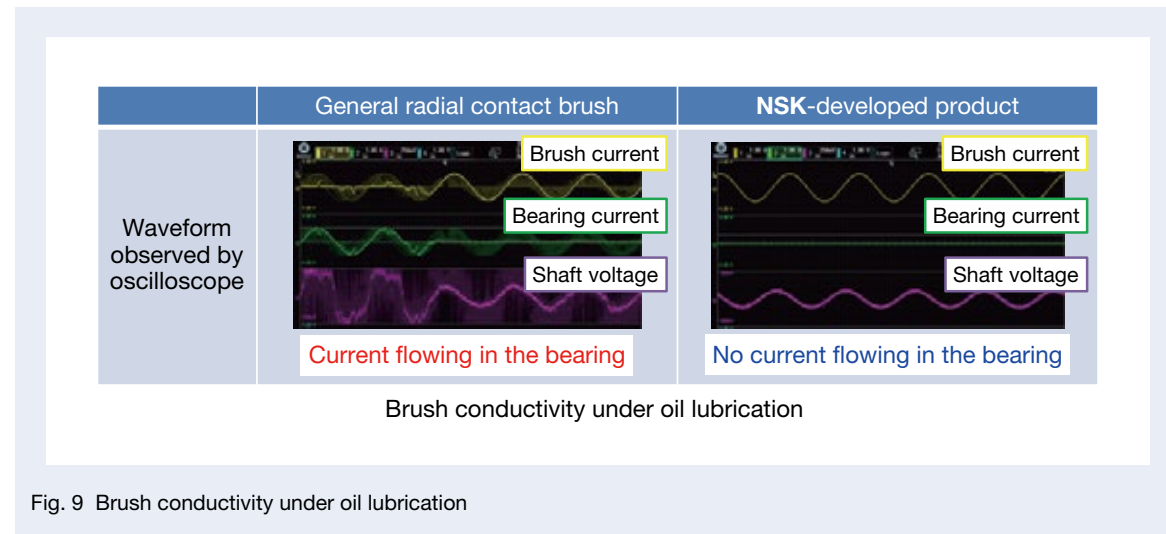
Junji Ono

Fig. 9 Brush conductivity under oil lubrication

Efforts for Higher Reliability and Recent Technical Trends in Hub Unit Bearings

Keiju Haraguchi
Automotive Bearing Technology Center, Chassis Bearing Technology Department

Abstract

As the automotive industry undergoes a once-in-a-century transformation towards electrification, stronger environmental regulations around the world are shaping the active development of electric vehicles (EVs). The improvement of power consumption in EVs requires lower friction in hub unit bearings. At the same time, hub unit bearings must be highly reliable and resist damage even in harsh environments. NSK has developed technologies to achieve both high reliability and low friction while also establishing a method to predict brinelling depth.

1. Introduction

The automotive industry is undergoing its biggest transformation in a hundred years. Electrification is a particularly hot topic these days, with electric vehicles (EVs) being actively developed in response to stricter environmental regulations around the world. Extending the cruising range of EVs has become an issue, and improving electricity costs is an urgent priority. Reducing various resistances generated from running a car is necessary to improve electricity costs, and hub unit bearings (Figure 1) need to reduce friction.

Hub unit bearings play an important role in EVs as well, as they support the vehicle's wheels, and require high reliability as a basic function to prevent damage even in harsh environments. The hub unit bearing is an underbody component. Road conditions are often poor in markets where infrastructure is not well developed, such as in emerging countries, so when driving through puddles, muddy water is splashed up by the tires and splashes around the hub unit bearing. When used in

such a harsh environment, muddy water intrudes into the bearing, causing delamination due to rust and poor lubrication, which results in abnormal noise. For reasons discussed below, reducing the friction of hub unit bearings associated with the shift to EVs in vehicles often increases the risk of muddy water intrusion. When the ball rides over a pothole or curb, and an impact load is applied, plastic deformation called brinell indentation occurs at a ball pitch on the balls and ring raceway surfaces, causing abnormal noise. The risk of brinelling becomes higher with increases in vehicle weight due to the conversion to EVs. Additionally, in an investigation of market-recalled products, muddy water ingress and noise caused by brinell indentations were the main causes of hub unit bearing failures.

This article introduces technologies that can achieve low friction while maintaining the robustness and high reliability of hub unit bearings, technologies that can improve brinelling resistance and technologies for predicting brinelling depth.

2. High Reliability Low-Friction Seal

Figure 1 shows the structure of the drive wheel components and hub unit bearings that transmit power from the engine or motor. In most cases, hub unit bearings have an inner seal and an outer seal. Seals prevent the muddy water splashed up from the road surface from entering the bearing.

Conventional inner seals are often used in combination with slingers, with three lips in contact with the slinger to prevent muddy water from entering the bearing. On the other hand, the conventional outer seal has no slinger and has three lips in contact with the hub shaft and one

non-contacting labyrinth lip to prevent muddy water from entering the bearing.

Reducing the number of lips in contact or the contact force of the lips is effective for meeting the low friction requirements for hub unit bearings in the EV conversion of vehicles. As a drawback, however, these modifications aimed at lower friction may compromise reliability, the basic function of the hub unit bearing. NSK has developed a seal that achieves low friction without compromising muddy water resistance, which is described in the next section.
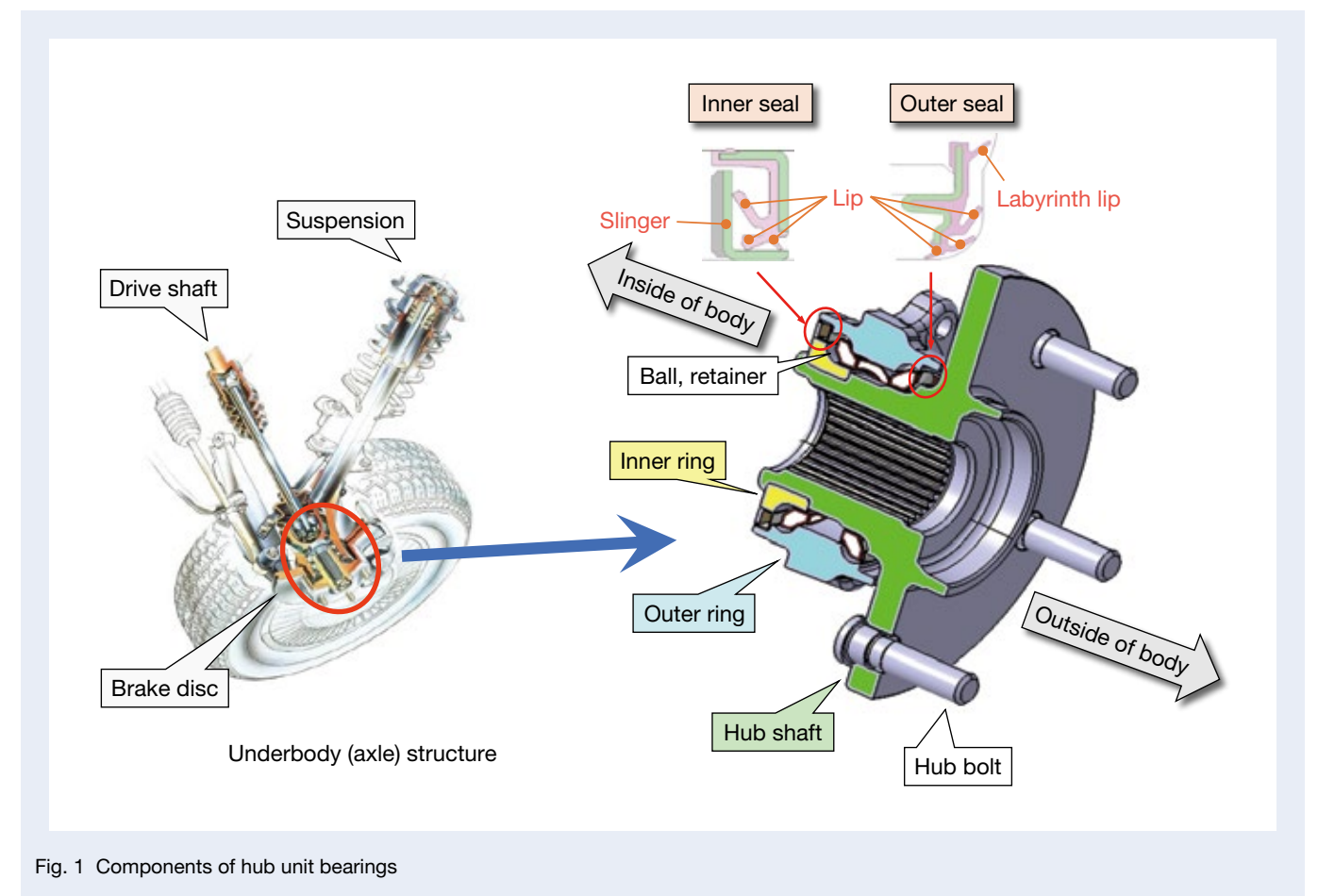

Fig. 1 Components of hub unit bearings

2.1 Low-friction inner seal

The conventional inner seal's slinger is L-shaped, whereas the low-friction inner seal, which retains muddy water resistance, changes to a U-shaped slinger (Figure 2). The U shape tends to reduce the amount of water in the seal when the slinger rotates, compared to the conventional product. This is because the U-shaped slinger creates a flow of muddy water inside the seal that moves outward, preventing muddy water from entering.

NSK created a fluid analysis 3D model up to the center of the shaft immersed in water and confirmed the validity of this consideration through fluid analysis. Figure 3 shows the results of fluid analysis for the conventional and new products. The percentage of water or air in the inner space of the seal of the hub unit bearing is indicated by color: brown for 100% water, white for 100% air, and blue for 50% each of water and air. The seal cross-section in water at a standstill is 100% water in the space from the side lip to the outside of the bearing. From this state, the slinger was rotated, and the behavior of water in the space outside the bearing from the side lip was compared between the conventional and new products.

In the conventional product, a large amount of water had entered the space outside the bearing from the side lip, and although there was some air mixed in, water had also reached the tip of the side lip. As for the new product, there was less water in the space outside the bearing from the side lip compared to the conventional product, indicating that water did not reach the tip of the side lip. The inability of the water to easily reach the tip of the side lip, compared to the conventional product, facilitates water resistance.

Figure 4 shows the muddy water resistance and torque test results for both products. The new product showed the same or better resistance to muddy water than the other and achieved a 30% reduction in torque.
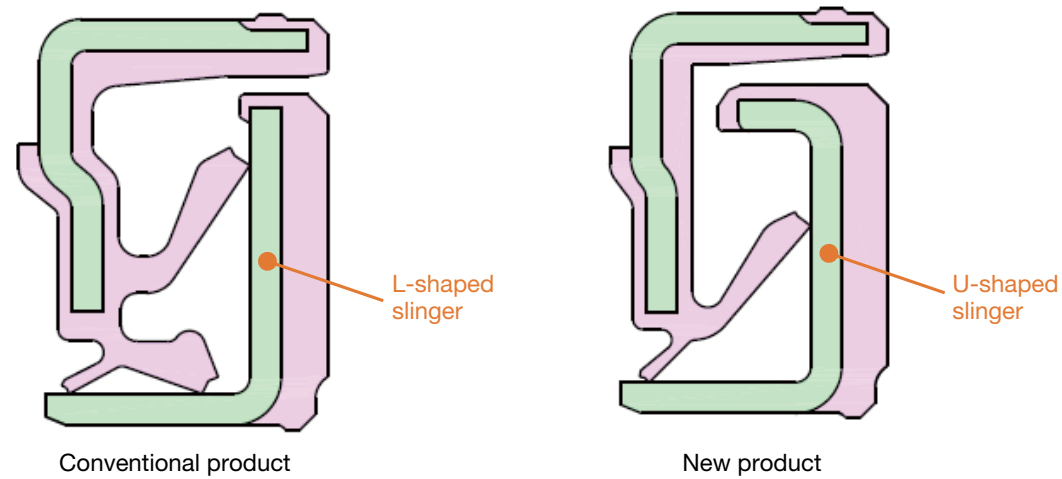

Fig. 2 Concept for high reliability low-friction inner seal
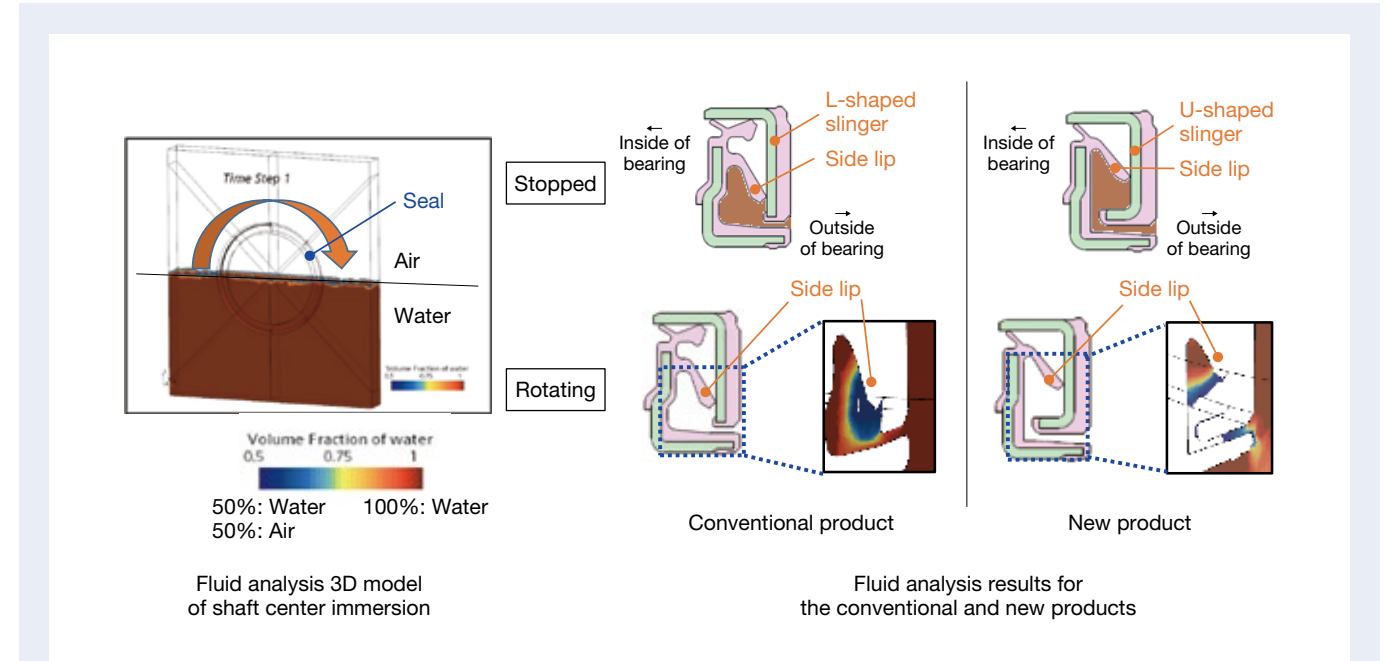

Fig. 3 Fluid dynamics of conventional and developed seals
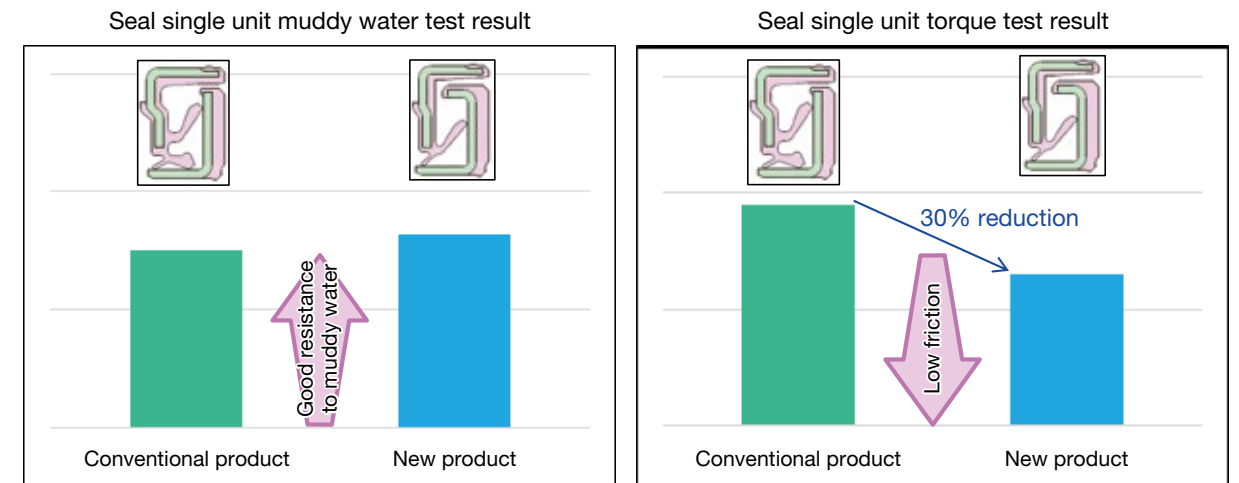

Fig. 4 Sealing performance and torque reduction with developed seal

2.2 Low-friction outer seal

Figure 5 shows the low-friction outer seal that retains muddy water resistance. Changes from the conventional outer seal include the addition of U-shaped slingers and the use of two lips instead of three. The addition of U-shaped slingers creates a labyrinth structure and keeps muddy water away from the side lips. As a result, the amount of muddy water reaching the side lip is reduced, in turn reducing the number of lips, and low friction can be achieved simultaneously.

Figure 6 shows the muddy water resistance and torque test results for both products. The new product's muddy water resistance is equivalent to that of the other, but the torque can be reduced by 40%.
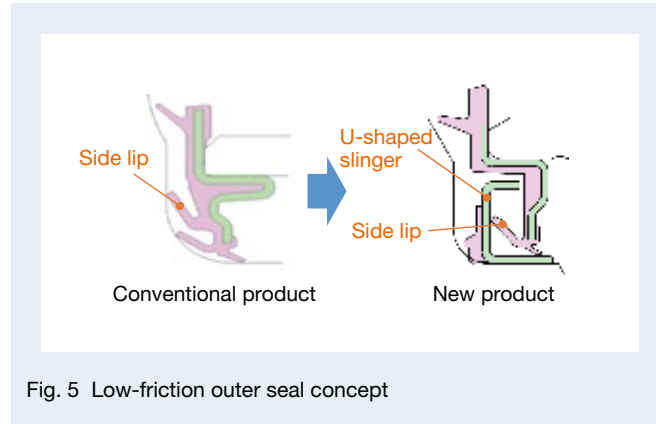

Fig. 5 Low-friction outer seal concept

Fig. 6 Sealing performance and torque reduction with developed seal

2.3 New seal grease

As previously mentioned, the hub unit bearing is equipped with a seal to prevent muddy water from entering the bearing. Sections 2.1 and 2.2 describe these seals' low-friction performance. NSK has developed a new seal grease to achieve even lower friction. This grease is also introduced here because it achieves low friction without compromising muddy water resistance.

It has a lower base oil kinematic viscosity than the conventional grease and uses a thickener with higher base oil retention. Employing thickeners with high base oil retention reduces the amount of thickener used, thereby reducing the thickener's shear resistance. When the kinematic viscosity of the base oil is small, however, its high fluidity tends to cause oil film breakage and allow muddy water to intrude through the seal. The new grease contains a polar polymer in the base oil so as not to reduce the muddy water resistance, and technology has been developed to reduce water ingress even when the oil film at the seal lip is thin through an ingenious molecular structure. Figure 7 shows how polar polymers work. Polar polymers have a long molecular structure, and the complex intertwining of these chains holds the base oil molecules that intervene between the lip tip and the sliding surface in place. This prevents the oil film from rupturing when the oil film comes into contact with muddy water. Moreover, the polar polymers improve the affinity between the lip rubber material and sliding surfaces of the slinger, making it easier for oil film and grease to intervene in the sliding section.

Figure 8 shows the results of a muddy water test and torque test conducted on the seal single unit to confirm its effectiveness. The sealing performance was improved by 50%, and torque was reduced by 25% compared to the conventional product.
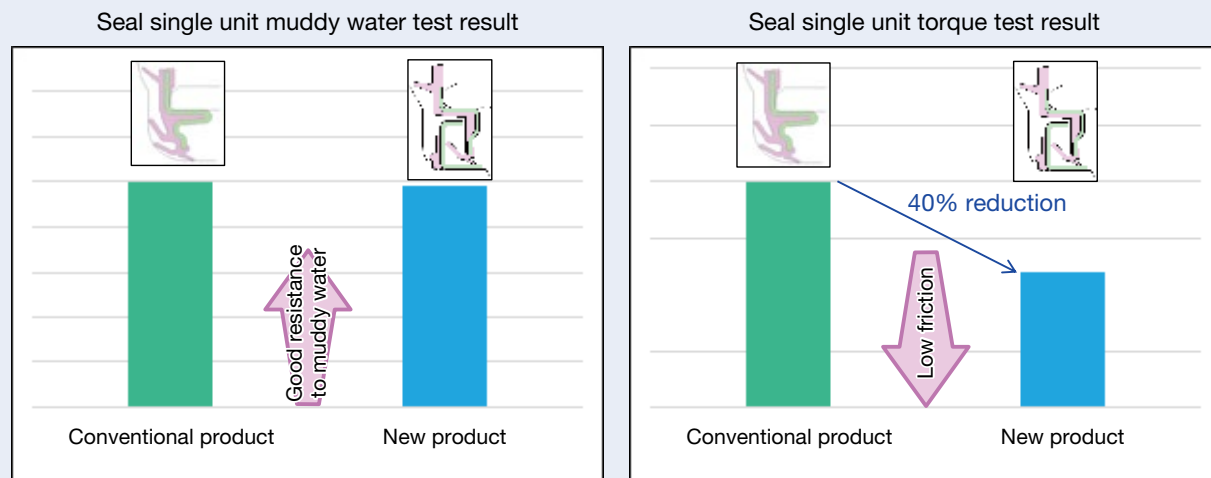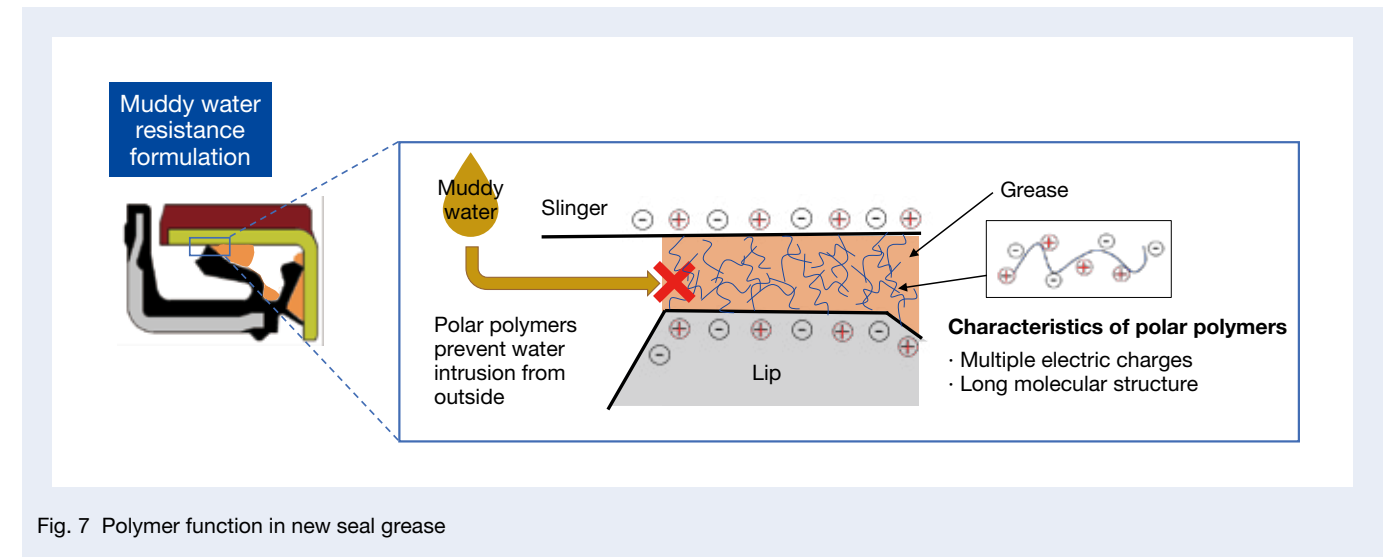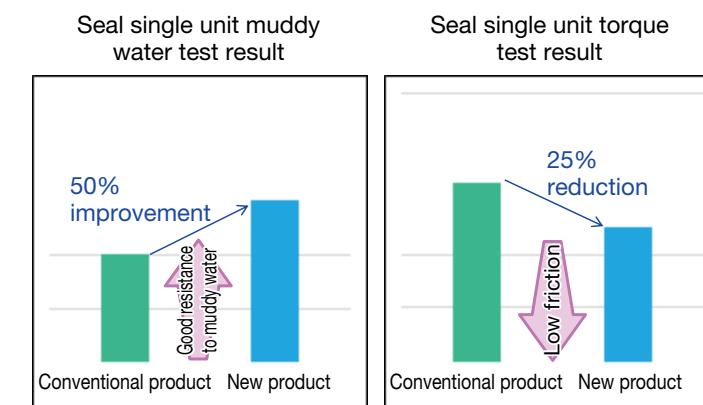

Fig. 7 Polymer function in new seal grease

Fig. 8 Sealing performance and torque reduction with developed grease

3. Second Generation Low-Friction Grease with Water Resistance

Although the new seal improves muddy water resistance, it is difficult to completely prevent muddy water from entering the bearing. If even a tiny bit of moisture intrudes into the bearing, the grease will not form a lubricating film as easily. This results in metallic contact between the raceway surface and balls, wear, and micro-cracking, which can lead to delamination. NSK has developed and marketed water-resistant grease for bearings as a technology that renders this small amount of water intrusion harmless.

Figure 9 shows the technology of making water-resistant grease harmless. Additives provide two actions to water-resistant grease. One is to control the particle size of water that enters the bearing, keeping water away from the balls and raceway surfaces. The other is the early formation of a thick oxide film on the balls and raceway surfaces, which inhibits water-metal contact.

NSK developed a first-generation low-friction grease with low friction and reliability in high temperature and high load ranges by employing a base oil with a viscosity that does not change with temperature. This first-generation low-friction grease has the water-resistant effect previously mentioned. We have already started mass production and introduced this grease to the market.

NSK has also recently developed a second-generation low-friction grease, aiming for even lower friction than the first-generation low-friction grease. As in the first generation, the base oil is a chemically synthesized oil with low viscosity change over a temperature range to reduce rolling resistance over a wide temperature range.

The use of a thickener with finer fibers than that of the first generation aims to increase the retention of base oil, reducing the amount of thickener and stirring resistance. Furthermore, the consistency of the grease is made smaller (harder grease) to reduce stirring resistance. The smaller consistency prevents grease pushed out of the raceway surface by the balls and cage from returning to the raceway surface, thereby reducing stirring resistance.

Figure 10 shows a performance comparison of first- and second-generation low-friction greases. The second-generation grease has 30% lower friction while maintaining high speed, high-load endurance, and low-temperature fretting resistance.
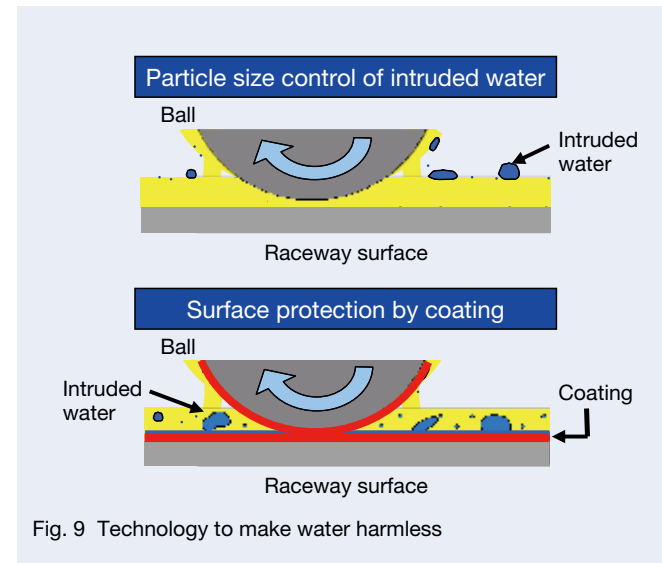

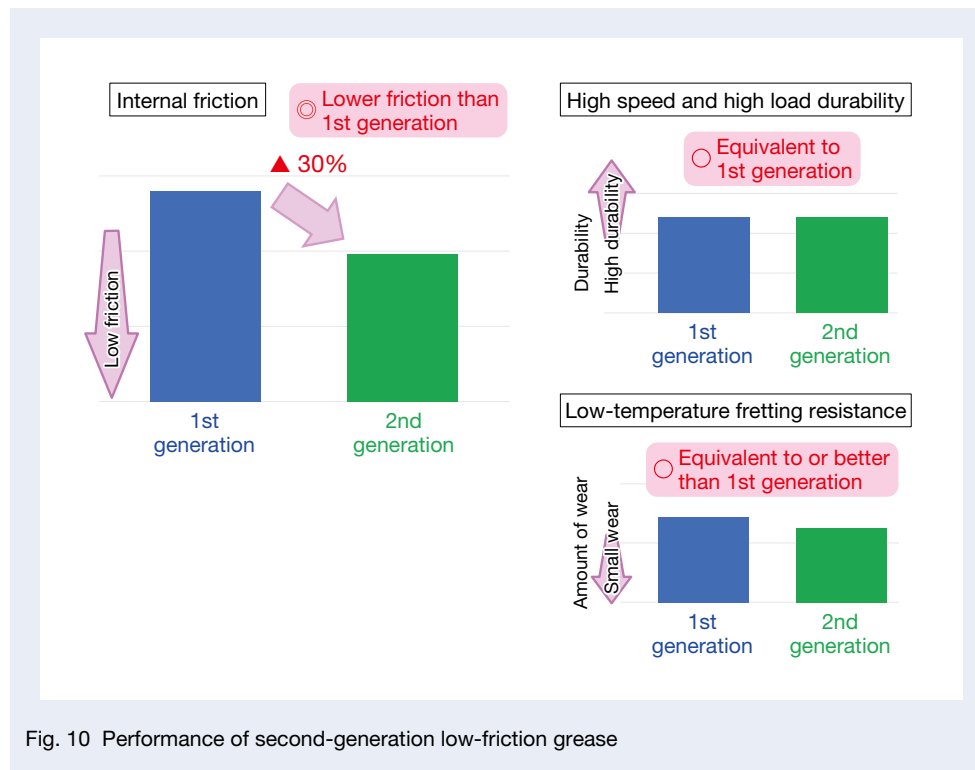Fig. 9 Technology to make water harmless

Fig. 10 Performance of second-generation low-friction grease

4. Technology to Improve Brinelling Resistance

So far, we have introduced technologies for high reliability and low friction against muddy water intrusion. As mentioned at the beginning of this article, brinell indentation, caused by excessive or impact loads on the hub unit bearings, is another cause of abnormal noise. To increase the reliability of hub unit bearings, taking measures against brinelling is crucial. One countermeasure against brinelling is to increase the bearing size and static load rating, but increasing the bearing size leads to more weight, interference with surrounding parts, and assembly impact.

NSK has developed a high-performance cage that can increase the static load rating while maintaining the bearing size as a technology to improve the brinelling resistance. In addition, a new analysis method has been devised to improve the prediction accuracy of brinelling depth.

4.1 High-performance cages

The new high-performance cage allows for one more ball without changing the bearing size (ball PCD), or the addition of one ball with minimal size increase, thus allowing for the high load capacity of the bearing.

In contrast to the conventional product, the new one removes the pillars between the balls, as shown in Figure 11. This narrows the distance between adjacent balls and increases the number of balls by one without changing the PCD. This cage makes it possible to improve the brinelling resistance without affecting the surrounding components. In fact, a hub unit bearing with the same ball PCD and one more ball was found to reduce the brinelling depth by about 30% in the brinelling test.

To meet the demand for lower friction, NSK has incorporated low friction technology into the new product to achieve both brinelling resistance and lower friction. The low-friction technologies are described below.
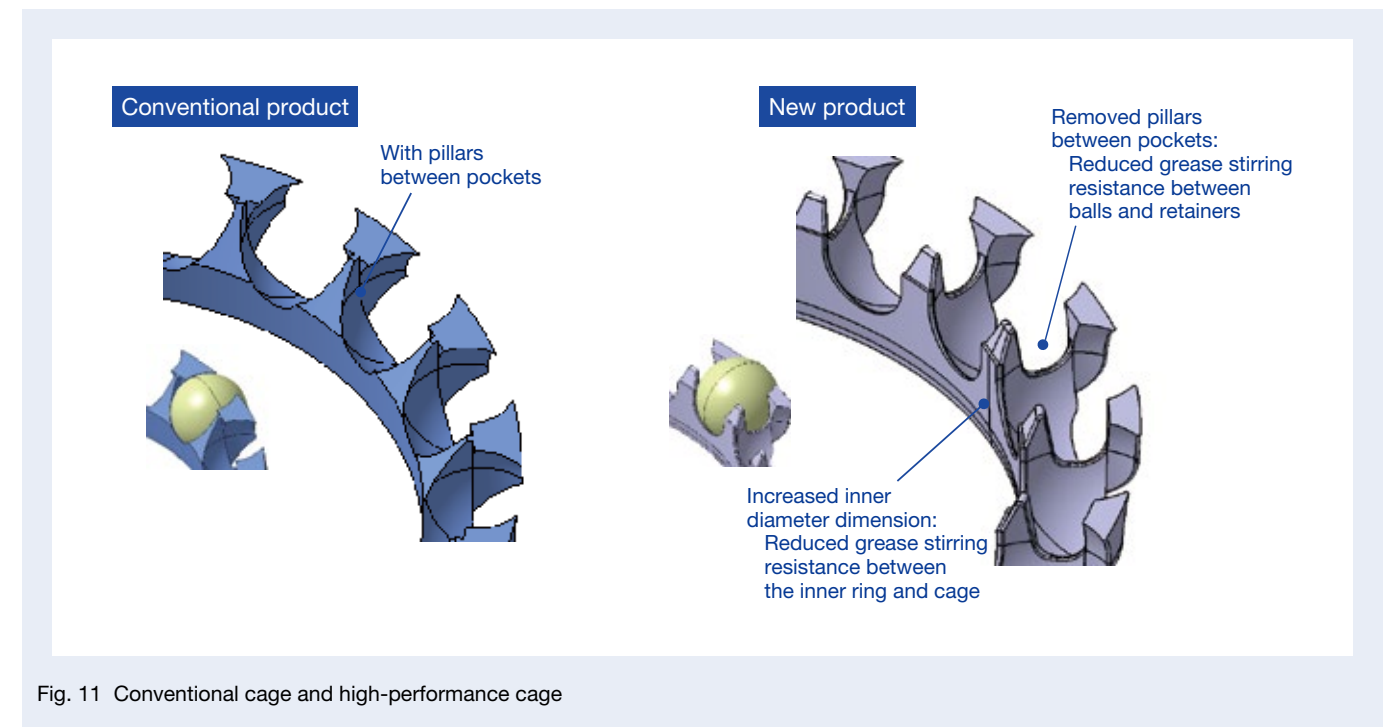

Fig. 11 Conventional cage and high-performance cage

· Reduction of stirring resistance between the balls and cage by eliminating the pillars
· Reduction of stirring resistance between the inner diameter of the cage and the outer diameter of the shaft by changing the inner diameter dimensions of the cage

Figure 12 shows the friction reduction effect of the new product. The product can achieve a 10% reduction in internal torque compared to the conventional product.

4.2 Brinelling depth prediction method

While it is known that a high-performance cage improves brinelling resistance, it is difficult to predict brinelling depth quantitatively on a theoretical basis. The brinelling index, calculated by static load rating, distance between working points, shaft weight, and rim radius, qualitatively predicts market failure. NSK has been working to establish a new brinelling depth prediction method to prevent brinelling failures and propose optimal bearing sizes.

Conventional evaluation tests for the brinelling depth of hub unit bearings are performed by applying an axial load to a loading arm attached to the hub flange. NSK has been performing an assembly analysis that simulates this evaluation test to predict the brinelling depth (Figure 13).

The raceway surfaces are quenched by induction heat treatment and have a hardness gradient from the raceway surface layer to the depth. The material properties that account for this hardness gradient are used in the analysis.
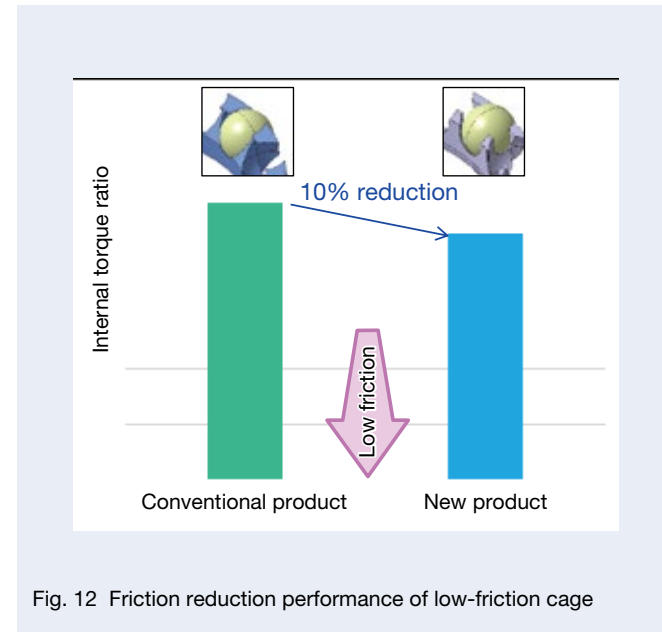
Fig. 12 Friction reduction performance of low-friction cage

The actual brinelling depth obtained from the analysis and test results are close (Figure 14), confirming the validity of the brinelling depth prediction method based on assembly analysis. In the future, we will aim to establish a method for predicting brinelling depth to further improve accuracy.
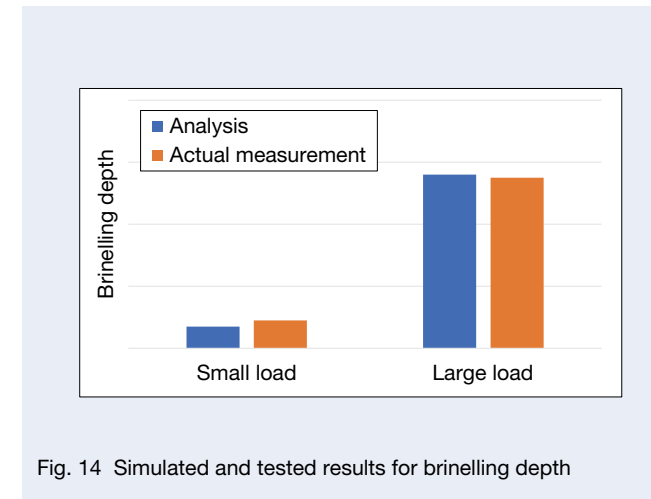
Fig. 14 Simulated and tested results for brinelling depth

5. Conclusion

In recent years, the demand for low-friction hub unit bearings has been increasing along with the shift to EVs. Low friction, however, often reduces muddy water resistance, and the increase in EV-related weight often reduces brinelling resistance, making compatibility with high reliability a challenge. NSK has been developing low-friction technologies based on its highly reliable technologies, and the technology described in this article has been developed to achieve low friction without compromising reliability.

NSK will continue to contribute to the development of automotive technology by developing even more reliable, low friction technologies to satisfy the market's need for reduced defects and lower friction.

Keiju Haraguchi
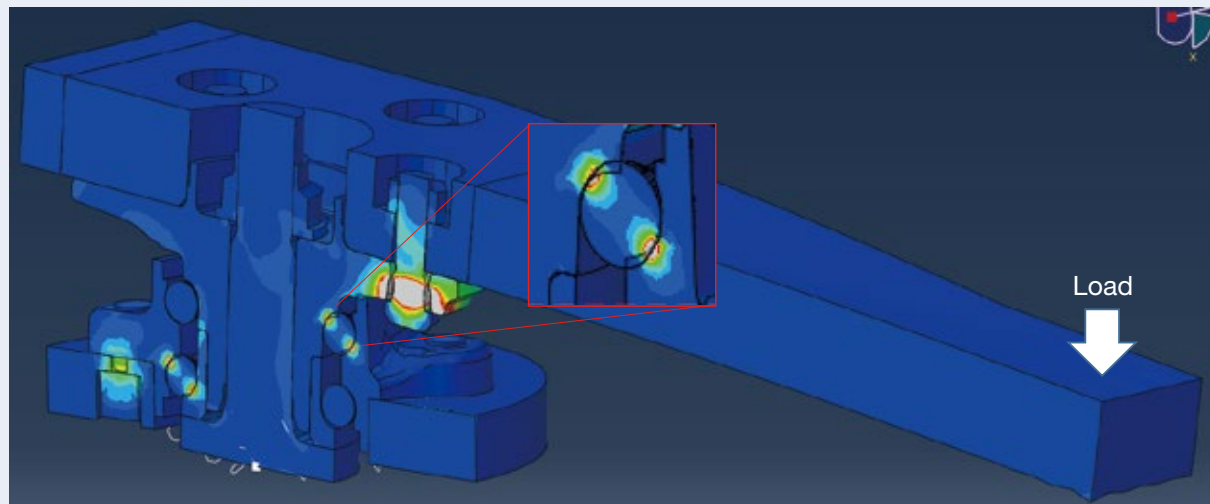
Fig. 13 Assembly analysis to predict brinelling depth

Performance Study of Rattle Noise in EPS Reduction Gears Using Multibody Dynamics

Masahiro Harunaga
NSK Steering & Control, Inc., Steering Engineering Center, Mechanical Design Department

Abstract

The adoption of hybrid and electric vehicles is accelerating worldwide, increasing the need for quiet electric power steering (EPS). The sound and vibration phenomena of EPS systems are influenced by various factors. When these exceed certain thresholds, EPS systems can affect the sound inside the vehicle. A lot of time is therefore spent on addressing EPS noise and vibration. This article includes a case study on EPS performance using simulations of multibody dynamics (MBD) to efficiently resolve vibration issues. In the case study, we analyzed the rattle noise generated in the EPS reduction gear. Using MBD simulations enabled significant improvements in rattle noise without the need for multiple prototypes.

1. Preface

The need to reduce CO_2 emissions to protect the global environment[1] has led countries around the world, including the United States, China, and in Europe, to set a goal of eliminating internal combustion engine-only vehicles, accelerating the movement toward hybrid and electric vehicles. Accordingly, to make vehicle interiors quieter, electric power steering (EPS) installed in vehicles must be quiet.

EPS consists of mechanical components (reduction gears, etc.), hardware (motor, ECU), and software (control). It generates various sound and vibration phenomena due to different factors, such as rattle noise caused by the rattling of mechanical components due to reverse input from the road surface when driving on rough roads, operating noise from the motor's order components, and vibration from resonance between the EPS and vehicle. If these phenomena exceed a certain threshold value, the cabin's quietness is impaired, resulting in the driver's discomfort. The sound and vibration phenomena of EPS vary widely depending on vehicle type and the operating environment. A lot of time is therefore spent on trial and error in efforts to solve the problem. The challenge for product development is how to make the process more efficient. Model-based development (MBD) is an important development method that aims for efficient product design by enabling performance studies before manufacturing[2]. Computer-aided engineering (CAE) technology is indispensable for MBD[3], and performance studies (strength, sound and vibration, behavior of objects, etc.) that apply various simulation methods (structural analysis, mechanism analysis, etc.) are now used widely.

This article presents a case study using mechanism analysis to investigate the performance of rattle noise generated in the reduction gear of an EPS due to reverse input from the road surface.

2. Simulation of Steering Products

High safety, functionality, and durability are required of steering products because they are responsible for turning, one of the three major actions of an automobile (driving, turning, and stopping). There are also requirements for steerability and quietness related to driver comfort. Because they must be designed to satisfy such a wide range of needs, verification is usually very costly and time-consuming. The aim of MBD is to boost design efficiency by upfront examination of each design stage virtually on a computer. This reduces unexpected failures later in the design process, minimizing the need for expensive real-machine testing[3].

In our steering product design, we have been conducting design studies using computer-based structural analysis since the early 1990s[3]. NSK has been using software since then to address a wide range of requirements such as mechanism analysis and 1D-CAE, as well as structural analysis, in accordance with the V-shaped process development flow. We have developed various analysis methods that can be applied at each stage of the design process. These are based on correlation with test results and intended to improve the validity of analysis results and reproducibility of real-world performance. The analysis methods developed to date cover each stage of the steering system design process (Figure 1).

The mechanism analysis of the reduction gear section for rattle noise, discussed in this article, is at the component level.
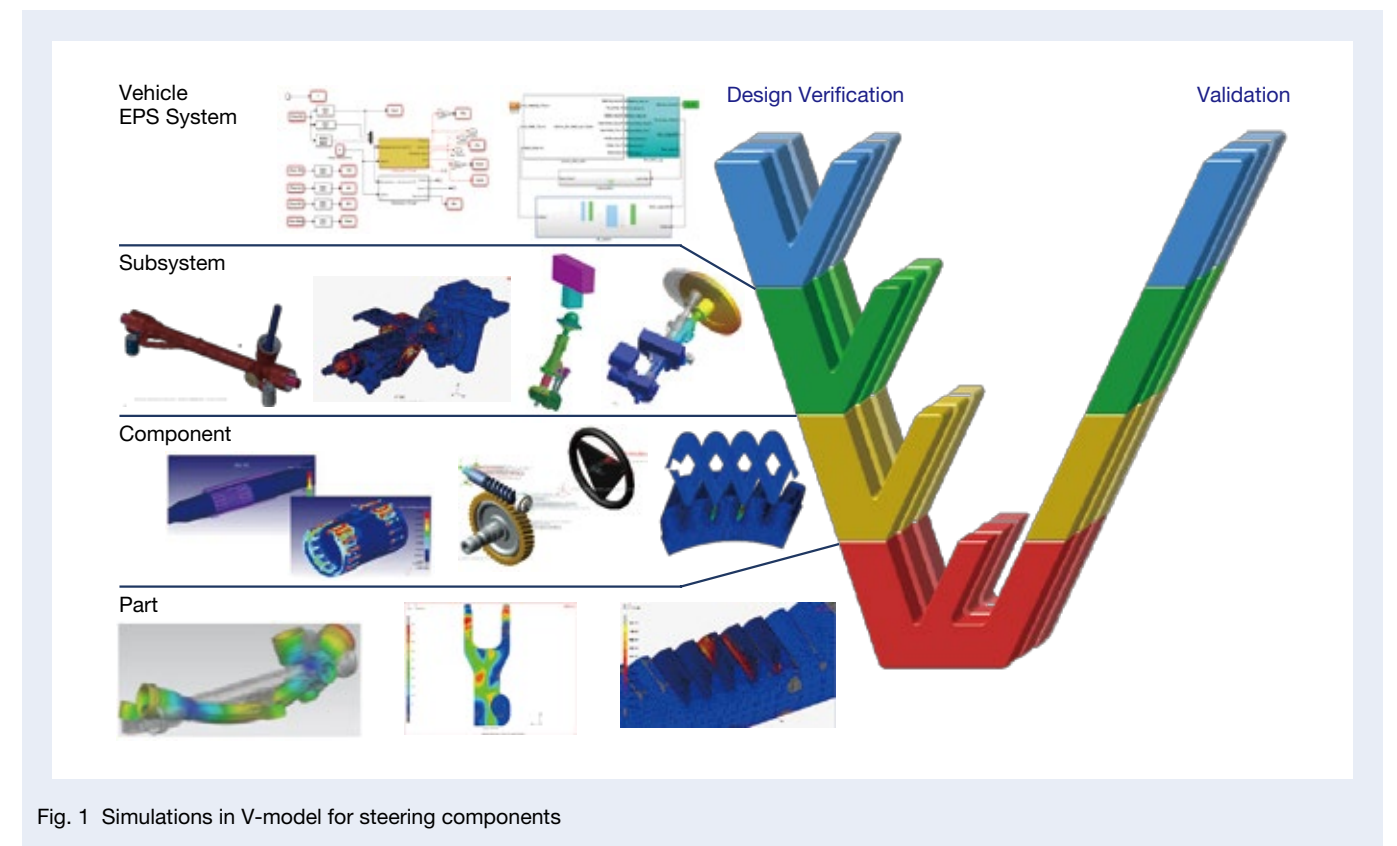

Fig. 1 Simulations in V-model for steering components

3. Mechanism Analysis Model of the Reduction Gear Section

The reduction gear section importantly amplifies the torque output from the motor so that the driver can steer with an appropriate load. The reduction gear section is an important component in considering the EPS's sound and vibration performance because of the backlash (a small gap between the teeth necessary to make gear rotation smooth without undue force) that causes rattle noise.

Figure 2 shows a schematic diagram of the reduction gear section mechanism analysis model. The reduction gear section consists of a worm gear, a support section that supports the worm gear, a connection section between the motor and worm, and a preload section that suppresses the worm gear's backlash with an elastic material to reduce tooth-beating noise during gear reversal.

The reduction gear section mechanism analysis model is modeled by the parts representing the shape and moment of inertia of each component on the rotation axis, springs and friction representing the characteristics between each part. The model is simple except for the contact calculation by importing the 3D shapes of the worm and worm wheel. For example, the support can be modeled in detail by using the 3D geometry of the bearing or by using NSK's bearing calculation program developed in-house. While detailed modeling allows the confirmation of the microscopic behavior of each part, a simple model such as that shown in Figure 2, has the following advantages.

· To achieve the target performance of the reduction gear section, it is possible to investigate the characteristics of each part of the reduction gear components without being limited by the component's shape
· Small computational load

This method can be used to determine the requirements for each section (connection, support, preload, etc.) not only later in the development process, when the detailed shape is fixed, but also earlier, when the shape is still ambiguous. This article presents a case study of its use later in the development process.

Fig. 2 Schematic model of multibody dynamics simulation for the reduction gear section
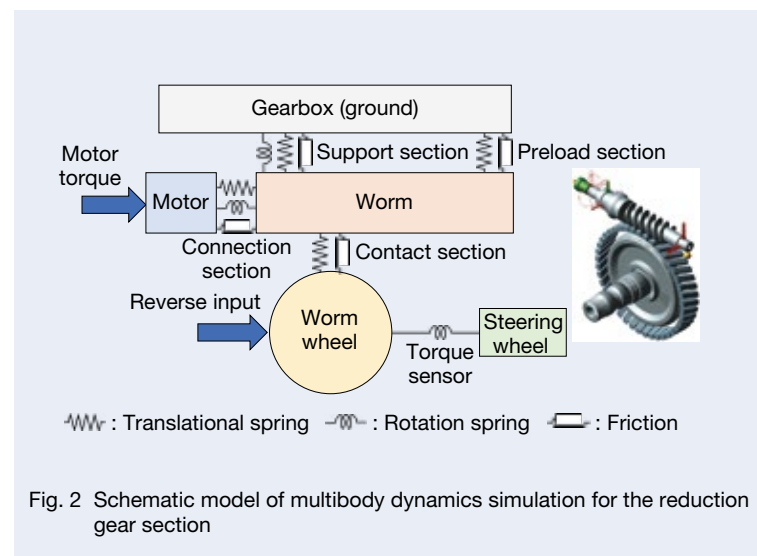
4. Application of Mechanism Analysis to Rattle Noise

In this section, we present a case study in which rattle noise was generated while studying the preload characteristics of a reduction gear. The noise had never been heard before and was resolved through mechanism analysis.

4.1 Mechanism of the target rattle noise

Figure 3 is an overview of the target rattle noise phenomenon. The noise occurs when the reverse input torque (caused by the road surface during rough road driving) entering the worm wheel changes direction and passes through the zero torque point. Torque is applied as a reverse input, and the worm moves in the direction of separation (+Y direction) due to the engagement of the worm gear. Because of backlash in the worm gear, the worm moves rapidly in the −Y direction as the torque decreases. The worm and worm wheel then collide, generating sound and vibration.

Fig. 3 Overview of the rattle noise phenomenon
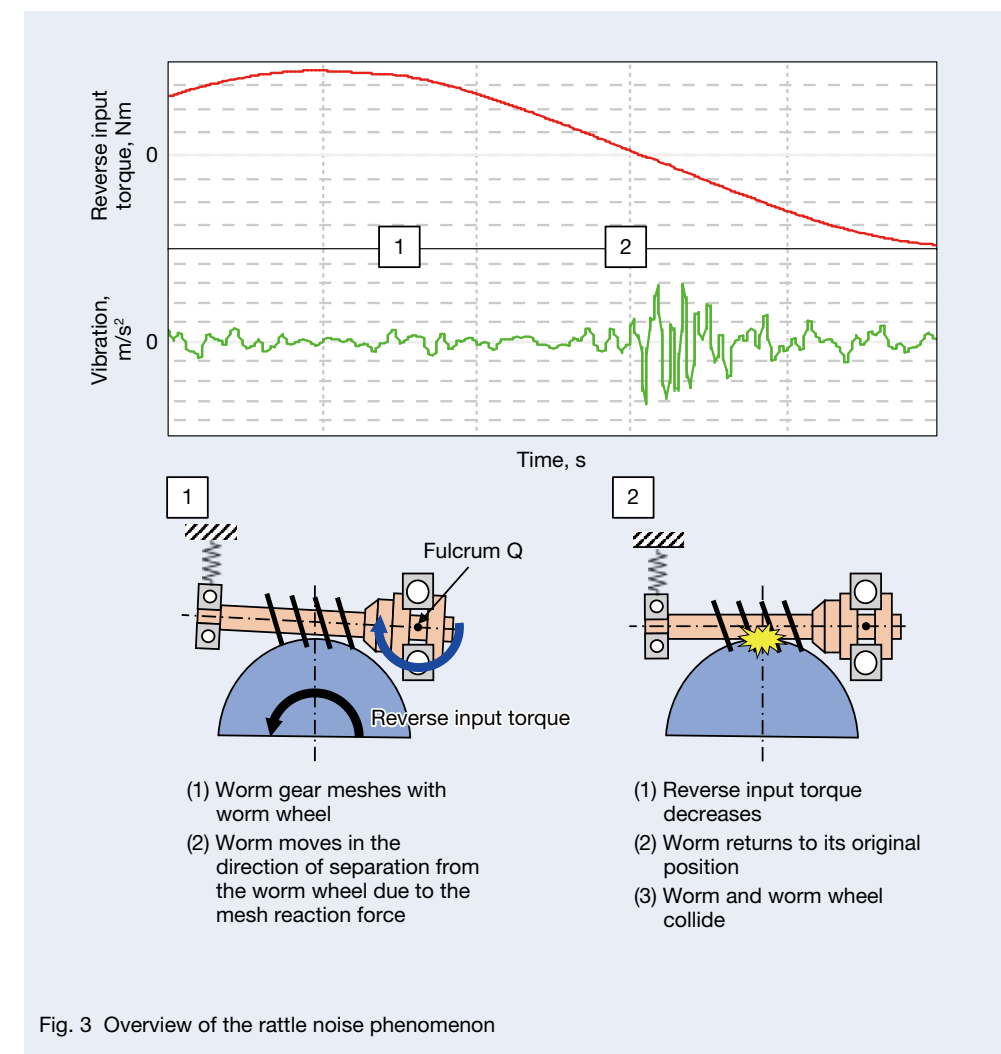
4.2 Comparison of actual and simulated results

The mechanism analysis model used here was introduced in Section 3. As described in Section 4.1, the backlash of worm gears causes rattle noise, so the preload section, which suppresses backlash, was selected for development. The characteristics of other parts were obtained from actual equipment measurements.

The targeted rattle noise is primarily influenced by the behavior of the worm, as indicated in Section 4.1. To confirm the validity of the simulation, the displacement of the worm in each direction was compared between the actual equipment test and the simulation results. The results are shown in Figure 4.

(a) Definition of coordinate system

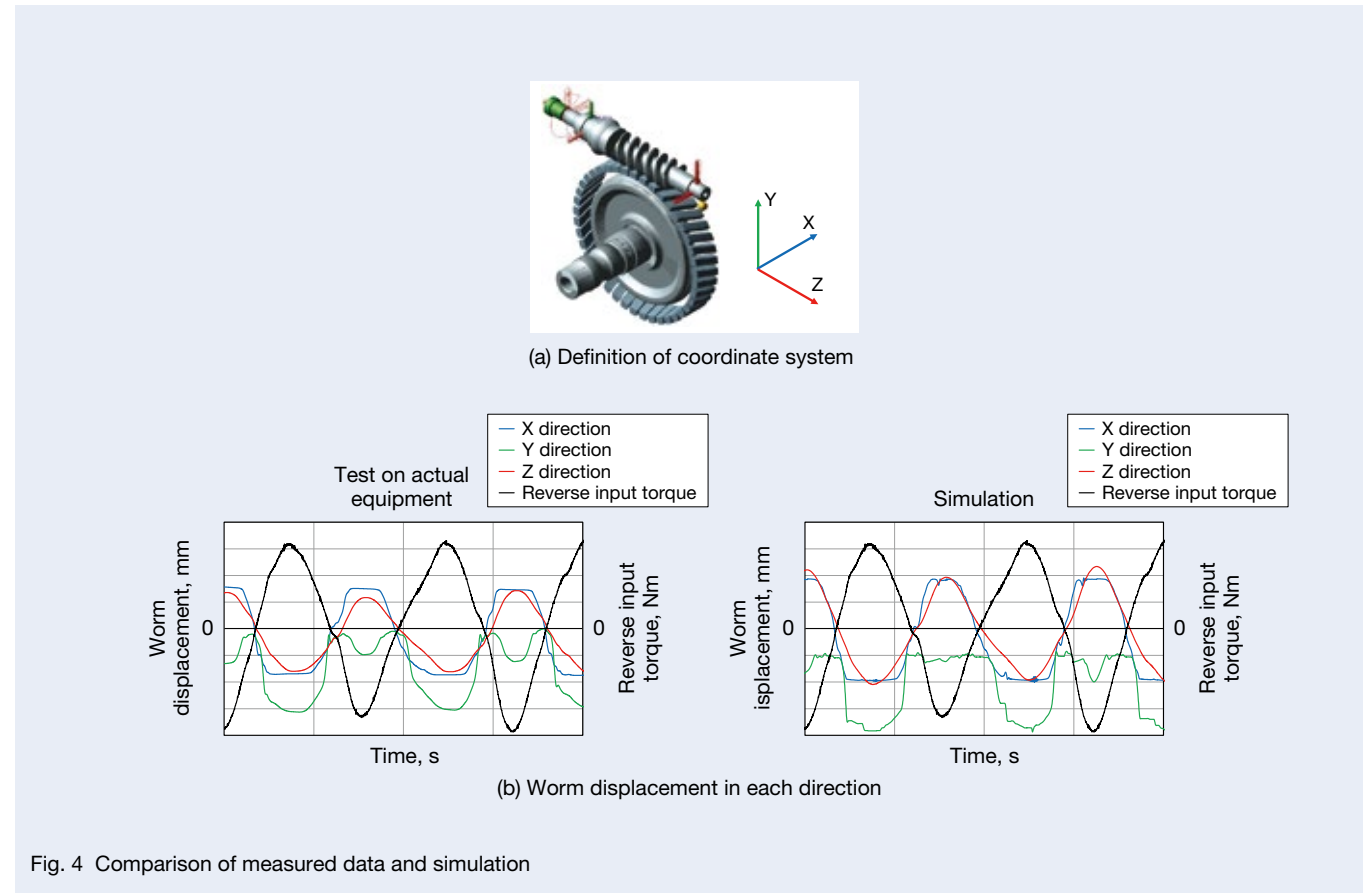(b) Worm displacement in each direction

Fig. 4 Comparison of measured data and simulation

As for the behavior of worm displacement, the simulation still deviates from the actual equipment test. Overall, however, the simulation can represent the behavior of the actual equipment test, especially regarding the timing of the rattle noise that occurs when the reverse input torque crosses the zero point.

Since it is known from the evaluation of the actual equipment that there is a correlation between the vibration that causes the rattle noise and the Y-directional speed of the worm, we next checked whether the same tendency could be obtained in the simulation (Figure 5). Our testing confirmed a correlation between vibration during the actual equipment test and the Y-directional speed in the simulation. This suggests that the simulation model can be effectively used to analyze rattle noise performance.

4.3 Rattle noise performance study

Using the simulation model described in section 4.2, we examined the appropriate preload characteristics to reduce the rattle noise. To efficiently study the preload characteristics, we first conducted a parameter study of the preload characteristics, and two parameters were extracted that have a significant effect on the worm's Y-directional speed, a surrogate characteristic for rattle noise. Next, we checked the relationship between those two parameters and the worm's Y-directional speed (Figure 6). Parameters (1) and (2) are found to be correlated with the worm's Y-directional speed.

Since the preload section must meet various requirements, including those related to the target rattle noise and other rattle noise phenomena, friction, etc., the requirements for the preload section characteristics were determined by simulation. The improvement effect of the preload section designed based on these requirements is shown in Figure 7. Both the worm Y-directional speed in the simulation and the vibration in the actual equipment test after the improvement were reduced to about half the level, indicating that a significant improvement was achieved.
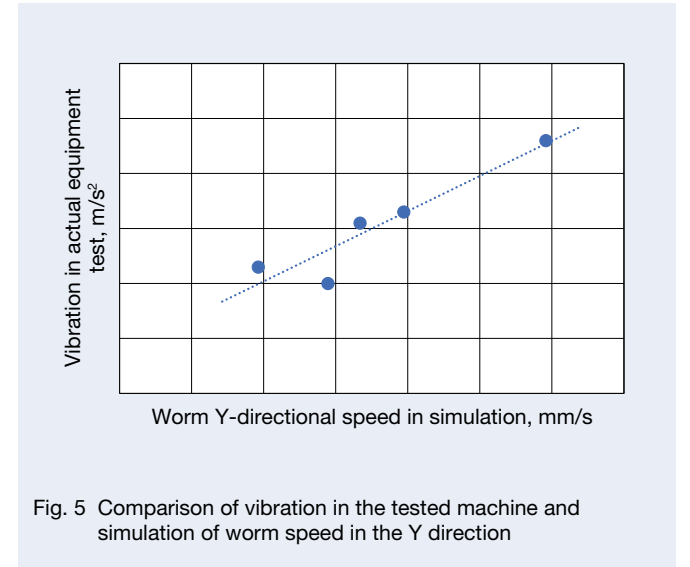

Fig. 5 Comparison of vibration in the tested machine and simulation of worm speed in the Y direction
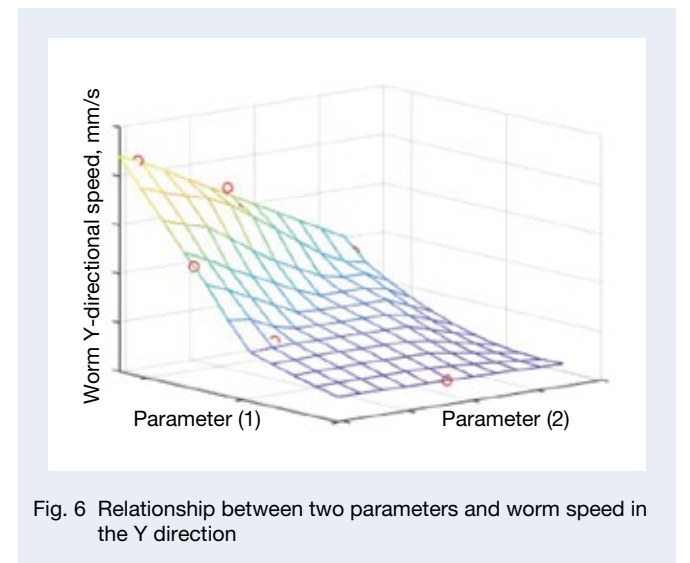

Fig. 6 Relationship between two parameters and worm speed in the Y direction

5. Postscript

In this article, we introduced a case study on the performance using simulation technology to investigate the rattle noise generated in the reduction gear section of the EPS. The case study involved simulation technology at the middle to lower levels of the development process for rattle noise performance. In the future, we will continue to develop simulation technology that can be used at higher levels of the development process and to advance simulation technology to achieve the ultimate goal of simulation in the development process, which eliminates the need for prototype evaluation.

References

1) M. Kanatsu, "Technologies of NV Measurement and Analysis for Steering Systems," *NSK Technical Journal*, No. 692 (2020), pp. 8–23.

2) S. Fujikawa, "Model Based Development in Mazda," *Mazda Technical Review*, No. 31 (2013), pp. 44–47.

3) Y. Uchiyama, R. Habermann, G. Laszlo, and T. Iwai, "Introduction of Analysis Method Automation Technology for Efficient Design," *NSK Technical Journal*, No. 694 (2022), pp. 37–49.
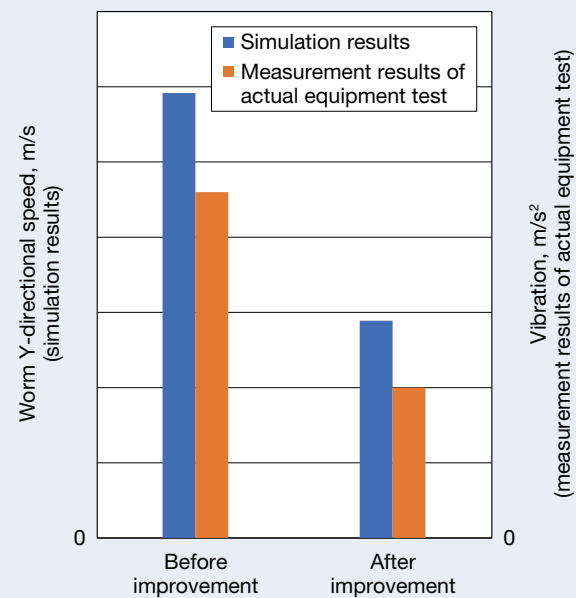
Masahiro Harunaga

Fig. 7 Comparison before and after improvement

Efficient Development for EPS Controls Using Simulation Technology

Tetsuya Kobayashi
System Design Department, Steering & Engineering Center,
NSK Steering & Control, Inc.

Abstract

The automotive industry is undergoing a once-in-a-century transformation, with model-based development proving to be an effective development method for the times. In the development of electric power steering (EPS), NSK has introduced model-based development to improve design efficiency with the use of simulations, particularly in the design of EPS controls. We use simulations in many processes, including system configuration studies, the design of assist control functions, parameter calibrations, and design verification. Here, we introduce actual examples of how simulation technology is used in the development of EPS controls at NSK.

1. Preface

The automotive industry is undergoing a once-in-a-century transformation, and the requirements for electric power steering (EPS) are becoming more sophisticated and complex, including advanced driver-assistance systems (ADAS), automated driving, over-the-air (OTA) updates, and cyber security. Shorter product development cycles and lower costs are also in demand.

One of the most important development methods for overcoming this period of great change is model-based development (MBD). MBD is characterized by the use of models to represent the control function and the control target (plant) and is a method for improving development efficiency through simulation.

NSK has been using MBD on a full-scale basis since the control development of column-type EPS, which it began mass-producing in 2004. In various cases of design and verification, simulation using tools represented by MATLAB®/Simulink® by MathWorks® has been used to improve development efficiency.

The control development of EPS has been discussed in a previous article[1], and here we will look at how simulation technology is used throughout the control development process.

2. Overview of the EPS Control Development Process

Figure 1 shows the control development process for EPS. The main function of EPS is to assist the steering force, which is achieved by driving a motor. EPS control is responsible for precisely controlling the motor so that EPS can generate an appropriate assist force.

In system design, system requirements are defined from customer requirements, and architectural design is performed to assign requirements to components. Here, requirements for the control design are also defined. Control design involves the design of a controller function based on system requirements, including design verification. The deliverable is a control model. Software implementation involves optimizing control model resolution conversion and variable definition and includes mass production code generation performed by an automatic code generation tool. NSK mainly uses dSPACE's TargetLink as an automatic code generation tool. The system is then integrated with functions outside the MBD process and comprehensively tested as an EPS system, including self-diagnostic functions and durability.

Various simulation technologies are used in the EPS control development process, including design, implementation, and testing. This article discusses the use of simulation in control design, which has the longest history of MBD at NSK. The article also touches on the use of simulation in system design, an upstream process closely related to control design.
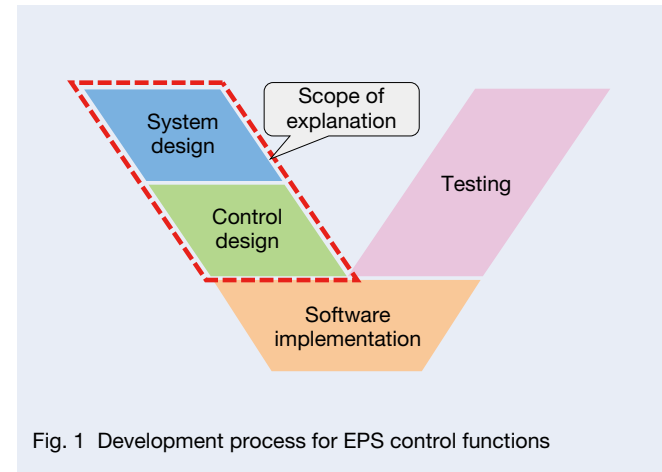
Fig. 1 Development process for EPS control functions

3. Application Examples in Control Design

Figure 2 shows a schematic block diagram of the EPS control. Conventional assist control primarily calculates target assist characteristics based on the driver's steering information and vehicle speed information and controls the motor to achieve the calculated target characteristics. However, with the growing popularity of ADAS functions these systems now require controlling the steering wheel angle based on the vehicle's inputs. The ADAS function and assist control are not exclusive, and the driver can steer the vehicle at any time during the ADAS function's control of the steering angle. Coordination between the ADAS function and conventional control is therefore crucial. With the increasing complexity of control, the use of simulation is also important to promote rapid development. In this section, we introduce a simulation application example in actual control design using this ADAS function as a subject (Figure 3).

Fig. 3 Case study using simulations for control design

Fig. 2 Block diagram of EPS control functions

3.1 Control design with MILS

In the ADAS function, the camera unit requests the target steering angle from the EPS via the in-vehicle network. The EPS must control the steering angle to enable the actual steering angle to follow the target steering angle. In a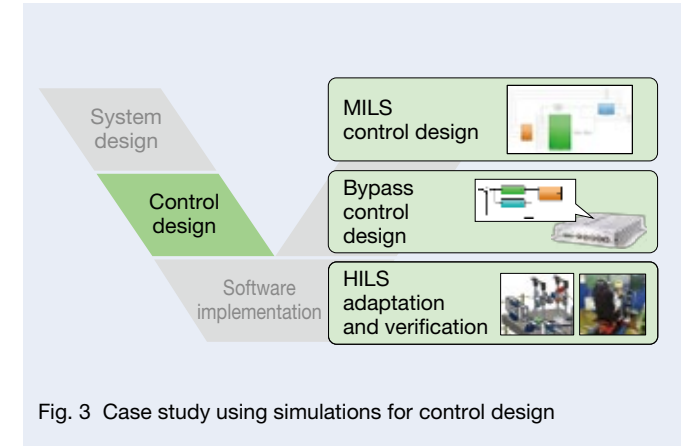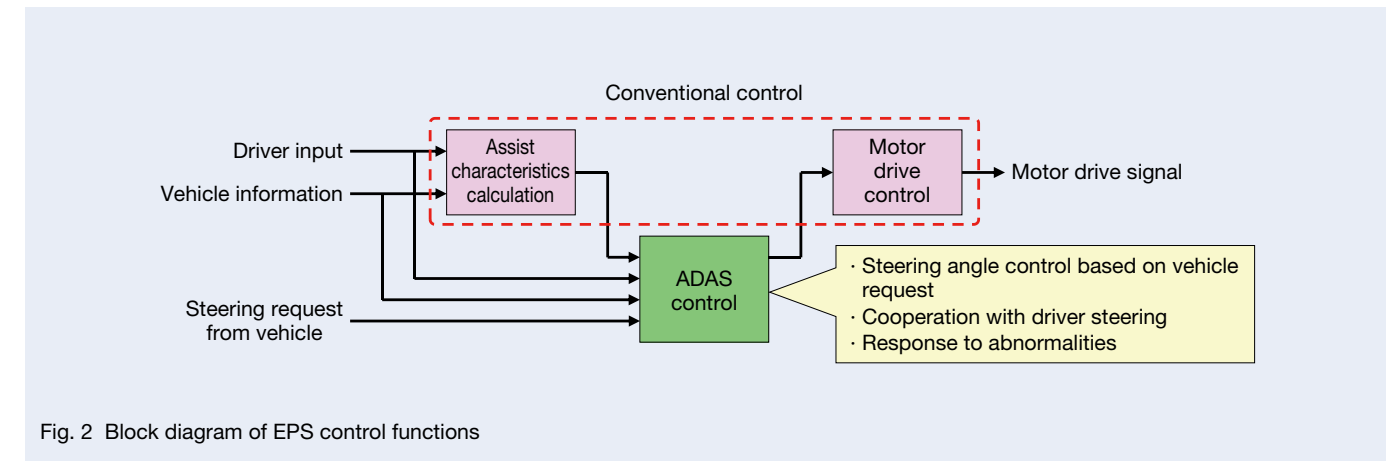ddition to these ADAS functions, we are using model-in-the-loop simulation (= MILS) as the first step in functional design, including cooperative control with conventional assist control.

In functional design by MILS, the control function and control target (plant) are modeled. Plant models include vehicle models for generating target steering angles and expressing load characteristics, mechanical models for the mechanical elements of steering, and electrical models for the behavior of sensors and motors. These plant models are combined according to purpose to construct the MILS environment.

Because NSK uses Simulink to design the control, the plant model also uses Simulink or commercially available vehicle simulation software that can be integrated with it.

When building a plant model in Simulink, it is necessary to model each element based on physical equations. Since the basic mechanism of steering has many common parts, each element model is managed as a library so that it can be used in various projects, thereby improving the efficiency of model creation.

In vehicle simulation software, the entire vehicle is pre-modeled, including elements necessary for the development of ADAS functions such as cameras and radar. Simply replacing the pre-model with the part to be developed allows for a simulation including the vehicle behavior. NSK owns HILS manufactured by IPG Automotive, and the company's simulation platform, CarMaker, is also used in MILS to develop ADAS functions.

Simulink also provides a wealth of functions for model verification. One can implement tests with varying levels of granularity and from different perspectives on the control model of the development target. The process at the MILS stage helps boost the completion level of the development target functions.

3.2 Control design using bypass

Although the MILS environment enables basic control design, situations remain where actual equipment is preferred in design evaluation, such as the steering feel when the driver steers the vehicle during ADAS function operation. In such cases, the bypass method, a type of rapid control prototyping (RCP), is used.

In the bypass method, a processor in the actual ECU and a real-time computer are connected by a debug interface or other means, and only some functions of the EPS are calculated on a real-time computer (Figure 4). The advantage of the bypass is that the control model designed by MILS can be easily operated at the IO interface and execution timing of the actual equipment. In addition, because the control model is running on a real-time computer, any functional changes can be made in just a few minutes. Compared to creating software for testing, a significant reduction in working hours is possible. In this case study, MicroAutoBox II from dSPACE was used as the real-time computer for bypass.

Functions to be developed are calculated by a computer outside the ECU, and the calculation results are returned to the ECU
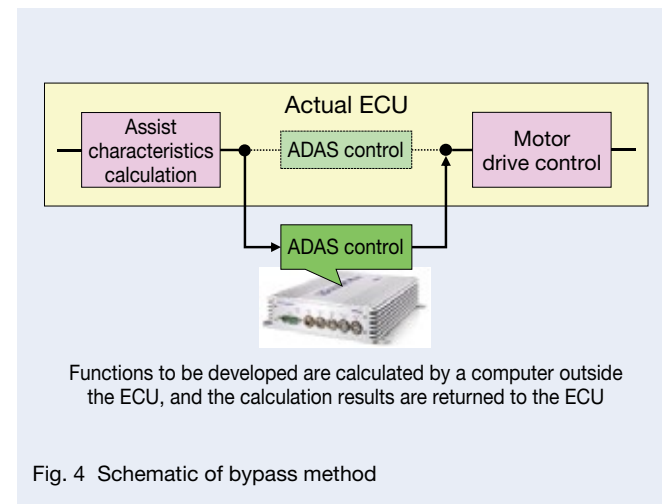
Fig. 4 Schematic of bypass method

3.3 Adaptation and verification using HILS

NSK is working to reduce the use of actual vehicles as much as possible from the viewpoints of safety and cost. In the development of ADAS functions, hardware-in-the-loop simulation (= HILS) is used as a substitute for actual vehicles. Figure 5 shows the difference between MILS and HILS.

In MILS, both the steering system and the vehicle to be developed are models. In HILS, the vehicle is the model, while the steering system is the actual equipment. IPG Automotive's HILS, used in this case study, can apply the same CarMaker as the MILS environment so that the same vehicle models can be employed.

In the ADAS function development, HILS equipped with an actual steering system allowed for the building of more detailed functions and adapting parameters, using the bypass method based on the functions designed in MILS. In addition, HILS allows the driver to operate the actual steering wheel. HILS thus enables efficient design in a short time while minimizing the use of actual vehicles, although the coordination between the steering control by the ADAS function and the driver's steering requires sensory and sensitive characteristics.

In addition, HILS can be also used for verification work. The customer presented more than 100 evaluation conditions for the characteristics of ADAS functions, especially steering angle tracking. Since evaluating all of these manually is time-consuming, HILS, discussed in the previous section, was automated to handle this task (Figure 6).
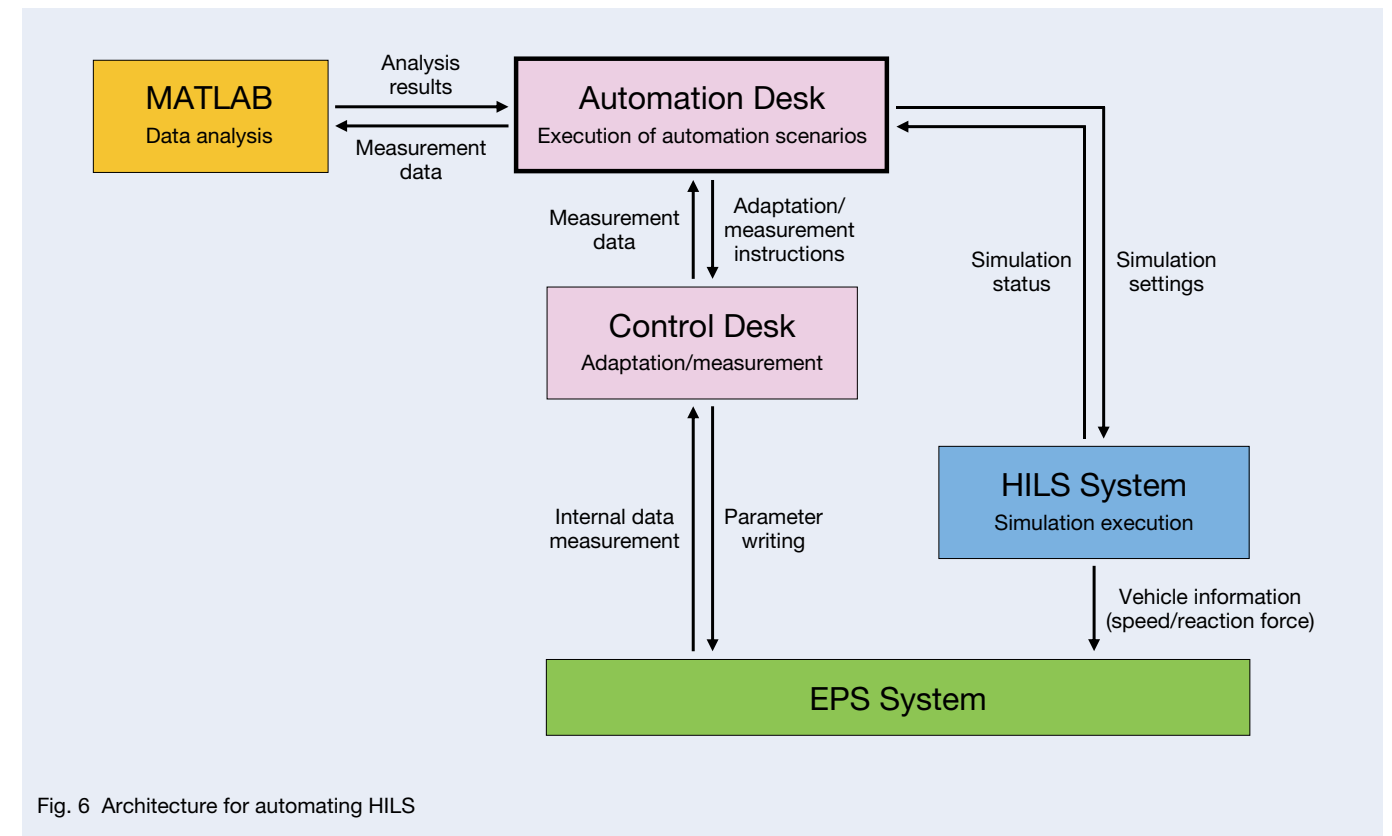

Fig. 5 Difference between MILS and HILS

Fig. 6 Architecture for automating HILS

AutomationDesk from dSPACE was used for automation control. For adaptation and measurement control, we employed the company's ControlDesk, which supports measuring internal EPS-ECU data. Since simulation conditions such as vehicle speed had to be set in the HILS system, we used an API to link with AutomationDesk. Controlling MATLAB from AutomationDesk and executing analysis scripts automated the pass/fail judgment of the steering angle tracking performance and the generation of reports. This automation series could shorten the time required for evaluation from several days, if done manually, to about three hours.

Figure 7 compares the tracking of the actual steering angle to the target steering angle and the control output of the ADAS function between MILS and HILS after the design and verification were completed in this way. It should be noted that the MILS results are quite close to the HILS results using the actual steering system, and the completeness of the MILS plant model is important to obtain these results.

HILS enables efficient design, reduces rework in the development of ADAS functions, and reduces the amount of work required in actual vehicles, thereby contributing to safety and cost-saving.

4. Examples of Use in System Design

In system design, a high-level process of control design, after defining system requirements, requirements are assigned to each component based on architecture. At this time, it is necessary to proceed with the work while confirming its feasibility as a system.

This section presents examples of simulation applications in system design (Figure 8).
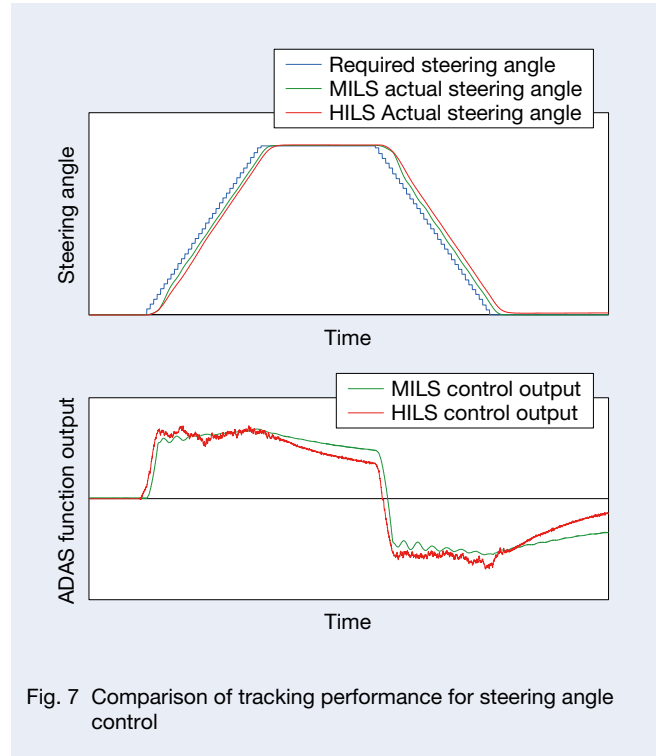

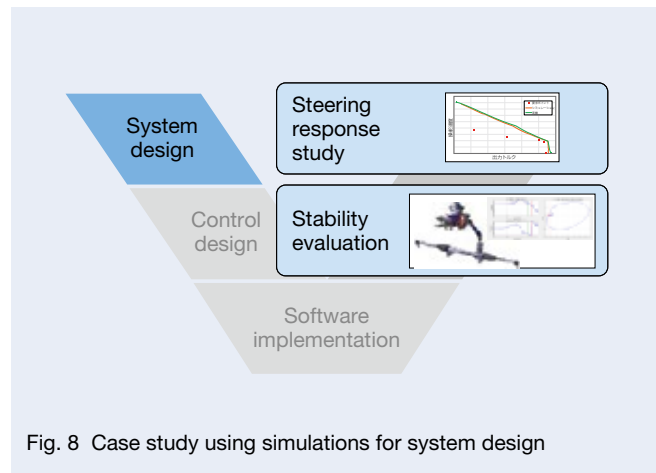Fig. 7   Comparison of tracking performance for steering angle control

Fig. 8   Case study using simulations for system design

4.1 System steering response examination

An EPS's primary functional requirement is the generation of assist force, and its typical performance requirement is output steering response. The customer requires the steering response to be in the form of rack thrust or column shaft output. The initial stage of system design needs to consider the system configuration that can satisfy this steering response requirement.

Many steering response studies use a simplified one-degree-of-freedom model for the steering mechanism. On the other hand, the motor drive control and motor model use a detailed model because it is necessary to check that the supply voltage and current consumption constraints can also be satisfied.

Figure 9 shows an example of a waveform that superimposes the customer's requirements, simulation study results, and measurement results of the actual steering response. The simulation study showed that the proposed specifications have sufficient performance for the requirements. Subsequent comparisons with the measured results of the actual equipment show that the simulation results are quite similar in characteristics to those of the actual equipment.

Simulation has therefore facilitated the system configuration study that satisfies the output steering response in the initial stage of system design.

4.2 System stability evaluation

The EPS can change the assist characteristics by adjusting the control function parameters, but some

parameters may cause the system to become unstable. For this reason, the system's stability is evaluated in advance, and the adjustable range of parameters is predefined.

Conventionally, the system stability of EPS has been evaluated using actual equipment. However, actual equipment evaluation still led to several problems. Extensive preparation was required, including arranging specimens and measuring instruments, setting them up on a table, and configuring the measuring instruments. Furthermore, the number of data measurement patterns increased significantly when considering the combinations of parameters of each function, input signals, and load conditions. We therefore modeled all components and attempted to evaluate their stability by full simulation.

The overall model was built in Simulink, and the assist control and electrical components, such as motors, were also created in Simulink. The mechanical components were divided into columns, motor, reduction gear, intermediate shaft, and rack and pinion. They were modeled using a non-causal modeling tool and then integrated with the overall model in Simulink.

Figure 10 shows the waveforms of the stability simulation using the model after measuring and identifying the stability data of the actual equipment with several parameter combinations. The simulation results captured the characteristics of the actual equipment results well, establishing the model as a useful tool for determining the gain margin and phase margin, which are stability evaluation indices. This model enabled simulations to evaluate stability with various combinations of parameters.
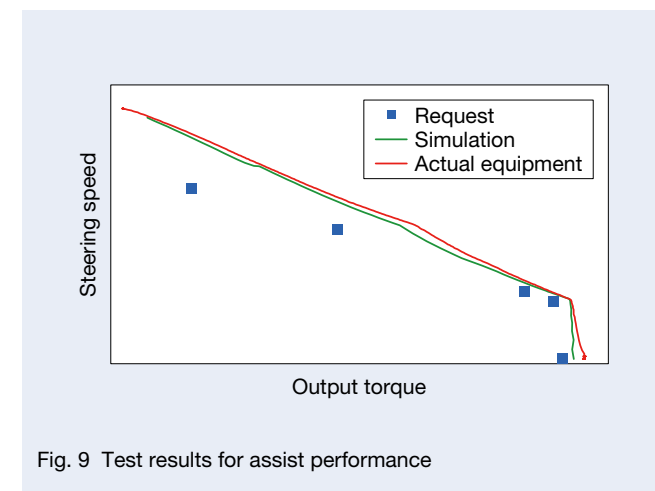

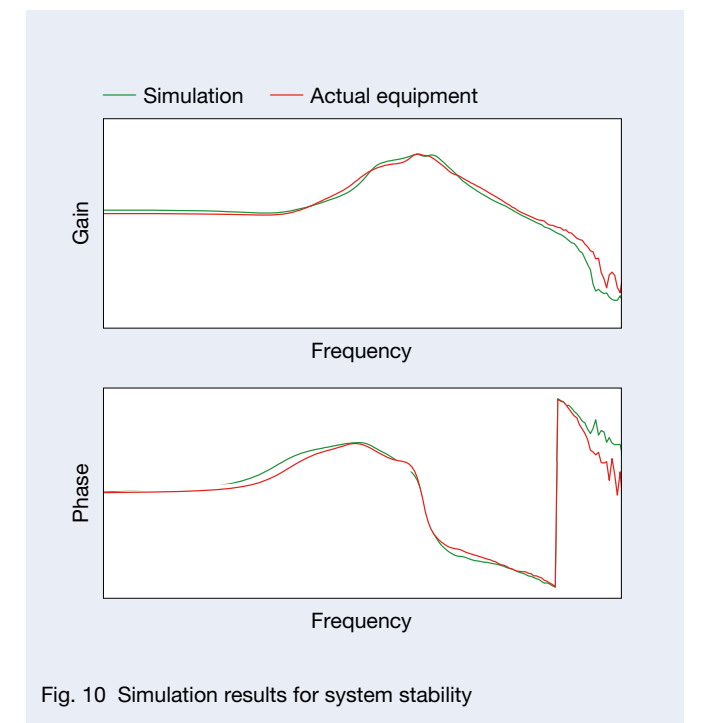Fig. 9   Test results for assist performance

Fig. 10   Simulation results for system stability

5. Postscript

This article has presented several examples of efficient EPS control development using simulation technology. NSK has been using MBD for EPS control development for about 20 years and has been developing EPS efficiently by using simulation technologies. In recent years, there have been an increasing number of opportunities to provide simulation models at customers' requests, and factors such as ease of coupling with other vehicle components are also in demand. We will continue to improve development efficiency through further use of simulation technologies.

Reference

1) S. Shimokawabe and T. Kitazume, "NSK EPS Control Technology," *NSK Technical Journal*, No. 689 (2017), pp. 51–57.

Tetsuya Kobayashi

Lubrication Condition Monitoring of Practical Ball Bearings by Electrical Impedance Method

Taisuke Maruyama, Masayuki Maeda
Core Technology R&D Center, NSK Ltd.
Ken Nakano
Faculty of Environment and Information Sciences, Yokohama National University

Abstract

In this study, the electrical impedance method was developed to monitor the thickness and breakdown ratio of oil films in elliptical elastohydrodynamic (EHD) contacts of practical ball bearings. First, it is theoretically shown that the oil film thickness and breakdown ratio can be simultaneously measured from the complex impedance generated when a sinusoidal voltage is applied to elliptical contacts. Subsequently, lubrication conditions of practical ball bearings were monitored at an ambient temperature to verify the measurement accuracy of the developed method. The oil film thickness in the low-speed range was consistent with the theoretical value calculated by Hamrock–Dowson equation. However, in the high-speed range, the oil film was thinner than the theoretical value considered an ambient temperature. In this high-speed range, the results of both the outer ring temperature and bearing torque revealed that the viscous shear heating and starvation were occurring simultaneously, thus supporting that the measured thickness would be thinner than the theoretical value. Besides, the developed method can also measure the breakdown ratio, confirming that it increases in the low-speed range where the bearing torque increases. That is, it indicates that not only the oil film thickness but also the breakdown ratio can be evaluated quantitatively.

Keywords

electrical impedance method, condition monitoring, oil film thickness, breakdown ratio, elastohydrodynamic lubrication, ball bearing

1. Introduction

In recent years, global warming [1] has led to increased demands for further decreases in the torque of rolling bearings used for rubbing parts in various machines. To reduce the bearing torque, the viscosity or amount of lubricant may be reduced. However, these approaches induce breakdown of oil films in elastohydrodynamic (EHD) contacts [2] of rolling bearings, causing various surface damages [3–5]. Therefore, the ideal lubrication condition to further reduce the bearing torque is a state in which the oil film has the thinnest thickness achievable but does not break down. Therefore, the oil film thickness and the breakdown ratio in EHD contacts are especially important as indexes of lubrication conditions.

There have been various studies conducted on conventional methods of monitoring lubrication conditions in EHD contacts [6]. Optical interferometry [7–14] is widely used as it is well suited for measuring the oil film thickness in EHD contacts with high accuracy. Johnston et al. [7] developed the optical method which measured molecularly thin films (i.e., several nm) with high accuracy by applying a SiO₂ spacer layer on a glass disc. The optical method also allows for detailed understanding of oil film distribution in EHD contacts; thus, it has been applied to measure the oil film thickness under non-steady states [8–11], abnormal film shapes [12, 13], or temporal change in the thickness of adsorbed films [14]. However, the material must transmit light for the optical method to work, which means that lubrication conditions of practical bearings cannot be visualized. As methods for monitoring lubrication conditions in steel/steel contacts that do not transmit light, electrical methods have been generally proposed. Electrical methods are classified into three: electrical resistance method [15–20], electrical capacitance method [21–24], and electrical impedance method [25–29].

First, the electrical resistance method measures the breakdown ratio of oil films by measuring electrical resistance in EHD contacts. Therefore, this method has been mainly used to elucidate the friction or wear mechanism under the mixed lubrication. For instance, Lugt et al. [18] and Load et al. [19] reported on the relationship between surface roughness and breakdown ratio by using the electrical resistance method.

Meanwhile, the electrical capacitance method measures the oil film thickness in EHD contacts from the measured electrical capacitance. Jablonka et al. [23, 24] showed that the oil film thickness was measured with high accuracy comparable to that of the optical method by considering the electrical capacitances not only the inside but also the outside contact area. In general, there are two types of the outside contact area. One is the area filled with oil, and the other is the cavitation area not filled with oil. They assumed that about 25% of the oil-filled area is the cavitation area that it remains constant. However, the size of the cavitation area has been reported to vary based on test conditions [30–32]. Besides, under the starved lubrication, the area not filled with oil exists in the inlet of contact area [33–36], which means the surrounding area in EHD contact not filled with oil is not constant. Furthermore, the electrical capacitance method cannot be applied to monitoring lubrication conditions under the mixed lubrication since oil films partially collapse.

Recently, the electrical impedance method has been proposed that simultaneously measures the oil film thickness and the breakdown ratio from the complex impedance measured by applying a sinusoidal voltage to contact areas. This method has an advantage of being able to measure the oil film thickness under the mixed lubrication. Nakano et al. [25, 26] developed the electrical impedance method to investigate into the breakdown process of oil films between metal surfaces, in which mercury was used as a counter surface of a steel surface. By using mercury as a lower specimen, it can be assumed that the apparent contact area is equivalent to the area of capacitor electrodes. Thus, it indicates that the oil film thickness and breakdown ratio can be evaluated quantitatively. However, as it uses mercury, EHD contacts are not the target.

Studies that applied the electrical impedance method to EHD contacts include those by Schnabel et al. [27], Nihira et al. [28], and Maruyama et al. [29]. Schnabel et al. [27] measured the complex impedance in EHD contacts under the mixed lubrication in order to simultaneously monitor the oil film component (i.e., the electrical capacitance) and the breakdown component (i.e., the electrical resistance). However, they did not calculate the thickness and breakdown ratio of oil films. In contrast, Nihira et al. [28] made quantitative measurements of the oil film thickness and breakdown ratio simultaneously when a ball collided with a plate coated with a thin layer of lubricating oil. However, as it is unknown how much of the surround EHD contact is filled with the lubricating oil, they ignored the capacitance in the surrounding area. Maruyama et al. [29] took the capacitance in the surround EHD contact into consideration, and discovered that the oil film thickness could be measured with high accuracy comparable to the optical interferometry. However, as this is a method that targets a ball-on-disc-type apparatus (i.e., a point contact), it cannot be applied to a practical ball bearing (i.e., elliptical contacts), where two rubbing surfaces have different curvatures.

Therefore, in this study, we improved the conventional electrical impedance method [29] and derived theoretical equations for the thickness and breakdown ratio of oil films in elliptical EHD contacts. The developed method is able to monitor lubrication conditions of practical bearings with high accuracy; thus, we believe that it would be an extremely important technique in achieving both lower torque and longer life of bearings.

2. Measurement principle

This paper focuses on the lubrication condition monitoring in elliptical EHD contacts of practical ball bearings. In the proposed method, a sinusoidal voltage is applied to contact areas of bearings, and the complex impedance is measured as a response. Using the modulus and phase of the measured impedance, the oil film thickness and breakdown ratio of contacts are quantified. For the quantifications, two types of models (i.e., a "geometrical model" and an "electrical model") of contacts are needed.

2.1 Geometrical model

First, let us consider the geometrical model of the contact area of deep groove ball bearings. The raceways of the inner and outer rings of bearings have grooves to guide the rolling elements, which make elliptical contacts in shape. As the curvature radii of the inner and outer rings are different, the oil film thickness in each contact is also different [37]. Meanwhile, if the developed method is applied to practical bearings, only the total value of the complex impedance Z generated in all contact areas can be measured. In short, it is impossible to measure the oil film thickness and breakdown ratio in each contact, respectively. Therefore, as shown in Fig. 1, the present study assumed all contacts in a rolling bearing as a contact between ellipsoid and plane, and obtained the mean values of oil film thickness and breakdown ratio. Here, $\bar{r}_x$ is the semi-axis of the ellipsoid in the x-axis direction (i.e., in the rolling direction of the rolling element), $\bar{r}_y$ is the semi-axis of the ellipsoid in the y-axis direction (i.e., perpendicular to the rolling direction), and $\bar{r}_h$ is the semi-axis of the ellipsoid in the h-axis direction, which are defined by the following equations:

$$\bar{r}_x = (r_{x1} + r_{x2}) / 2 \qquad \cdots\cdots (1)$$

$$\bar{r}_y = (r_{y1} + r_{y2}) / 2 \qquad \cdots\cdots (2)$$

$$\bar{r}_h = (\bar{r}_x + \bar{r}_y) / 2 \qquad \cdots\cdots (3)$$

where r_{x1} is the effective radius between rolling element and inner ring in the x-axis direction, r_{x2} is the effective radius between rolling element and outer ring in the x-axis direction, r_{y1} is the effective radius between rolling element and inner ring in the y-axis direction, and r_{y2} is the effective radius between rolling element and outer ring in the y-axis direction. As shown in Eq. (3), $\bar{r}_h$ is defined as the average value of $\bar{r}_x$ and $\bar{r}_y$ because the curvature radii of the ellipsoid in the x-axis and y-axis directions are affected by not only $\bar{r}_x$ and $\bar{r}_y$ but also $\bar{r}_h$. In other word, $\bar{r}_h$ is defined so as to affect the curvature radii of the ellipsoid in the x-axis and y-axis directions equally. Therefore, the

formula $h(x, y)$ that describes the gap between ellipsoid and x-y plane is expressed as follows:

$$(x / \bar{r}_x)^2 + (y / \bar{r}_y)^2 + ((h_3 - h(x, y)) / \bar{r}_h)^2 = 1 \qquad \cdots\cdots (4)$$

where h_3 is the height from the x-y plane to the center of the ellipsoid, satisfying $h_3 \geq h(x, y)$. Note that we regarded it as an ideal ellipsoid (i.e., no elastic deformation). In addition, we defined the mean values $\bar{a}$ and $\bar{b}$ of the semimajor and semiminor axes of all contact ellipses as the following equations:

$$\bar{a} = (a_1 + a_2) / 2 \qquad \cdots\cdots (5)$$

$$\bar{b} = (b_1 + b_2) / 2 \qquad \cdots\cdots (6)$$

where a_1 and b_1 are the semimajor and semiminor axes of the contact ellipse in the inner ring, a_2 and b_2 are the semimajor and semiminor axes in the outer ring, respectively. Note that the developed method can be applied when only an axial load is applied to practical ball bearings (i.e., when all contact ellipses are the same size). When a radial load is applied, all contact ellipses are not constant, which means that the developed method is not applicable.
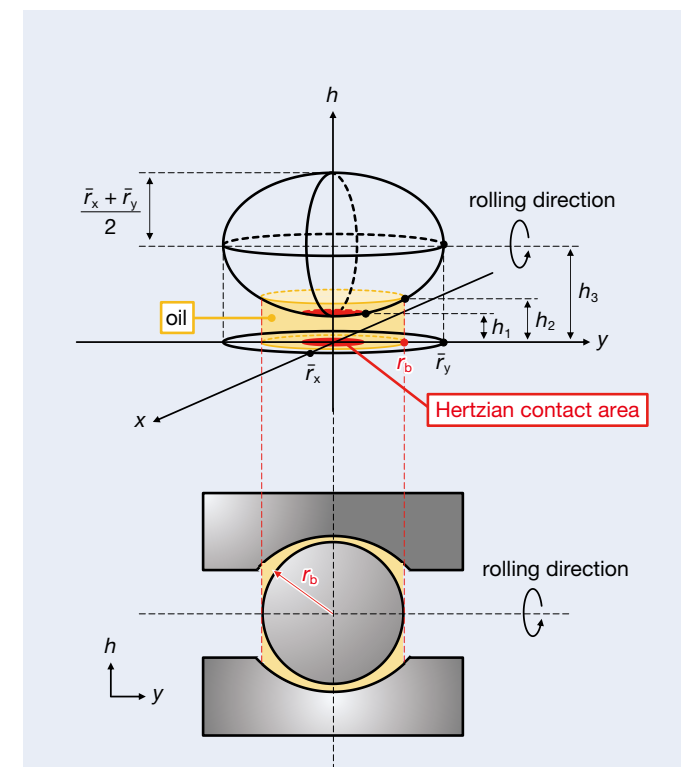

Fig. 1 Consideration of effective radius of deep groove ball bearing.

Subsequently, Fig. 2 shows the geometrical models of the ellipsoid in the x-axis and y-axis directions. Note that not only the "contact area" but also its "surround area" is considered. Here, h_1 is the thickness in oil film formed area within EHD contacts, r_b is the radius of the rolling element, S_1 is the EHD contact area ($\approx$ the Hertzian contact area), S_2 is the surround area of the x-y plane filled with oil, and α is the breakdown ratio of oil films (i.e., $0 \leq \alpha \leq 1$). If we assume that the oil film thickness h_1 is constant shown in Fig. 2, the Hertzian contact ellipse does not exist in any cross-section of the ellipsoid expressed by Eq. (4) because $\bar{a} : \bar{b} \neq \bar{r}_y : \bar{r}_x$. Thus, we defined a new contact ellipse satisfying its contact area $S_1 = \pi \bar{a} \bar{b}$ and semimajor axis: semiminor axis $= \bar{r}_y : \bar{r}_x$. The newly defined semimajor axis of contact ellipse $\bar{a}'$ and semiminor axis $\bar{b}'$ can be expressed using the following equations:

$$\bar{a}' = \sqrt{\bar{a}\,\bar{b}\,\bar{r}_y / \bar{r}_x} \qquad \cdots\cdots (7)$$

$$\bar{b}' = \sqrt{\bar{a}\,\bar{b}\,\bar{r}_x / \bar{r}_y} \qquad \cdots\cdots (8)$$

Therefore, h_3 of Eq. (4) can be obtained from Eqs. (7), (8):

$$h_3 = h_1 + \bar{r}_h \sqrt{1 - \bar{a}\,\bar{b} / \bar{r}_x \bar{r}_y} \qquad \cdots\cdots (9)$$

Furthermore, as shown in Figs. 1, 2, we assumed that the surround area is completely filled with the lubricating oil in the y-axis direction up to $y = r_b$. The maximum oil film thickness h_2 in the surround area filled with the oil is expressed as Eq. (10) from Eq. (4) as $h_2 = h (x, y) = h (0, r_b)$:

$$h_2 = h_3 - \bar{r}_h \sqrt{1 - (r_b / \bar{r}_y)^2} \qquad \cdots\cdots (10)$$

Meanwhile, we cannot assume that the surround area is filled with the oil in the x-axis direction up to $x = r_b$ since $\bar{r}_x < r_b$. Therefore, as shown in Fig. 2, we assumed that it is filled up to the distance of $x = r_b'$ that satisfies $h (r_b', 0) = h_2$ in the x-axis direction. From Eqs. (4), (10), r_b' is obtained by Eq. (11):

$$r_b' = r_b \bar{r}_x / \bar{r}_y \qquad \cdots\cdots (11)$$

In short, in the case of an elliptical EHD contact, the thickness $h (x, y)$ in the breakdown area is expressed with Eq. (12), $h (x, y)$ in the lubricated area is expressed with Eq. (13), and $h (x, y)$ in the surround area is expressed with Eq. (14), respectively:

$$h (x, y) = 0 \qquad \cdots\cdots (12)$$

$$h (x, y) = h_1 \qquad \cdots\cdots (13)$$

$$h (x, y) = h_3 - \bar{r}_h \sqrt{1 - (x / \bar{r}_x)^2 - (x / \bar{r}_y)^2} \qquad \cdots\cdots (14)$$

2.2 Electrical model

Figure 3 shows the equivalent circuit assuming ball bearings, where R_1 is the electrical resistance in the breakdown area, C_1 is the capacitance in the lubricated area, and C_2 is the capacitance in the surround area. Each value is a physical quantity per contact area. Actually, the curvature radii of the inner and outer rings are different, and the oil film thickness in each EHD contact is also different; thus, the above R_1, C_1, and C_2 are different between rolling element and inner/outer rings [22]. However, as shown in Fig. 1, we considered a simple contact of the ellipsoid whose semi-axes are the mean values of the effective radii between rolling element and inner/outer rings. Therefore, in this study, the R_1, C_1, and C_2 were assumed to be equal between rolling element and inner/outer rings, which means that all contact areas of ball bearing have the same complex impedance under the axial load. Moreover, as shown in Fig. 3, we assumed that contact areas of the inner and outer rings are connected in series circuits, while all rolling elements are connected in parallel circuits. In this situation, R_1, C_1, and C_2 can be expressed using the following equations:

$$R_1 = R_{10} / \alpha \qquad \cdots\cdots (15)$$

$$C_1 = \varepsilon (1 - \alpha) S_1 / h_1 = \pi \varepsilon (1 - \alpha) \bar{a}\,\bar{b} / h_1 \qquad \cdots\cdots (16)$$

$$C_2 = \varepsilon \int_{\frac{r_b}{a'}} \int_{\frac{r_b'}{b'}} (1 / h (x, y)) \, dx dy \qquad \cdots\cdots (17)$$

where ε is the dielectric constant of the lubricating oil, and R_{10} is the electric resistance under the stationary contact (i.e., $\alpha = 1$). By using Eqs. (7) – (9), (11), (14), Eq. (17) can be expressed as follows:

$$C_2 = 2\pi \varepsilon \bar{r}_x \bar{r}_y (h_3 \ln (h_2 / h_1) + h_1 - h_2) / \bar{r}_h^2 \qquad \cdots\cdots (18)$$

Generally, $\bar{r}_x \gg \bar{b}$, $\bar{r}_y \gg \bar{a}$, and $\bar{r}_h \gg h_1$; thus, Eq. (18) can be approximated as Eq. (19):

$$C_2 \approx 2\pi \varepsilon \bar{r}_x \bar{r}_y (\ln (\psi \bar{r}_h / h_1) - \psi) / \bar{r}_h \qquad \cdots\cdots (19)$$

where ψ is a dimensionless constant expressed with the following equation:

$$\psi = 1 - \sqrt{1 - (r_b / \bar{r}_y)^2} \qquad \cdots\cdots (20)$$

Note from Eq. (19) that C_2 is independent on both $\bar{a}$ and $\bar{b}$.

2.3 Complex impedance analysis

In the complex form, the alternating voltage $V = V (t)$ (as the input) and the alternating current $I = I (t)$ (as the output) are given:

$$V = |V| \exp (j\omega t) \qquad \cdots\cdots (21)$$

$$I = |I| \exp (j (\omega t - \theta)) \qquad \cdots\cdots (22)$$

where j is the imaginary unit, and t is the time. Equations (21), (22) mean that, by applying an alternating voltage with an angular frequency ω and an amplitude $|V|$, we obtain an alternating current with an amplitude $|I|$ and a phase θ at the same angular frequency ω. Then, the complex impedance Z is obtained:

$$Z = V / I = |Z| \exp (j\theta) \qquad \cdots\cdots (23)$$

Note that in the electrical impedance measurement, the modulus $|Z|$ ($= |V|/|I|$) and phase θ of the complex impedance Z are obtained. The complex impedance Z for the overall equivalent circuit, as shown in Fig. 3, can be obtained by Eq. (24) if the number of rolling elements per rolling bearing is n:

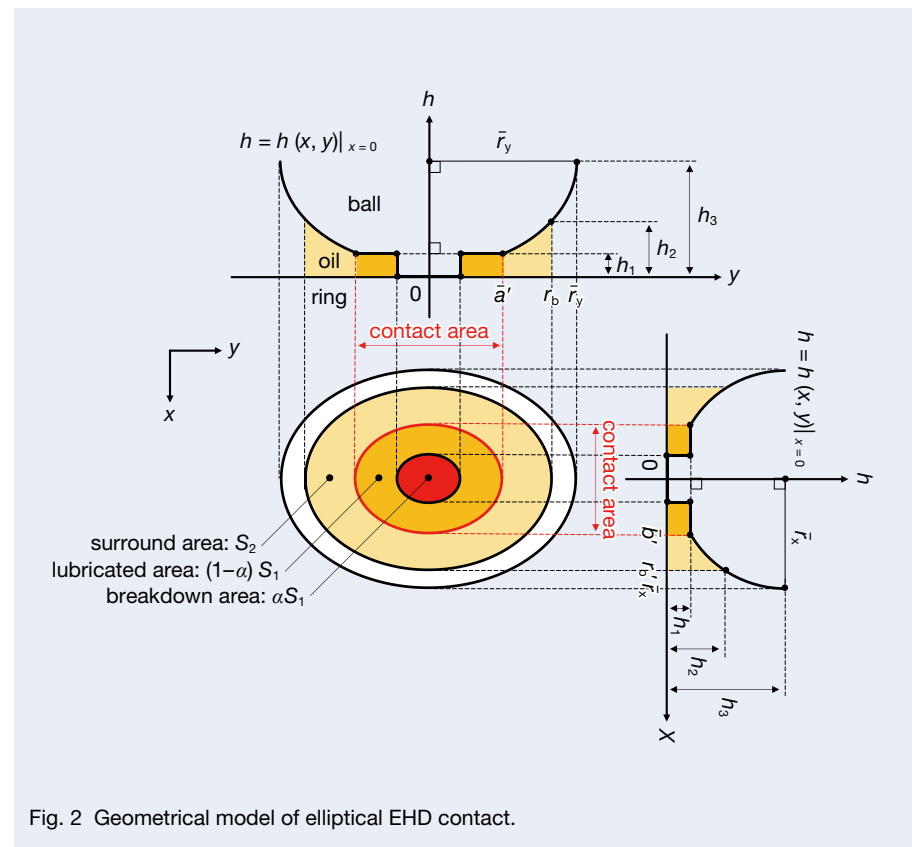$$1 / Z = n (1 / R_1 + j\omega (C_1 + C_2)) / 2 \qquad \cdots\cdots (24)$$
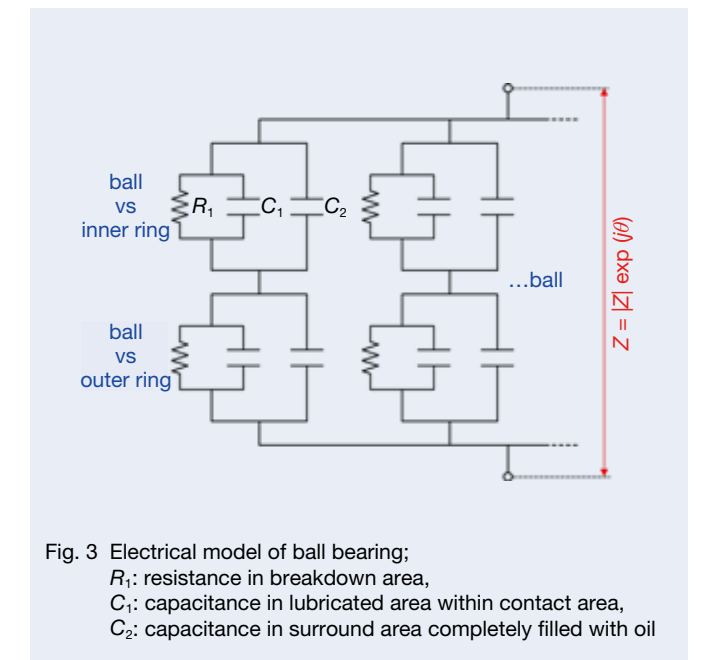

Fig. 2 Geometrical model of elliptical EHD contact.

Fig. 3 Electrical model of ball bearing;
R_1: resistance in breakdown area,
C_1: capacitance in lubricated area within contact area,
C_2: capacitance in surround area completely filled with oil

Normally, multiple bearings are used for the rotating shaft of the machine. Therefore, to make Eq. (24) versatile, we consider the number of rolling bearings, the measurement target, to be k. If k bearings are the measurement targets, all bearings are connected in parallel circuits; thus Eq. (24) would be expressed with Eq. (25):

$$1 / Z = kn \ (1 / R_1 + j\omega \ (C_1 + C_2)) / l \qquad \cdots\cdots (25)$$

where, l is the number of contacts per rolling element. For example, as in a ball-on-disc-type apparatus, if there is one contact per rolling element, $l = 1$ (i.e., one contact area between ball and disc). On the other hand, in the case of a rolling bearing, $l = 2$ (i.e., two contact areas between rolling element and inner/outer rings). In this study, to derive general equations for the electrical impedance method that can also work for a ball-on-disc-type apparatus [29], we will use Eq. (25) hereafter. Of course, when multiple bearings are the measurement target, we obtain the mean value for all contact areas of all bearings. From Eqs. (23), (25), Eqs. (26), (27) are given:

$$R_1 = kn \ | Z | / l\cos\theta \qquad \cdots\cdots (26)$$

$$C_1 + C_2 = - l\sin\theta / kn\omega \ | Z | \qquad \cdots\cdots (27)$$

Therefore, from Eqs. (15), (26), the breakdown ratio of oil films α can be obtained as follows:

$$\alpha = lR_{10} \cos\theta / kn \ | Z | \qquad \cdots\cdots (28)$$

Meanwhile, from Eqs. (16), (19), Eq. (27) are expressed with Eq. (29):

$$(\delta / h_1) \exp (\delta / h_1) = (\delta / \psi \overline{r}_h) \exp (\psi - \zeta\sin\theta \ | Z |) \qquad \cdots\cdots (29)$$

where δ and ζ are constants defined as follows:

$$\delta = (1 - \alpha) \ \overline{a} \ \overline{b} \ \overline{r}_h / 2 \ \overline{r}_x \overline{r}_y \qquad \cdots\cdots (30)$$

$$\zeta = l \ \overline{r}_h / 2\pi kn\varepsilon\omega \ \overline{r}_x \overline{r}_y \qquad \cdots\cdots (31)$$

Based on Eq. (29), we introduced the Lambert W function [38, 39] in order to derive the explicit function for h_1. For the arbitrary complex number z', the Lambert W function $\mathfrak{W} \ (z')$ is defined by Eq. (32):

$$\mathfrak{W} \ (z') \exp (\mathfrak{W} \ (z')) = z' \qquad \cdots\cdots (32)$$

Therefore, the following equation is obtained as the explicit function for h_1 from Eqs. (29), (32):

$$h_1 = \delta / \mathfrak{W} \ ((\delta / \psi \overline{r}_h) \exp (\psi - \zeta\sin\theta / \ | Z |) \qquad \cdots\cdots (33)$$

When oil films partially collapse in EHD contacts (i.e., the mixed lubrication), the mean oil film thickness $\overline{h}$ can be obtained from Eq. (34) using α and h_1:

$$\overline{h} = (1 - \alpha) \ h_1 \qquad \cdots\cdots (34)$$

As such, it was showed that the oil film thickness and breakdown ratio in EHD elliptical contacts of deep groove ball bearings can be obtained from Eqs. (28), (34), respectively. As these equations can also be applied to point contacts, such as a ball-on-disc-type apparatus [29], they are general equations for the electrical impedance method.

3. Experimental details

3.1 Apparatus

In this study, we verified the measurement accuracy of the developed method using a ball bearing test rig shown in Fig. 4. The measurement targets of this study were two test bearings, and we applied only the axial load F_a using a spring. To apply the electrical impedance method to this test rig, we applied a sinusoidal voltage from the LCR meter between rotating shaft and bearing housing. The rotating shaft was rotated while being insulated from the motor using a rubber timing belt. This test rig is able to simultaneously measure the outer ring temperature T and the bearing torque M in addition to the mean oil film thickness $\overline{h}$ and the breakdown ratio α when the rotational speed of the inner ring N is varied. The outer ring temperature was measured by directly attaching a thermocouple to the outer ring of the test bearing. The bearing torque was measured by a load cell pulling a string attached to a freely rotating bearing housing.

3.2 Materials

The test bearings were deep groove ball bearings 608 (inner diameter: 8 mm, outer diameter: 22 mm, width: 7 mm) made of 52 100 steel (Young's modulus: 207 GPa, Poisson's ratio: 0.30). The cage and seal were made of resin and metal, respectively. The tested oil was PAO (poly-α-olefin oil, viscosity at 40°C: $v = 19 \ mm^2/s$). The relative permittivity of oil was constant ($\varepsilon_{oil} \approx 2.0$) in a frequency range of $f = 30$ Hz to 1.0 MHz for a sinusoidal voltage (RMS amplitude: $V_e = 1$ V); therefore, we calculated the oil film thickness with $\varepsilon = \varepsilon_{oil} \ \varepsilon_0 = 2.0 \ \varepsilon_0$ F/m, where $\varepsilon_0 = 8.85 \cdot 10^{-12}$ F/m is the dielectric constant in a vacuum.

3.3 Procedure

Bearing tests were all conducted at an ambient temperature (26°C). Before performing experiments, test bearings were cleaned thoroughly in petroleum benzine with an ultrasonic cleaner. After the lubricating oil 40 mg was injected into the each bearing, the metal seals were attached. Two test bearings were installed to the rotating shaft, and applied a sinusoidal voltage (RMS amplitude: $V_e = 1.5$ V, frequency: $f = 1.0$ MHz) between shaft and housing while only applying the axial load shown in Fig. 4. First, the initial complex impedance Z_0 was measured under stationary contacts (i.e., $\alpha = 1$). From the measured Z_0, we obtained the electrical resistance R_{10} in Eq. (28) using the following Eq. (35).

$$R_{10} = kn \ | Z_0 | / l\cos\theta_0 \qquad \cdots\cdots (35)$$

where $| Z_0 |$ and θ_0 are the modulus and phase of Z_0, respectively. By substituting Eq. (35) into Eq. (28), it can be seen that α is not affected by k, l, and n. Besides, we rotated the inner rings of two test bearings, and simultaneously measured four parameters $| Z |$, θ, T, and M under dynamic contacts (sampling rate: 1 Hz). In this study, we increased the rotational speed N from 50 min^{-1} every 40 min up to 6 000 min^{-1} (the total test time: 10 h). Note that all experimental results are the mean values for two test bearings. The mean oil film thickness obtained by the electrical impedance method was compared to the theoretical value calculated by Hamrock–Dowson equation [37]. Note that the theoretical value was the mean value of the central oil film thickness generated in the inner and outer rings.

4. Results

4.1 Examples of $| Z |$ and θ

Figure 5 shows examples of the obtained electrical measurements for two ball bearings, which are the measured values of the modulus $| Z |$ (upper) and phase θ (lower) of the complex impedance Z at a varied rotational speed N under the axial load $F_a = 30$ N. Each plot shows the measured value after 40 min at each rotational speed N. Under the experimental conditions, $| Z |$ varied approximately from 0.1 to 1.5 kΩ and θ varied approximately from –10° to –90°. In the following section, the mean oil film thickness $\overline{h}$ and the breakdown ratio α will be quantified by using $| Z |$ and θ.
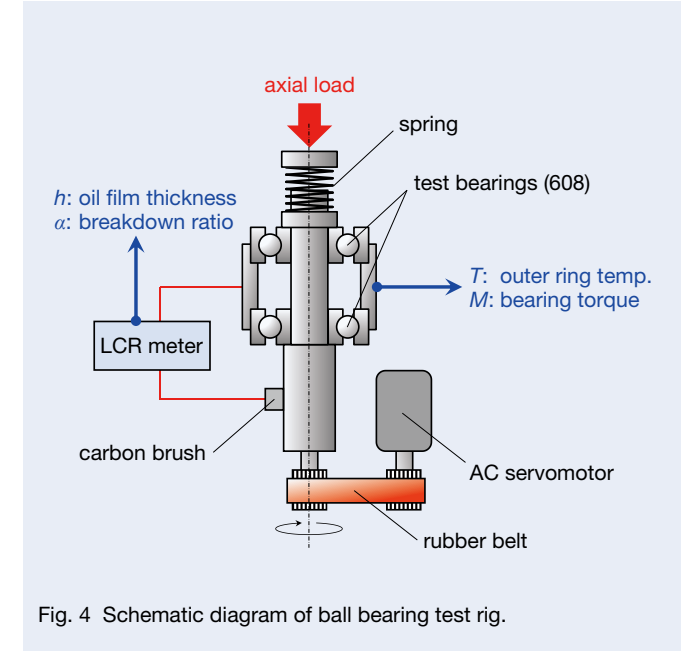

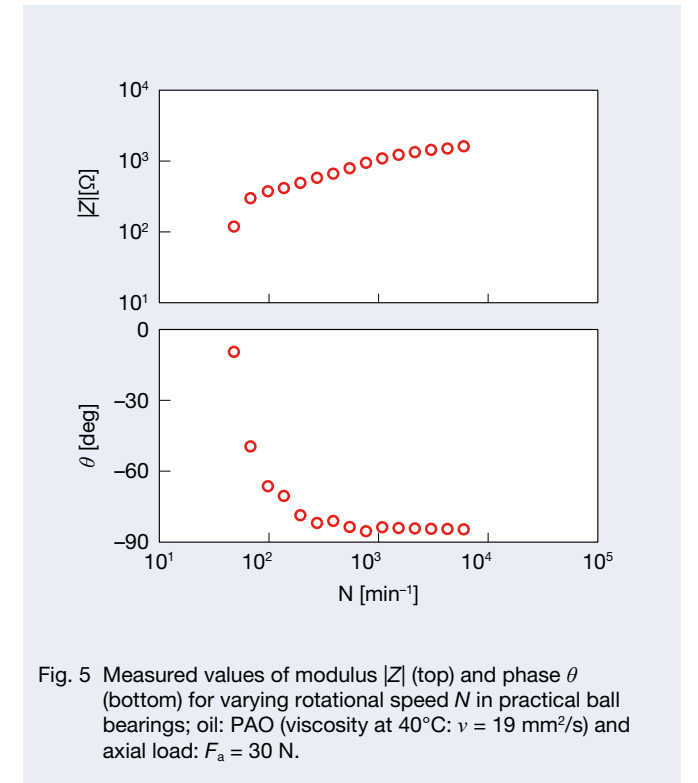Fig. 4 Schematic diagram of ball bearing test rig.

Fig. 5 Measured values of modulus $|Z|$ (top) and phase θ (bottom) for varying rotational speed N in practical ball bearings; oil: PAO (viscosity at 40°C: $v = 19 \ mm^2/s$) and axial load: $F_a = 30$ N.

4.2 Measurements of h, α, T, and M

The mean oil film thickness $\bar{h}$, the breakdown ratio α, the outer ring temperature T, and the bearing torque M were measured simultaneously while the rotational speed N was varied from 50 to 6 000 min^{-1}, as shown in Fig. 6 (i.e., the same experimental conditions as Fig. 5). Each plot shows the measured values after 40 min at each rotational speed N. Besides, each plot is also the mean values of four tests performed under the same conditions. The ranges of errors in Fig. 6 represent the standard deviation, and the red open circles are measured values obtained by the electrical impedance method developed in this study. The black dashed line in the top left graph represents the theoretical oil film thickness at an ambient temperature. The black dashed line in the bottom left graph indicates an ambient temperature. Figure 6 shows that $\bar{h}$ obtained by the developed method was consistent with the theoretical value in the low-speed range. Furthermore, as α and M increased together in the low-speed range, this

indicated that the developed method is able to evaluate α quantitatively. On the other hand, $\bar{h}$ was thinner than the theoretical value in the high-speed range, confirming that T was increasing. We also confirmed that M decreased in this high-speed range.

Figure 7 shows the temporal changes for 40 min in the low-speed range (N = 100 min^{-1}). It was confirmed that $\bar{h}$ was similar to the theoretical value although it became occasionally thin (several nm). On the other hand, α and M behaved very similarly, which means that the larger the metallic contact, the higher the bearing torque.

Figure 8 shows the temporal changes occurring in the high-speed range (N = 6 000 min^{-1}). It was found that the experiment was performed under the hydrodynamic lubrication since $\alpha \approx 0$. The results of $\bar{h}$ and M indicated that the increased oil film increased the bearing torque. It was considered that the bearing torque increased when the race track was replenished with the lubricating oil [40–42]. Besides, Fig. 8 confirmed that T increased with time.
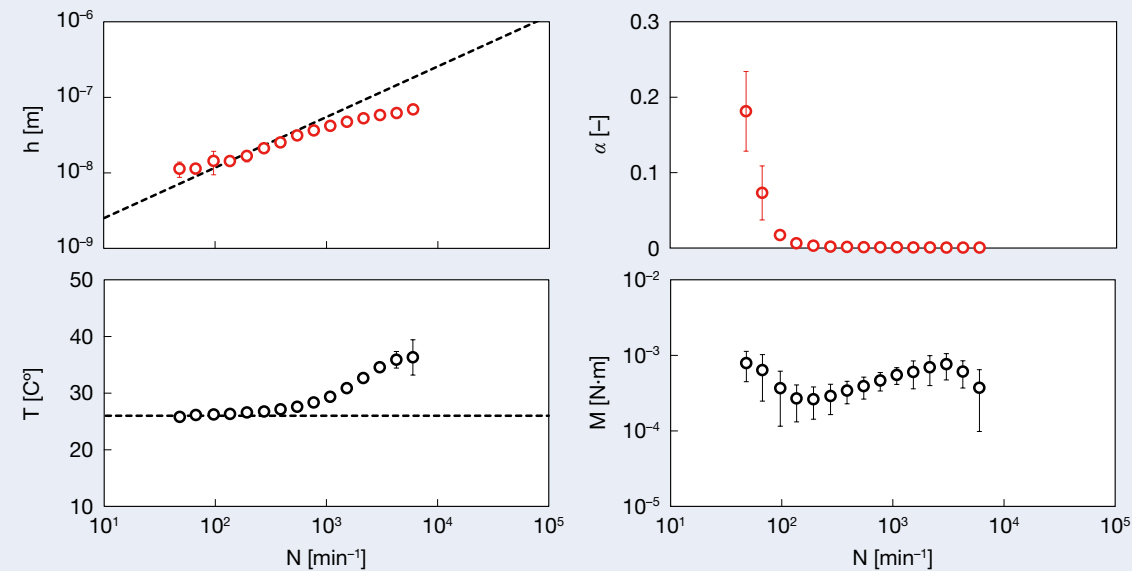

Fig. 6 Measured values of oil film thickness h (left top), breakdown ratio α (right top), outer ring temperature T (left bottom), and bearing torque M (right bottom) for varying rotational speed N; oil: PAO (viscosity at 40°C: ν = 19 mm^2/s) and axial load: F_a = 30 N; red open circles in graphs: measured values by electrical method; black dashed line in left top graph: theoretical prediction at room temperature (26°C) by Hamrock and Dowson; black dashed line in left bottom graph: T = 26°C.

Fig. 7 Time evolutions of measured oil film thickness h (left top), breakdown ratio α (right top), outer ring temperature T (left bottom), and bearing torque M (right bottom); oil: PAO (viscosity at 40°C: ν= 19 mm^2/s), rotational speed: N = 100 min^{-1}, and axial load: F_a = 30 N; red lines in graphs: measured values by electrical method; black dashed line in left top graph: theoretical prediction at room temperature (26°C) by Hamrock and Dowson.
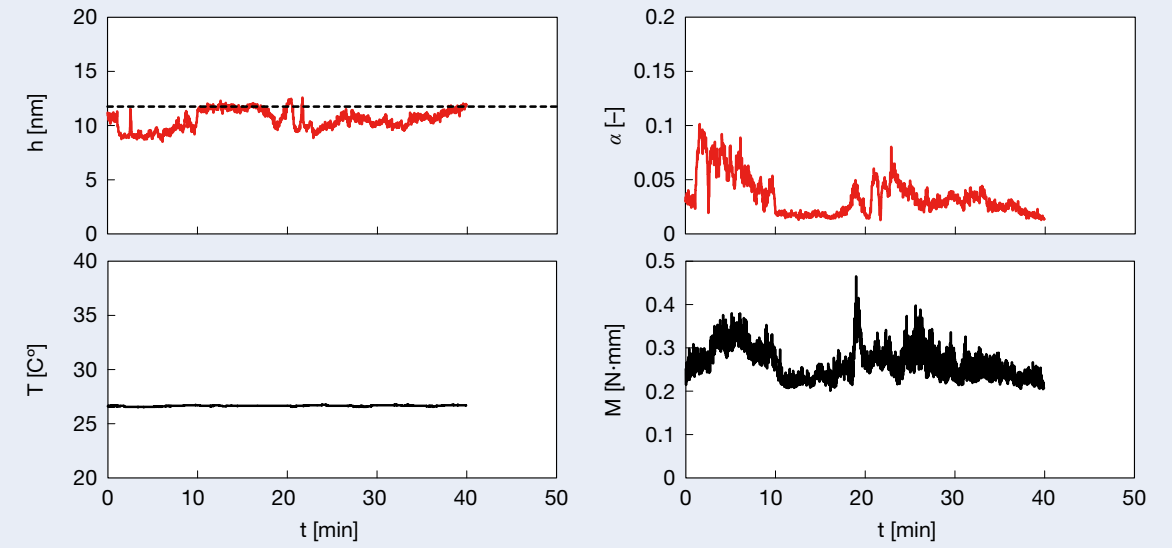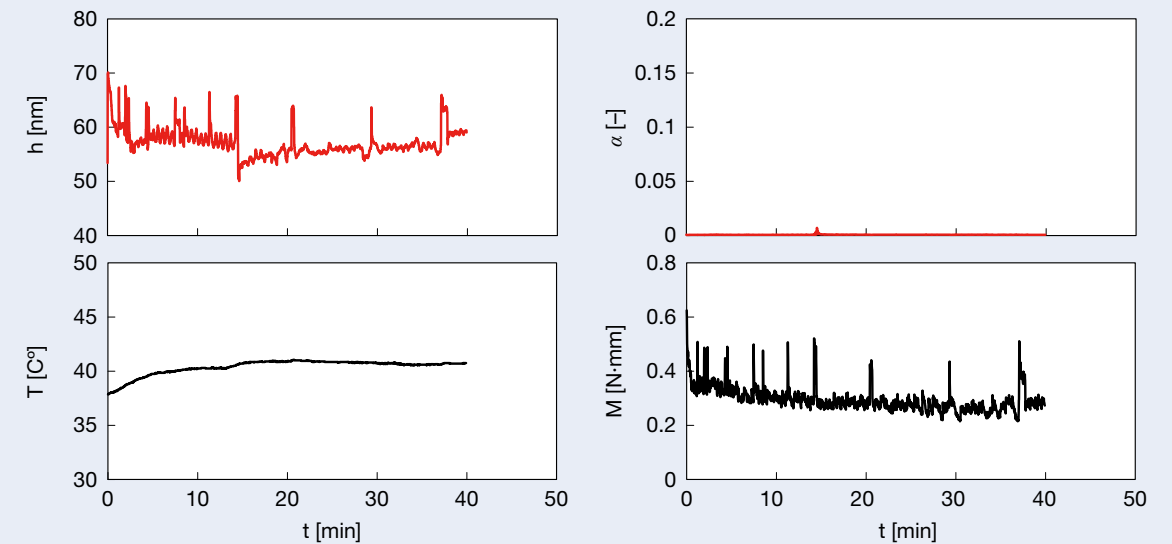

Fig. 8 Time evolutions of measured oil film thickness h (left top), breakdown ratio α (right top), outer ring temperature T (left bottom), and bearing torque M (right bottom); oil: PAO (viscosity at 40°C: ν= 19 mm^2/s), rotational speed: N = 6 000 min^{-1}, and axial load: F_a = 30 N; red lines in graphs: measured values by electrical method.

4.3 Observations of inner ring

Figure 9 shows the observations of the inner ring using an optical microscope. Figure 9 (b) indicates that the wear occurred during the experiment shown in Fig. 6. Next, the surface roughness of the wear track was measured using an interference microscope. The y-axis (horizontal axis) in Fig. 10 is perpendicular to the direction of the inner ring rotation. Figure 10 (b) shows that the surface roughness after experiments increased due to wear.
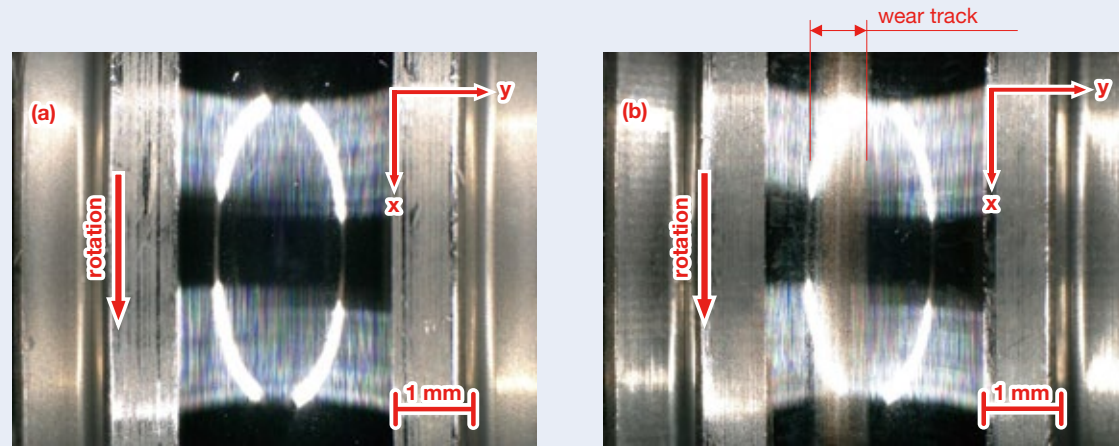

Fig. 9 Photographs of inner rings for v = 19 mm²/s, N = 50 to 6 000 min⁻¹, and F_a = 30 N; (a) photograph of inner ring before experiments and (b) photograph of inner ring after experiments; red arrow: rotation direction of inner ring.
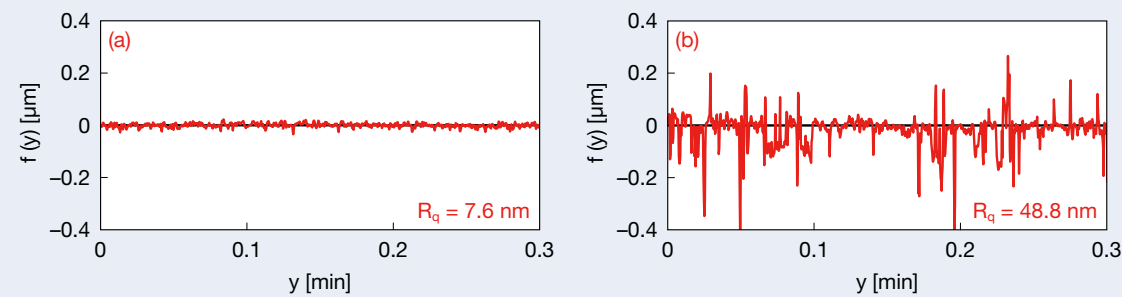

Fig. 10 Surface roughness profiles of inner rings for v = 19 mm²/s, N = 50 to 6 000 min⁻¹, and F_a = 30 N; y-axis: coordinate across rotation direction of inner ring, f (y): height of surface roughness, R_q: root mean square roughness; (a) measured profile before experiments and (b) measured profile after experiments.

5. Discussion

5.1 Validation of measured h-values

Figure 6 shows that $\bar{h}$ obtained by the developed method agrees with the theoretical oil film thickness in the low-speed range. On the other hand, $\bar{h}$ was thinner than the theoretical value in the high-speed range, and at this time, T increased; therefore, it was considered that the viscous shear heating [43-45] occurred, which caused the decrease of viscosity. For reference, Fig. 11 shows the theoretical oil film thickness when assuming that the EHD inlet temperature is equal to T. It shows that the measured values (red solid circles) are still thinner than the theoretical values (red dashed circles) that took T into consideration. In short, it indicates the EHD inlet temperature is higher than T. Besides, in this high-speed range, Fig. 8 confirmed that $\bar{h}$ and M decreased or increased simultaneously, which means that the starvation and replenishment have repeatedly occurred in EHD contacts. That is, in the high-speed range, it was found that not only the viscous shear heating but the starved lubrication also occurred, resulting in the oil film thickness obtained by developed method being thinner than the theoretical values. Furthermore, it is suggested that the reason M decreases in the high-speed range, shown in Fig. 6, is also the same.

Incidentally, the developed method is characterized by taking the capacitance C_2 in the surround EHD contact into consideration, as shown in Fig. 3. Therefore, it was considered the influence of C_2 on the measurement accuracy of the oil film thickness. The mean oil film thickness $\bar{h}$ not considering C_2 is obtained by the following equation where $C_2 = 0$ F is substituted into Eq. (27).

$$\bar{h} = -\pi (1 - \alpha)^2 \, \bar{a}\, \bar{b}\, kn\varepsilon\omega \mid Z \mid / \, l \sin\theta \qquad \cdots\cdots (36)$$

Figure 12 shows the influence of C_2 on the measurement accuracy under the hydrodynamic lubrication (i.e., $\alpha = 0$). Here, h is the theoretical values considering C_2, h' is the theoretical values not considering C_2, the red solid line is the case of a deep groove ball bearing 608 used in this study (i.e., elliptical contacts), and the red dashed line is the case of a ball-on-disc-type apparatus used in the previous study [29] (i.e., a point contact). It is indicated that the oil film thickness was underestimated when C_2 was not considered. Besides, when comparing the ball bearing with the ball-on-disc-type apparatus, the influence of C_2 on the oil film measurement was different. In short, it depends on the shapes of the contact area and its surrounding. However, in both cases, the thinner h, the smaller the impact of C_2. Therefore, from Eqs. (16), (19), we calculated C_1 and C_2 respectively when the oil film thickness varied. Figure 13 shows that the magnitudes of C_1 and C_2 reversed at $h \approx 400$ nm for the test bearing, and $h \approx 50$ nm for the ball-on-disc-type apparatus. In both cases, it is confirmed that C_2/C_1 becomes smaller as the oil film becomes thinner.
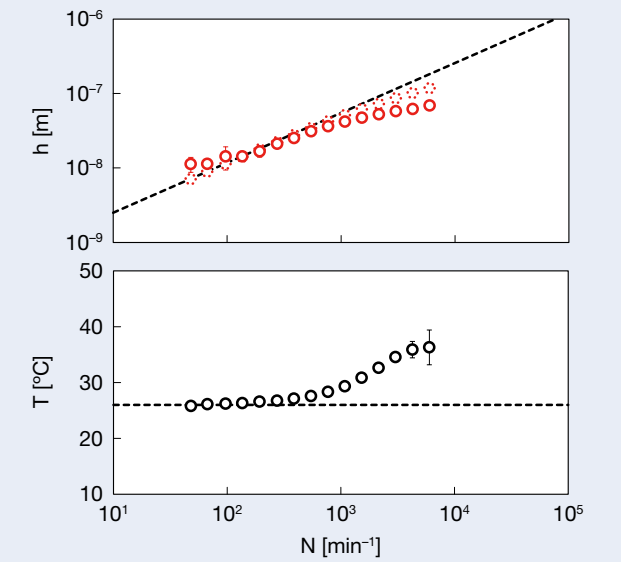
Fig. 11 Theoretical predictions of oil film thickness considering outer ring temperature T; oil: PAO (viscosity at 40°C: v = 19 mm²/s) and axial load: F_a = 30 N; red open circles in top graph: measured values by electrical method; red dashed circles in top graph: theoretical prediction at outer ring temperature T by Hamrock and Dowson; black dashed line in top graph: theoretical prediction at room temperature (26°C) by Hamrock and Dowson; black dashed line in bottom graph: T = 26°C.

Fig. 12 Effect of C_2 on measurement accuracy of h with no breakdown area (i.e., $\alpha = 0$); h: theoretical values considering C_2, h': theoretical values not considering C_2, red line: simulated results of practical ball bearing, red dashed line: simulated results of ball-on-disc-type apparatus.

This is the reason why the influence of C_2 on the oil film measurement becomes smaller, as shown in Fig. 12.

By the way, shown in Fig. 8, it was suggested that the starved lubrication occurred in the high-speed range. This means that surround EHD contacts are not suff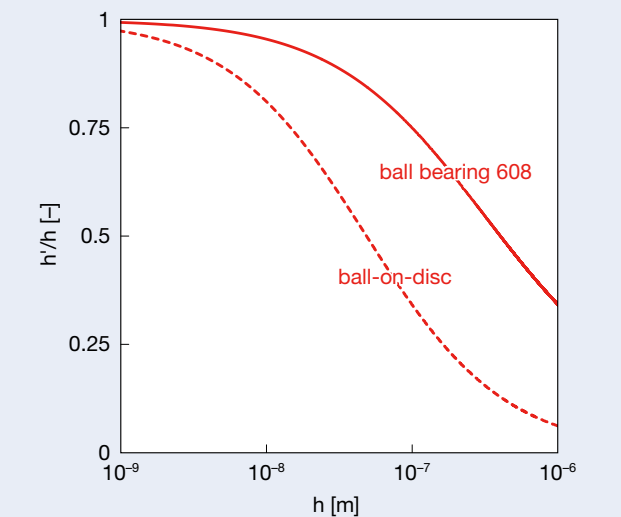iciently filled with the lubricating oil, which may affect C_2. However, according to Fig. 13, it is considered that C_2 does not significantly affect the measurement accuracy because the oil film generally becomes thin under the starved lubrication. As for the influence of the starved lubrication (or the cavitation) on the measurement accuracy of the oil film thickness, the previous study has already discussed in detail [29].

5.2 Validation of measured α-values

In order to confirm the validity of α obtained by the developed method, the relationship between film parameter Λ and breakdown ratio α was examined. Here, Λ is the ratio of the oil film thickness to the surface roughness [3], which is obtained by the following equation:

$$\Lambda = \bar{h} / \sqrt{R_{q1}^2 + R_{q2}^2} \qquad \cdots\cdots (37)$$

where R_{q1} and R_{q2} are the root mean square surface roughness of the rolling element and inner ring raceway, respectively (R_{q1} = 4.0 nm, and R_{q2} = 7.6 nm). Figure 14 shows the relationship between Λ and α, and the range of error in the figure is the standard deviation from four rounds of experiments. From this graph, it is found that α increases at Λ < 3, which means that the mixed lubrication has occurred. Johnson et al. [46] expected that the number of asperity contacts within the EHD contact was given by a Poisson distribution, and indicated that the oil film breaks at Λ < 3 in theory. Therefore, Fig. 14 confirmed that the developed method evaluates not only $\bar{h}$ but also α quantitatively.

Moreover, Fig. 7 confirmed that α and M behaved similarly in the low-speed range. Specifically, the bearing torque increases as the metallic contact area increases. Bowden et al. [47, 48] also pointed out that the friction force increased as the real contact area increased, supporting the results shown in Fig. 7. Besides, Figs. 9 (b), 10 (b) confirmed that the surface roughness increased after the experiment due to wear. These observations also support that α actually increased in the low-speed range (i.e., the mixed lubrication occurred).
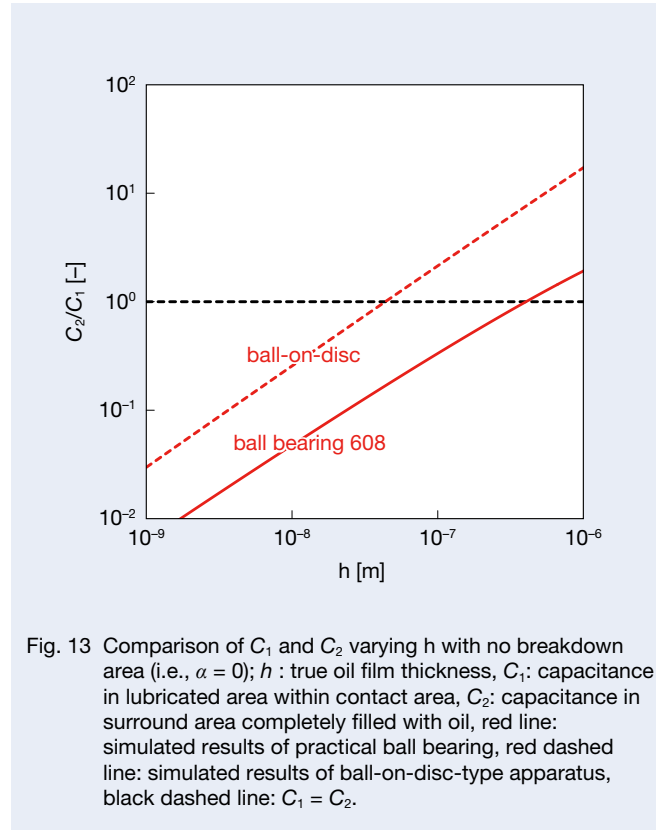

Fig. 13 Comparison of C_1 and C_2 varying h with no breakdown area (i.e., α = 0); h : true oil film thickness, C_1: capacitance in lubricated area within contact area, C_2: capacitance in surround area completely filled with oil, red line: simulated results of practical ball bearing, red dashed line: simulated results of ball-on-disc-type apparatus, black dashed line: $C_1 = C_2$.
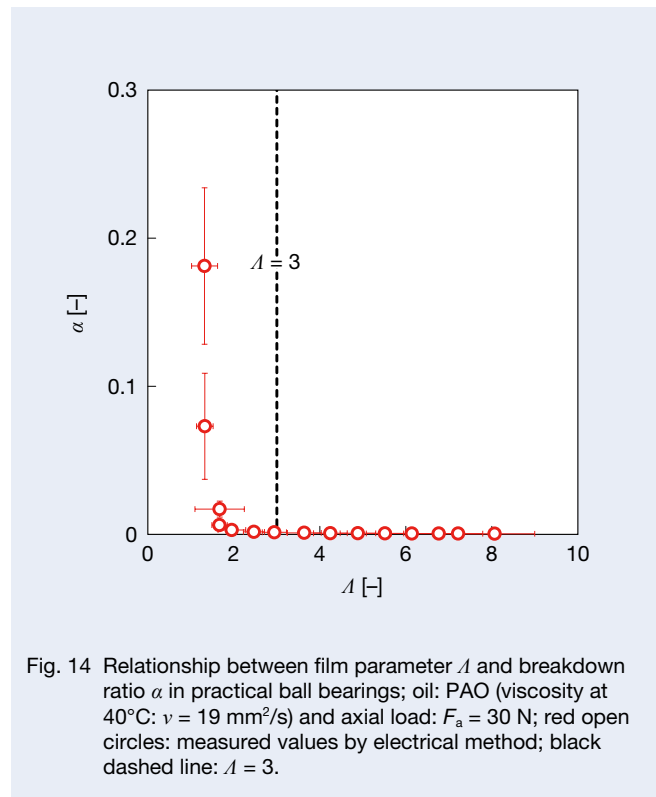

Fig. 14 Relationship between film parameter Λ and breakdown ratio α in practical ball bearings; oil: PAO (viscosity at 40°C: ν = 19 mm²/s) and axial load: F_a = 30 N; red open circles: measured values by electrical method; black dashed line: Λ = 3.

6. Conclusions

In this study, we developed the electrical impedance method that could be applied to elliptical EHD contacts. Furthermore, we applied the developed method to monitor the lubrication condition of practical deep groove ball bearings, and verified the measurement accuracy. Specifically, we simultaneously measured the outer ring temperature and bearing torque in addition to the oil film thickness and the breakdown ratio obtained by the developed method, and compared these results to verify the measurement accuracy of the developed method. Our findings are as follows:

1. It was shown that the thickness and breakdown ratio of oil films could be theoretically derived from the complex impedance generated when a sinusoidal voltage was applied to elliptical contacts of practical ball bearings. The equations derived in this study can be applied to not only elliptical contacts but also a point contact; thus, they can be considered general equations for the electrical impedance method.
2. The results of varying the rotational speed confirmed that the mean oil film thickness by the developed method agrees with the central oil film thickness by Hamrock–Dowson equation in the low-speed range.
3. On the other hand, the measured oil film thickness was thinner than the theoretical value in the high-speed range. From the fact that the outer ring temperature increased in this range, it is considered that the viscous shear heating occurred, which caused the decrease of viscosity. Besides, the finding that the oil film thickness and bearing torque were linked indicated that the starved lubrication also occurred. Both results support that measured values are thinner than theoretical values in the high-speed range.
4. The electrical impedance method developed in this study is characterized by taking the capacitance C_2 in the surround EHD contact into consideration. It was confirmed that the influence of C_2 on the measurement accuracy of the oil film thickness differs based on the shapes of the contact area and its surrounding. In addition, it was also found that the thinner the oil film, the smaller the influence of C_2 on the measurement accuracy.
5. The developed method confirmed that the mixed lubrication occurs at Λ < 3, where both the breakdown ratio and bearing torque have increased simultaneously. It means that this method can also evaluate the breakdown ratio of practical bearings quantitatively.

The electrical impedance method developed in this study is able to simultaneously monitor the oil film thickness and breakdown ratio in elliptical EHD contacts; thus, it is hoped that this method will contribute to a better understanding of lubrication conditions in practical ball bearings. Furthermore, since this method can be applied to a ball-on-disc-type apparatus, it could also contribute to basic studies of steel/steel point contacts.

Nomenclature

a_1 semimajor axis of contact ellipse between rolling element and inner ring   [m]

a_2 semimajor axis of contact ellipse between rolling element and outer ring   [m]

$\bar{a}$ mean semimajor axis of contact ellipse expressed as $\bar{a} = (a_1 + a_2)\,/\,2$ [m]

$\bar{a}'$ estimated mean semimajor axis of contact ellipse expressed as $\bar{a}' = \sqrt{\bar{a}\,\bar{b}\,\bar{r}_y\,/\,\bar{r}_x}$ [m]

b_1 semiminor axis of contact ellipse between rolling element and inner ring   [m]

b_2 semiminor axis of contact ellipse between rolling element and outer ring   [m]

$\bar{b}$ mean semiminor axis of contact ellipse expressed as $\bar{b} = (b_1 + b_2)\,/\,2$ [m]

$\bar{b}'$ estimated mean semiminor axis of contact ellipse expressed as $\bar{b}' = \sqrt{\bar{a}\,\bar{b}\,\bar{r}_x\,/\,\bar{r}_y}$ [m]

f frequency of sinusoidal voltage   [Hz]

$f(y)$ height of surface roughness in y-axis direction   [m]

h oil film thickness   [m]

h_1 oil film thickness in lubricated area   [m]

h_2 maximum oil film thickness in surround area   [m]

h_3 coordinate of ellipsoid center from x-y plane   [m]

$\bar{h}$ mean oil film thickness expressed as $\bar{h} = (1 - \alpha)\,h_1$ [m]

h' oil film thickness not considering C_2 [m]

j imaginary unit   [–]

k number of bearings   [–]

l number of contact areas per rolling element   [–]

n number of rolling elements per bearing   [–]

r_b radius of rolling element   [m]

r_b' estimated radius of rolling element in rolling direction expressed as $r_b' = r_b\bar{r}_x\,/\,\bar{r}_y$ [m]

$\bar{r}_h$ semi-axis of ellipsoid in h-axis direction expressed as $\bar{r}_h = (\bar{r}_x + \bar{r}_y)\,/\,2$ [m]

r_{x1} effective radius in rolling direction between rolling element and inner ring   [m]

r_{x2} effective radius in rolling direction between rolling element and outer ring   [m]

$\bar{r}_x$ semi-axis of ellipsoid in rolling direction expressed as $\bar{r}_x = (r_{x1} + r_{x2})\,/\,2$ [m]

r_{y1} effective radius perpendicular to rolling direction between rolling element and inner ring   [m]

r_{y2} effective radius perpendicular to rolling direction between rolling element and outer ring   [m]

$\bar{r}_y$ semi-axis of ellipsoid perpendicular to rolling direction expressed as $\bar{r}_y = (r_{y1} + r_{y2})\,/\,2$ [m]

t time   [s]

x coordinate in rolling direction   [m]

y coordinate perpendicular to rolling direction   [m]

z' complex number   [–]

C_1 capacitance in lubricated area within contact area   [F]

C_2 capacitance in surround area completely filled with oil   [F]

F_a axial load   [N]

I alternating current (AC) expressed as $I = |I|\exp(j\,(\omega t - \theta))$ [A]

$|I|$ amplitude of alternating current   [A]

M bearing torque   [N·m]

N rotational speed   [min^{-1}]

R_1 resistance in breakdown area under dynamic contact conditions   [Ω]

R_{10} resistance of breakdown area under stationary contact conditions   [Ω]

R_q root mean square roughness   [m]

R_{q1} root mean square roughness of rolling element   [m]

R_{q2} root mean square roughness of inner ring   [m]

S_1 Hertzian contact area   [m^2]

S_2 surround area of EHD contact   [m^2]

T outer ring temperature of bearing   [°C]

V sinusoidal voltage expressed as $V = |V|\exp(j\omega t)$ [V]

$|V|$ amplitude of sinusoidal voltage   [V]

V_e RMS amplitude of sinusoidal voltage expressed as $V_e = |V|\,/\,\sqrt{2}$ [V]

Z complex impedance expressed as $Z = V\,/\,I = |Z|\exp(j\theta)$ [Ω]

$|Z|$ modulus of complex impedance under dynamic contact conditions   [Ω]

$|Z_0|$ modulus of complex impedance under stationary contact conditions   [Ω]

α breakdown ratio of oil films   [–]

δ constant expressed as $\delta = (1 - \alpha)\,\bar{a}\,\bar{b}\,\bar{r}_h\,/\,2\bar{r}_x\bar{r}_y$ [m]

ε complex constant of oil   [F/m]

ε_0 dielectric constant of vacuum   [F/m]

ε_{oil} relative permittivity of oil   [–]

ζ constant expressed as $\zeta = l\,\bar{r}_h\,/\,2\pi k n \varepsilon \omega \bar{r}_x \bar{r}_y$ [Ω]

θ phase of complex impedance under dynamic contact conditions   [deg]

θ_0 phase of complex impedance under stationary contact conditions   [deg]

v kinematic viscosity of oil   [mm^2/s]

ψ dimensionless constant expressed as $\psi = 1 - \sqrt{1 - (r_b\,/\,\bar{r}_v)^2}$ [–]

ω angular frequency of sinusoidal voltage expressed as $2\pi f$ [rad/s]

Λ film parameter expressed as $\Lambda = \bar{h}\,/\,\sqrt{R_{q1}^2 + R_{q2}^2}$ [–]

References

[1] Jianjun, Y., Jonathan, O., Cheryl, P. and Ronald, S., "Big Jump of Record Warm Global Mean Surface Temperature in 2014–2016 Related to Unusually Large Oceanic Heat Releases," Geophysical Research Letters, 45, 2, 2018, 1069–1078.

[2] Gohar, R. and Cameron, A., "The Mapping of Elastohydrodynamic Contacts," ASLE Transactions, 10, 1967, 215–225.

[3] Tallian, T. E., "On Competing Failure Modes in Rolling Contact," ASLE transactions, 10, 4, 1967, 418–439.

[4] Zhu, D., Martini, A., Wang, W., Hu, Y., Lisowsky, B. and Wang, Q. J., "Simulation of Sliding Wear in Mixed Lubrication," ASME Journal of Tribology, 129, 3, 2007, 544–552.

[5] Maruyama, T., Saitoh, T. and Yokouchi, A., "Differences in Mechanisms for Fretting Wear Reduction between Oil and Grease Lubrication," Tribology Transactions, 60, 2017, 497–505.

[6] Albahrani, S. M. B., Philippon, D., Vergne, P. and Bluet, J. M., "A Review of In Situ Methodologies for Studying Elastohydrodynamic Lubrication," Proceedings of the Institution of Mechanical Engineers, Part J: Journal of Engineering tribology, 230, 2016, 86–110.

[7] Johnston, G. J., Wayte, R. and Spikes, H. A., "The Measurement and Study of Very Thin Lubricant Films in Concentrated Contacts," Tribology Transactions, 34, 1991, 187–194.

[8] Kaneta, M., Sakai, T. and Nishikawa, H., "Effects of Surface Roughness on Point Contact EHL," Tribology Transactions, 36, 4, 1993, 605–612.

[9] Sugimura, J., Jones, W. R. and Spikes, H. A., "EHD Film Thickness in Non-steady State Contacts," ASME Journal of Tribology, 120, 1998, 442–452.

[10] Kaneta, M., Ozaki, S., Nishikawa, H. and Guo, F., "Effects of Impact Loads on Point Contact Elastohydrodynamic Lubrication Films," Proceedings of the Institution of Mechanical Engineers, Part J: Journal of Engineering tribology, 221, 2007, 271–278.

[11] Maruyama, T. and Saitoh, T., "Oil Film Behavior under Minute Vibrating Conditions in EHL Point Contacts," Tribology International, 43, 2010, 1279–1286.

[12] Kaneta, M., Nishikawa, H., Kanada, T. and Matsuda, K., "Abnormal Phenomena Appearing in EHL Contacts," ASME Journal of Tribology, 118, 1996, 886–892.

[13] Yagi, K. and Vergne, P., "Abnormal Film Shapes in Sliding Elastohydrodynamic Contacts Lubricated by Fatty Alcohols," Proceedings of the Institution of Mechanical Engineers, Part J: Journal of Engineering tribology, 221, 2007, 287–300.

[14] Nakano, K. and Spikes, H. A., "Process of Boundary Film Formation from Fatty Acid Solution," Tribology Online, 7, 2012, 1–7.

[15] Furey, M. J., "Metallic Contact and Friction between Sliding Surfaces," ASLE Transactions, 4, 1961, 1–11.

[16] Tallian, T. E., Chiu, Y. P., Huttenlocher, D. F, Kamenshine, J. A., Sibley, L. B. and Sindlinger, N. E., "Lubricant Films in Rolling Contact of Rough Surfaces," ASLE Transactions, 7, 2, 1964, 109–126.

[17] Chu, P. S. Y. and Cameron, A., "Flow of Electric Current Through Lubricated Contacts," ASLE Transactions, 10, 1967, 226–234.

[18] Lugt, P. M., Severt, R. W. M, Fogelström, J. and Tripp, J. H., "Influence of Surface Topography on Friction, Film Breakdown and Running-in in the Mixed Lubrication Regime", Proceedings of the Institution of Mechanical Engineers, Part J: Journal of Engineering tribology, 215, 2001, 519–533.

[19] Lord, J. and Larsson, R., "Film-forming Capability in Rough Surface EHL Investigated Using Contact Resistance," Tribology International, 41, 9, 2008, 831–838.

[20] Clarke, A., Weeks, I. J. J., Evans, H. P. and Snidle, R. W., "An Investigation into the mixed lubrication Using Electrical Contact Resistance Techniques, Tribology International, 93, 2016, 709–716.

[21] Crook, A.W., "Elastohydrodynamic Lubrication of Rollers," Nature, 190, 1961, 1182–1183.

[22] Prashada, H., "Theoretical Evaluation of Impedance, Capacitance and Charge Accumulation on Roller Bearing Operated under Electrical Fields," Wear, 125, 1988, 223–239.

[23] Jablonka, K., Glovnea, R. and Bongaerts, J., "Evaluation of EHD Films by Electrical Capacitance," Journal of physics D: applied physics, 45, 38, 2012, 385301.

[24] Jablonka, K., Glovnea, R., Bongaerts, J. and Morales-Espejel, G., "The Effect of the Polarity of the Lubricant upon Capacitance Measurements of EHD Contacts," Tribology International, 61, 2013, 95–101.

[25] Nakano, K. and Akiyama, Y., "Simultaneous Measurement of Film Thickness and Coverage of Loaded Boundary Films with Complex Impedance Analysis," Tribology Letters, 22, 1, 2006 127–134.

[26] Manabe, K. and Nakano, k., "Breakdown of Oil Films and Formation of Residual Films," Tribology International, 41, 2008, 1103–1113.

[27] Schnabel, S., Marklund, P., Minami, I. and Larsson, R., "Monitoring of Running-in of an EHL Contact Using Contact Impedance," Tribology Letters, 63, 35, 2016, DOI:10.1007/s11249-016-0727-2.

[28] Nihira, T., Manabe, K., Tadokoro, C., Ozaki, S. and Nakano, K., "Complex Impedance Measurement Applied to Short-time Contact between Colliding Steel Surfaces," Tribology Letters, 57, 29, 2015, DOI: 10.1007/s11249-015-0478-5.

[29] Maruyama, T. and Nakano, K., "In Situ Quantification of Oil Film Formation and Breakdown in EHD Contacts," Tribology Transactions, 61, 6, 2018, 1057–1066.

[30] Otsu, T., Tanaka, H., Izumi, N. and Sugimura, J., "Effect of Surrounding Gas on Cavitation in EHL," Tribology Online, 4, 2, 2009, 50–54.

[31] Otsu, T., Tanaka, H. and Sugimura, J., "Initiation and Growth of Gaseous Cavity in Concentrated Contact in Various Surrounding Gases," Tribology International, 53, 2012, 68–75.

[32] Emden, E. V., Venner, C. H. and Morales-Esoejel, G. E., "Aspects of Flow and Cavitation Around an EHL Contact," Tribology International, 95, 2016, 435–448.

[33] Wedeven, L. D., Evans, D. and Cameron, A., "Optical Analysis of Ball Bearing Starvation," ASME Journal of lubrication technology, 93, 3, 1971, 349–361.

[34] Hamrock, B. J. and Dowson, D., "Isothermal Elastohydrodynamic Lubrication of Point Contacts: Part IV–Starvation Results," ASME Journal of lubrication technology, 99, 1977, 15–23.

[35] Cann, P. M., "The Transition between Fully Flooded and Starved Regimes in EHL," Tribology International, 37, 2004, 859–864.

[36] Maruyama, T. and Saitoh, T., "Relationship between Supplied Oil Flow Rates and Oil Film Thicknesses under Starved Elastohydrodynamic Lubrication," Lubricants, 3, 2, 2015, 365–380.

[37] Hamrock, B. J. and Dowson, D., "Isothermal Elastohydrodynamic Lubrication of Point Contacts: Part III–Fully Flooded Results," ASME Journal of lubrication technology, 99, 2, 1977, 264–275.

[38] Lambert, J. H., "Observationes Variae in Mathesin Puram," Acta Helvetica Physico-mathematico-anatomico-botanico-medica, 3, 1758, 128–168.

[39] Corless, R. M., Gonnet, G. H., Hare, D. E. G., Jeffrey, D. J. and Knuth, D. E., "On the Lambert W Function," Advances in Computational Mathematics, 5, 1996, 329–359.

[40] Jacod, B., Pubilier, F., Cann, P. M. E. and Lubrecht, A. A., "An Analysis of Track Replenishment Mechanisms in the Starved Regime," Tribology Series, 36, 1999, 483–492.

[41] Gershuni, L., Larson, M. G. and Lugt, P. M., "Lubricant Replenishment in Rolling Bearing Contacts," Tribology Transactions, 51, 5, 2008, 643–651.

[42] Nogi, T., "An Analysis of Starved EHL Point Contacts with Reflow," Tribology Online, 10, 1, 2015, 64–75.

[43] Goksem, P. G. and Hargreaves, R. A., "The Effect of Viscous Shear Heating on Both Film Thickness and Rolling Traction in an EHL Line Contact – Part I: Fully Flooded Conditions," ASME Journal of Tribology, 100, 3, 1978, 346–352.

[44] Goksem, P. G. and Hargreaves, R. A., "The Effect of Viscous Shear Heating on Both Film Thickness and Rolling Traction in an EHL Line Contact – Part II: Starved Conditions," ASME Journal of Tribology, 100, 3, 1978, 353–358.

[45] Kaneta, M., Shigeta, T., Yang, P., "Effects of Compressive Heating on Traction Force and Film Thickness in Point EHL Contacts," ASME Journal of Tribology, 127, 2, 2005, 435–442.

[46] Johnson, K. L., Greenwood, J. A. and Poon, S. Y., "A Simple Theory of Asperity Contact in Elastohydrodynamic Lubrication," Wear, 19, 1, 1972, 91–108.

[47] Bowden, F. P. and Tabor, D., "The Friction and Lubrication of Solids," Oxford, 1, 1950.

[48] Bowden, F. P. and Tabor, D., "The Friction and Lubrication of Solids," Oxford, 2, 1964.

Taisuke Maruyama

Masayuki Maeda

Ken Nakano

Assistive Robot to Aid Healthcare Staff in Patient Transport

Toshihiko Okamura
Technology Development Division Headquarters, New Field Products Development Center,
Technology Development Department 1

Abstract

Recent workstyle reforms and the ongoing decrease in the working population are creating significant challenges for staffing in healthcare facilities. We developed a robot to assist in the transport of patients on stretchers in hospitals as a way to ease the burden during a labor shortage and support healthcare staff with this physically demanding task. Through an implementation project sponsored by Kanagawa Prefecture, we compared the physical burden of moving patients on a stretcher with and without the assistive robot at Shonan Kamakura General Hospital. Using the Ovako Working Posture Assessment System (OWAS), we found that the manual transport of stretchers is AC4, a work posture with a very harmful effect on the musculoskeletal system. Using the assistive robot reduces the OWAS level to AC1, the lowest level of risk to the healthcare provider.

1. Preface

Japan, known for its cutting-edge medical technology, offers daily access to high-quality healthcare services. However, this advanced system heavily depends on the long hours and dedication of its doctors. Given that doctors often continue to treat patients and perform surgeries despite exhaustion from overnight shifts, it is clear that the current medical system requires improvements to ensure patient safety and the well-being of healthcare workers. Against this backdrop, the Ministry of Health, Labour, and Welfare (MHLW) is implementing working-style reform for doctors in FY2024. This reform aims to optimize doctors' workloads, focusing on agreements related to working hours, including a standard limit of 960 hours of overtime per year for practicing physicians.

While this represents a significant step forward in terms of keeping doctors healthy and reducing medical errors, the healthcare industry also must move away from traditional staffing practices that overburden healthcare facilities. In addition, the looming "2030 problem" exacerbates this concern—specifically, as the population continues to decline, with falling birthrates and an aging demographic, and where approximately 30% of the population will be 65 or older by 2030, it will become more difficult than ever to secure sufficient healthcare workers. To address this, healthcare facilities need to embrace new solutions for workforce shortages while also enhancing their operational efficiency. This can be achieved by shifting some tasks from doctors to other healthcare professionals, and by incorporating robots to take over some of the work.

In this article, we discuss the development of a robot designed to assist with patient transport, created after observing and analyzing the tasks performed by healthcare staff at Tokushukai Shonan Kamakura General Hospital (Medical Corporation). The robot addresses the physical strain experienced by nurses and nursing assistants during stretcher-based patient transport. With this robot, the OWAS method[1] for posture assessment showed a reduction in physical stress and burden on the healthcare staff, confirming its effectiveness in alleviating the strain associated with patient transport.

2. Ward Observation

We observed and analyzed the tasks of nurses and nursing assistants at Tokushukai Shonan Kamakura General Hospital (Medical Corporation) to identify the actual needs of a healthcare facility. Our analysis revealed that the daily task of transporting patients on stretchers is physically demanding and thus places a significant burden on the staff.

A typical medical stretcher weighs approximately 70 kg, and when transporting a patient who weighs between 50 and 70 kg, the total weight reaches 120 to 140 kg. Since nurses and nursing assistants routinely transport patients for check-ups, they frequently lift, turn, and stop, which can lead to strain on their backs and knees. Furthermore, because stretchers are long and horizontal, they can be difficult to maneuver, particularly for smaller nurses and nursing assistants, who are often women. This adds to the physical burden and increases the risk of handling errors.

Hospital administrative staff face additional challenges, such as concerns about health risks for nurses and nursing assistants caused by the physical strain of stretcher transport, the cost of repairing healthcare facilities damaged by stretchers due to their mishandling, and stretcher transport quality in relation to patient comfort, which can vary from one staff member to another.

3. Patient Transport Assistance Robot

After observing and analyzing stretcher transport work, we developed a remotely controlled patient transport assistance robot with the aim of reducing the physical burden on nursing staff.

The concept behind the robot is to use existing hospital assets and not limit its application to specific types of stretchers. For instance, it can be attached to the currently used stretchers, providing a versatile and adaptable solution for patient transport. Moreover, the robot comes equipped with five key functions (Figure 1) designed to meet these requirements and facilitate smoother, safer transport.

(1) Motor assistance allows for movement in all directions
(2) Easy connection with an elevator
(3) Replaceable battery supports continuous operation
(4) Intuitive remote-control operation
(5) Stretchers can be used with attachment devices

4. Kanagawa Prefecture's FY2022 Robot Implementation Project for New Coronavirus Infectious Disease Control

The patient transport assistance robot has been chosen for Kanagawa Prefecture's FY2022 Robot Implementation Project for New Coronavirus Infectious Disease Control, a program that promotes the use of robots to help combat coronavirus infections. The robot has been deployed to assist with stretcher transport for patients in wards at Tokushukai Shonan Kamakura General Hospital (Medical Corporation). Specifically, nursing assistants at the hospital use the robot to transport patients by stretcher.

1. Motor assistance allows for movement in all directions
2. Easy connection with an elevator
3. Replaceable battery supports continuous operation
Patient transport assistance robot
Remote control
4. Intuitive remote-control operation allows for equal transport quality from all staff
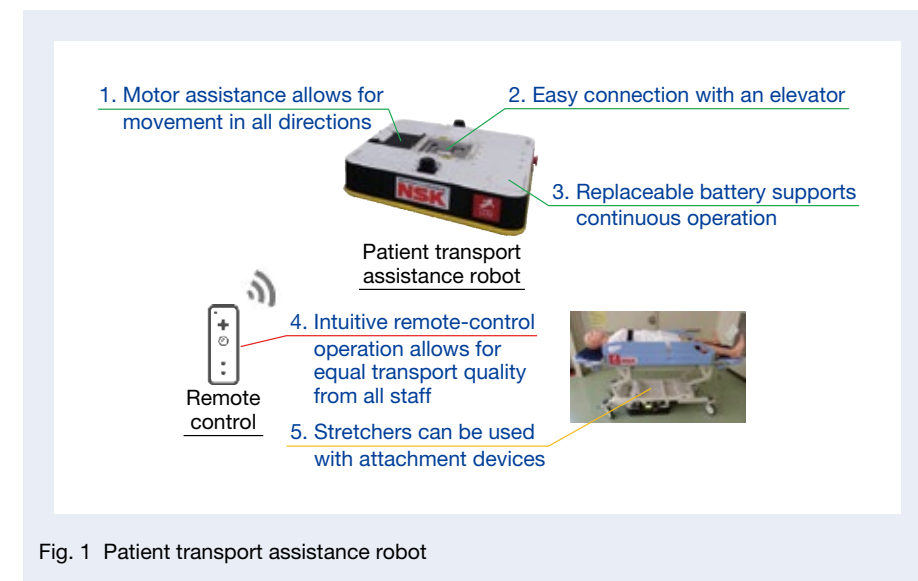5. Stretchers can be used with attachment devices

Fig. 1 Patient transport assistance robot

5. Whole Body Assessment Method— Assessment According to the OWAS Method

While seeking a method for assessing the physical burden associated with stretcher transport, we found that there is currently no established quantitative assessment method for doing this. We therefore focused on the OWAS method, a whole-body assessment approach used by the Labor Standards Inspection Office and others. The OWAS method, which dates back to 1997, involves categorizing body positions into segments (back, upper legs, lower legs, and arms) to assess posture-related burden and determine the need for ergonomic improvements based on an AC (action category) value.

However, because it requires observing and scoring a worker's posture at regular intervals, it can be time-consuming and require significant expertise. Given these limitations, we turned to PosCheck, an automatic workload measurement system developed by Bionet Laboratories, Inc., to enhance accuracy and reproducibility while reducing the potential for arbitrary scoring. PosCheck uses a 3D camera to automatically determine the workload of a healthcare employee every second, without requiring the subject to wear any special equipment. This allows for a less intrusive assessment of nurses' and nursing assistants' physical burden, by simply filming their routine activities. For this study, Bionet Laboratories, Inc. handled the entire process to prevent measurement errors caused by improper equipment installation, and their role included everything from equipment setup to measurement and analysis.

The measurement site was a corridor corner in the injury ward of Shonan Kamakura General Hospital, where we assessed physical burden during stretcher transport under the following conditions.

1. Transport worker: Nursing assistant (40s)
   Transport subject: Our employee playing the role of an elderly patient (approx. 50 kg)
2. Transport worker: Nursing assistant (70s)
   Transport subject: Our employee playing the role of an elderly patient (approx. 70 kg)
Note: The nursing assistants were employees of Shonan Kamakura General Hospital.

Our analysis showed that at corridor corners during current stretcher transport, even highly skilled nursing assistants face considerable physical strain, regardless of their age or the weight they are transporting. This strain is classified as AC4, indicating that the associated posture is "very detrimental to the musculoskeletal system, and improvements to working conditions should be made immediately" (Figure 2).

In contrast, when using a patient transport assistance robot, the stretcher transport is controlled remotely with the operator walking, resulting in much less physical strain. This method consistently scored an AC1, indicating that "the burden on the musculoskeletal system caused by this posture is not a problem, so no improvements to these working conditions are necessary."

The OWAS method thus demonstrates that using a patient transport assistance robot significantly reduces the physical burden on nursing assistants (Figure 3).
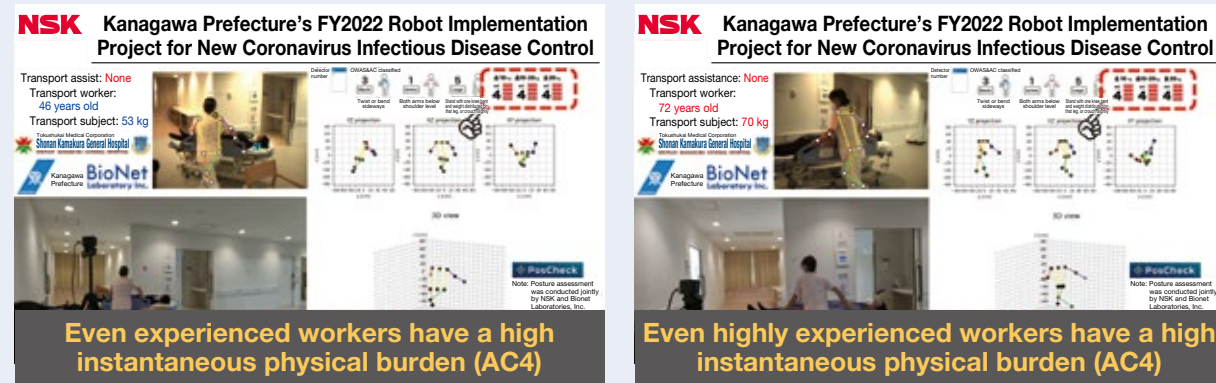

Fig. 2 Physical burden when moving stretchers normally (OWAS analysis results)
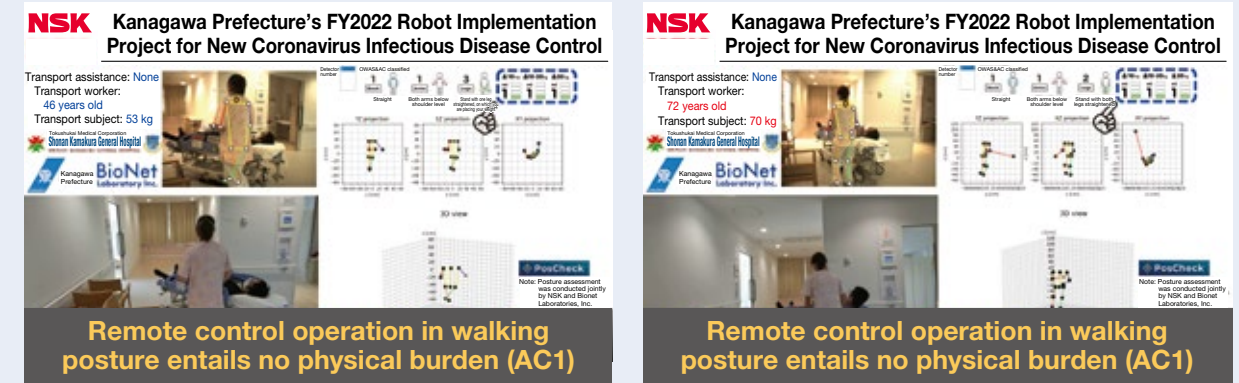

Fig. 3 Physical burden when moving a stretcher using the patient transport assistance robot (OWAS analysis results)

6. Postscript

Using the OWAS method, we demonstrated that a patient transport assistance robot can significantly reduce the physical burden on nursing assistants during stretcher transport. Furthermore, nursing assistants who have used the robot confirmed this, reporting a noticeable reduction in physical strain, reinforcing the conclusion that this robot effectively eases their workload.

However, there is currently no widely accepted method for quantitatively assessing the physical burden of stretcher transport. This study applied the OWAS method, which has the longest track record in whole-body assessment, to provide a basis for evaluation where no standard methodology exists. The OWAS method is considered a reliable starting point for assessing the strain involved in stretcher transport.

More recently, Rapid Entire Body Assessment (REBA)[2] has emerged as a more practical approach, and there is hope that future studies will adopt REBA for a more thorough assessment of physical burden.

In healthcare environments where lives are at stake, healthcare professionals face immense mental and physical demands. In our study, we aimed to show how robots can help alleviate some of that burden, even if only slightly. We hope that more people will become aware of this project through this article and engage with the effort to develop robots that can be seamlessly integrated into healthcare facilities.

References

1) Karhu, O., Kansi, P., et al. Correcting working postures in industry: a practical method for analysis. Applied Ergonomics. 1977, 8 (4), pp. 199–201, doi: 10.1016/0003-6870 (77) 90164–8.
2) Hignett, S. and McAtamney, L., Rapid entire body assessment (REBA). Applied Ergonomics. 2000, 31 (2), pp. 201–205, doi: 10.1016/s0003–6870 (99) 00039–3.

Toshihiko Okamura

J-Type ROBUSTDYNA™ Angular Contact Ball Bearings for Machine Tool Spindles

With the shift toward electric vehicles (EVs) in recent years, there has been an increasing demand for machine tools, such as automotive parts processing machines, to handle heavier cutting and tougher materials. As a result, main spindles must now balance heavy-duty cutting with high-speed operations, requiring higher load capacities. This article introduces several technological requirements that machining centers have demanded in recent years, focusing specifically on the needs of main spindles and the bearings that address those requirements (Figure 1).

While bearings for main spindles must offer both high load capacity to withstand heavy cutting and high-speed rotation like conventional bearings, no products have successfully met both demands until now. NSK has developed and added to its product lineup the ROBUSTDYNA™ Series: J-Type, designed to address the above problem. The new series improves upon the H-Type of the ROBUST™ Series (hereinafter the "conventional product").

diameter balls, to achieve both high load capacity and high-speed rotation. In addition, the rolling elements are made of ceramic materials for improved performance. We also used specialized materials, such as our proprietary high-speed heat-resistant steel and long-life steel, for the outer and inner rings, depending on the bearing type (Figure 2).

1. Composition, Structure, and Specifications

To develop the ROBUSTDYNA™ Series, we optimized internal specifications, including the use of larger-

Photo 1 J-Type of ROBUSTDYNA™ Series

Fig. 1 Example needs for machining centers

Series	ROBUST Series (Conventional bearing)		ROBUSTDYNA series (New bearing)	
Composition (Cross-section)	Ball Outer ring Inner ring		Ball Outer ring Inner ring	
Type	H-Type	X-Type	J-Type	X-Type
Part — Ball	Ceramic (Ball diameter: small)	Ceramic (Ball diameter: small)	Ceramic (Ball diameter: large)	Ceramic (Ball diameter: large)
Part — Outer and inner rings	Bearing steel	High-speed heat-resistant SHX steel	Long-life steel	High-speed heat-resistant SHX steel

Fig. 2 Specifications for ROBUSTDYNA™ Series

2. Features

2.1 Adoption of long-life steel

For the ROBUSTDYNA™ Series: J-Type, we used NSK's unique long-life steel (Figure 3). Furthermore, optimizing internal specifications has boosted the dynamic load rating by approximately 40% compared to the conventional product, leading to a bearing lifespan of up to six times longer. This improvement significantly enhances the long-term stability of spindle operation.

2.2 High load capacity

Optimizing internal specifications, including the adoption of larger-diameter balls, has increased the load capacity by approximately 15% compared to the conventional product. This enhancement supports the transition to heavier cutting and shorter processing times in machining centers (Figure 4).

2.3 High speed

Thanks to the optimizations, the new product achieves the same high-speed performance as the conventional product. This compatibility between heavy cutting and high-speed rotation leads to increased productivity.

3. Applications

The product is ideal for machine tools that perform heavy cutting and fast finishing, such as machining centers for general parts and automotive components.

4. Postscript

We remain committed to the further development of machine tools by creating new bearing technologies that meet the various evolving needs of the industry.
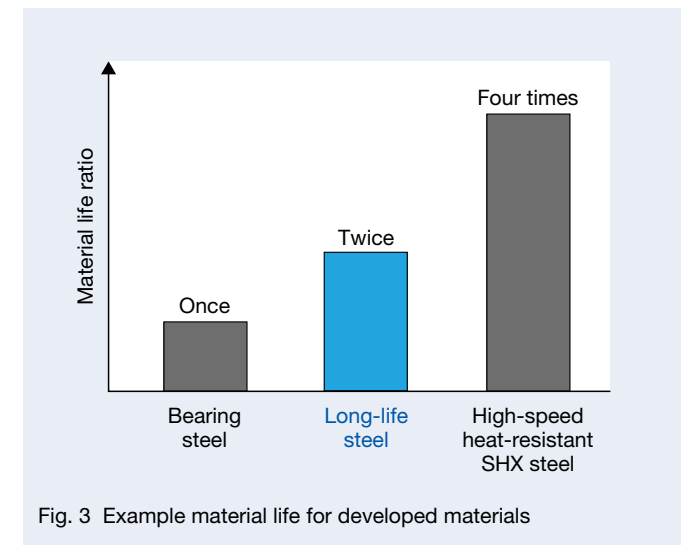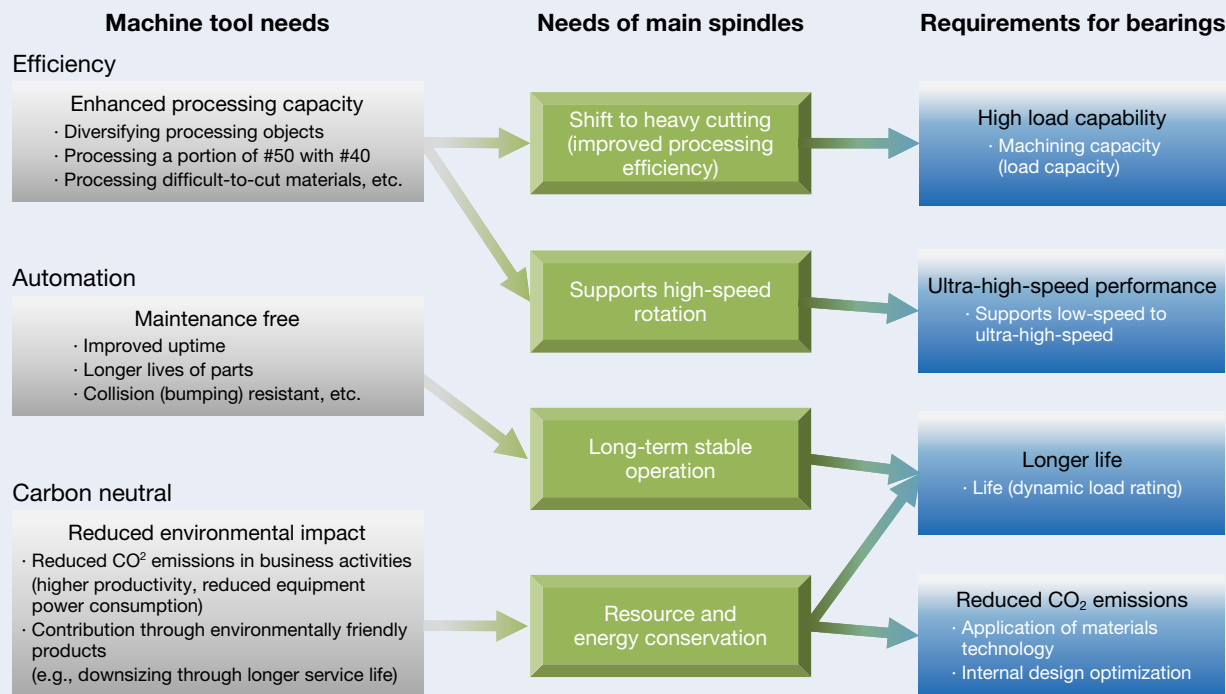

Fig. 3 Example material life for developed materials
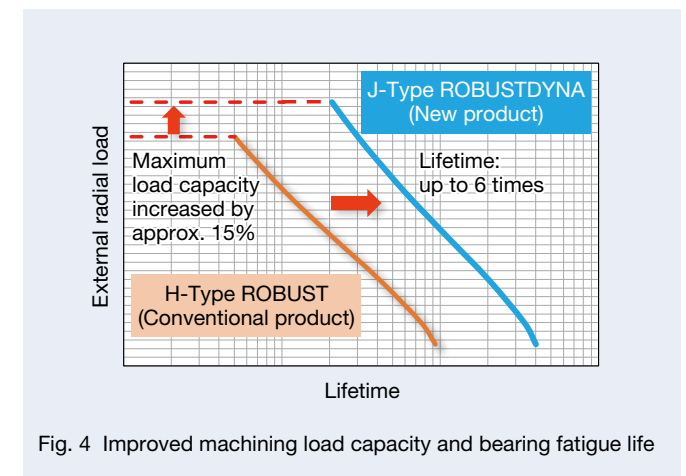

Fig. 4 Improved machining load capacity and bearing fatigue life

ROBUSTGRD™ Improved Seizure Resistance Grease

Machine tools require high productivity, so efforts are underway to increase both maximum spindle speed and load capacity. Oil-air lubrication is often used to lubricate spindle bearings to increase reliability. However, oil-air lubrication requires a sizable compressor and consumes a lot of power, as it continuously uses compressed air. Given the growing emphasis on carbon neutrality, there is increasing attention on downsizing equipment and reducing power consumption. Against this background, NSK has developed a new grease for machine tool spindle bearings, ROBUSTGRD™, which offers greater reliability.

1. Composition, Structure, and Specifications

ROBUSTGRD™ was developed with an optimized composition to ensure high reliability at high speeds and in coolant environments (Photo 1). Table 1 compares the composition of conventional products with that of ROBUSTGRD™.

Photo 1   ROBUSTGRD™ grease for enhanced seizure resistance

Table 1   Grease specifications

Composition	Conventional product	ROBUSTGRD™
Thickener	Urea	Special compound lithium soap
Base oil	Ester oil-based	Synthetic hydrocarbon oil-based
Consistency	NLGI Grade 2	
Water-resistant additive	Witihout	With

2. Features

2.1 Seizure resistance

In a seizure test under accelerated conditions, ROBUSTGRD™ resulted in more than five times the resistance to seizure compared to our conventional product (Figure 1).

2.2 Coolant resistance

By formulating a water-resistant additive with a proven track record in our automotive hub bearings and steel bearings, ROBUSTGRD™ reduces the possibility of moisture entering the lubrication area and disrupting oil film formation (Figure 2). ROBUSTGRD™ is also less prone to changes in consistency caused by moisture from coolant, compared to conventional products (Figure 3). Also, the water-resistant additives contribute to excellent corrosion resistance (Table 2).
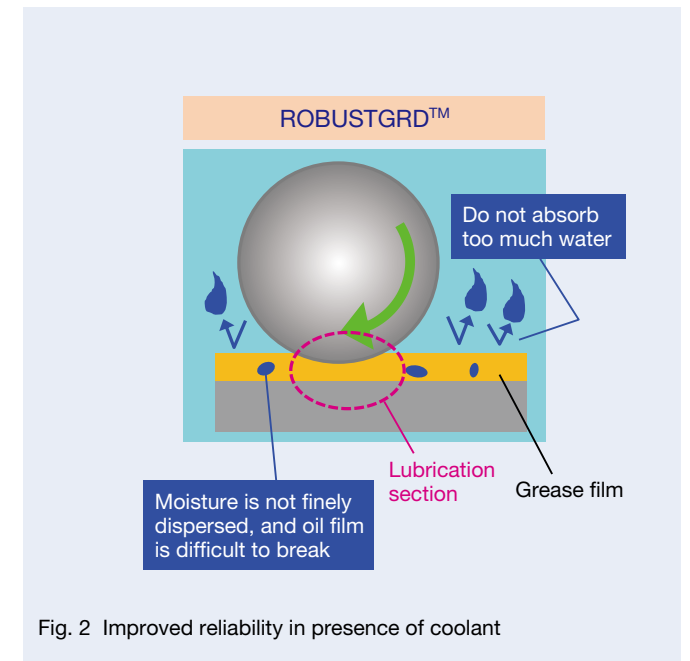
3. Applications

Machine tool spindles for general parts and automotive components are sometimes operated with oil-air lubrication, even under conditions where grease lubrication is possible, to improve reliability. With ROBUSTGRD™, it is possible to switch from oil-air lubrication to grease lubrication for machine tool spindles, reducing the need for compressed air while maintaining the same level of reliability.

4. Postscript

We will continue to develop environmentally friendly grease lubrication to broaden their applications and support machine tools in achieving carbon neutrality.
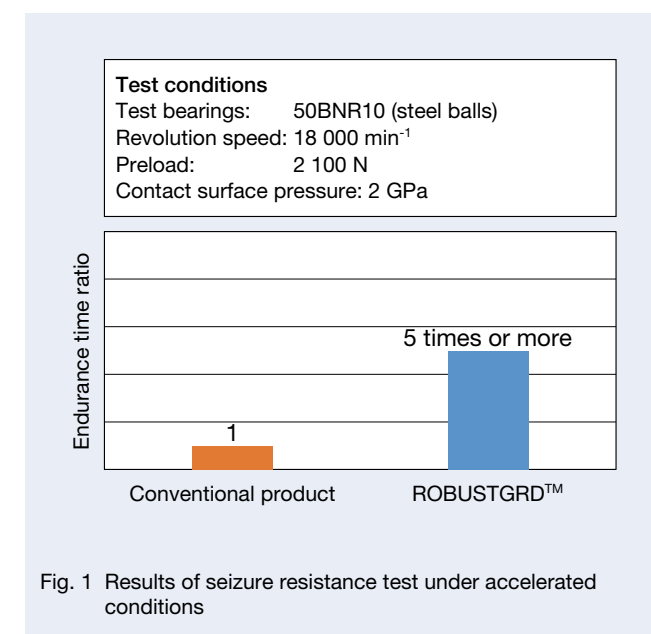

Test conditions
Test bearings: 50BNR10 (steel balls)
Revolution speed: 18 000 min⁻¹
Preload: 2 100 N
Contact surface pressure: 2 GPa

Fig. 1   Results of seizure resistance test under accelerated conditions

Fig. 2   Improved reliability in presence of coolant

Compliant with ASTM D1831
Water absorption roll stability test
25°C, 24 hr, 165 min⁻¹, 10% water content
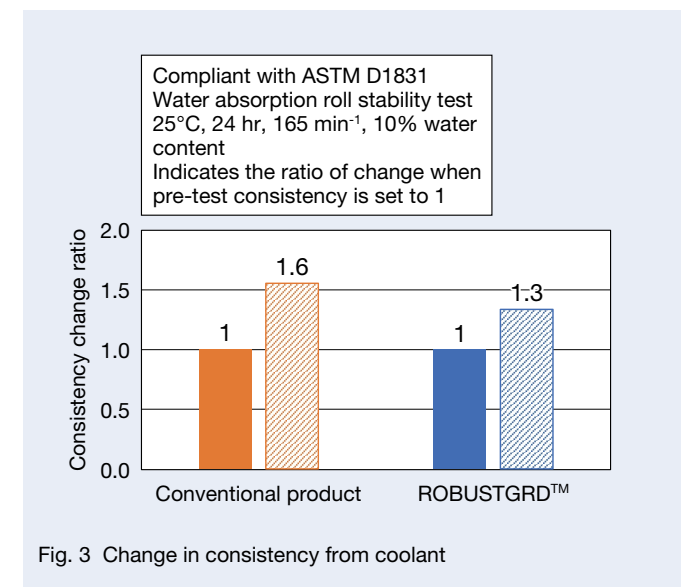Indicates the ratio of change when pre-test consistency is set to 1

Fig. 3   Change in consistency from coolant

Table 2   Test results for rust prevention

Conventional product	ROBUSTGRD™
#3	#1

Criteria   #1: No occurrence
#2: Within 3 points of small corrosion
#3: #2 or higher

Compliant with ASTM D1743-73
Anti-Corrosion Test
25°C, 0.5% saltwater, 5% content, 24 hr

NSK Ball Screw for High-Load Drives: Long-Life Specification

To increase the productivity of electric injection molding machines, the "high cycling" process is being developed by increasing the feed rate. High cycling increases the distance traveled by the ball screw per unit of time, requiring longer-lasting ball screws. To meet this demand for heavy-load drive ball screws with extended lifespans, we have developed a long-life ball screw option (Photo 1).

1. Composition, Structure, and Specifications

When an axial load acts on a ball screw, the nut, screw shaft, and balls are elastically deformed by the load. The load generated per ball inside the nut is not uniform, as the load near the point of load action is greater, resulting in a non-uniform load distribution. As the load acting on the ball screw increases, the variation of the load distribution inside the nut also increases.

Since the outset of developing ball screws for heavy-load drives—designed to endure significant loads—we have focused on load distribution within the nut. To achieve a more uniform load distribution, we have recommended specific circulation circuit arrangements and ball screw mounting orientations to our customers.

As the demand for higher load capacity and longer service life grew in recent years, adding a circulation circuit became common to increase the number of balls under load. However, this extended the nut's length, resulting in more nut deformation and greater load distribution variation. To address this, we have developed internal specifications by integrating the following technologies.

· High-precision machining technology:
 Development of specialized machining equipment
· Analysis technology:
 Use of real digital twins
· Precision measurement technology:
 Correlating processing data with measurement data

2. Features

In Figure 1, Example A shows a ball screw in use. where circuits 1 and 5 experience higher loads than circuits 2 through 4. The fatigue life of a ball screw is calculated at the position where the load is greatest. Efforts are thus being made to reduce the maximum

load by distributing the load acting on each ball so that the load distribution is uniform. We have developed a long-life option that optimizes the load distribution in each circuit by obtaining and applying the optimal internal specifications for the operating conditions through simulation. This reduces the maximum ball load and extends the ball screw's fatigue life (Figure 2).
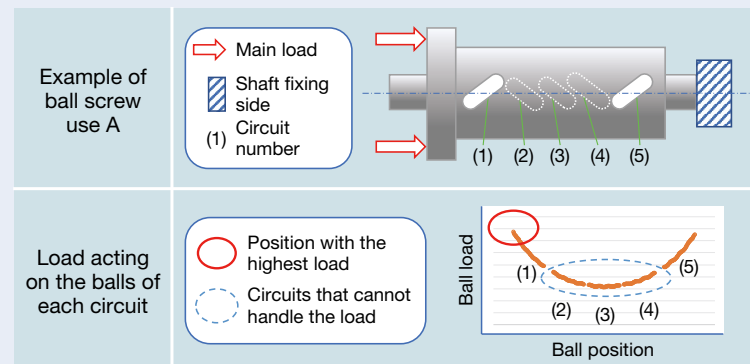

Photo 1 HTF-SRC Model

Fig. 1 Relationship between load direction and load distribution (Example A)
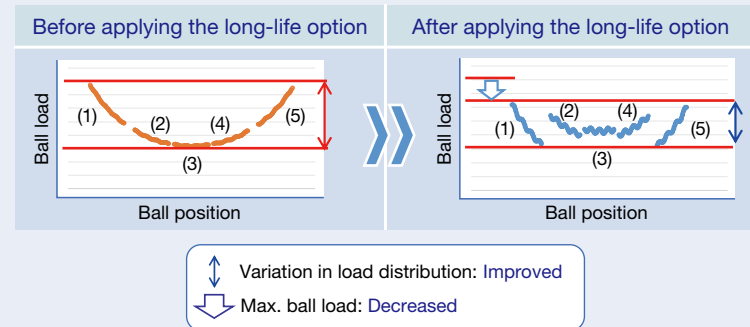

Fig. 2 Effects of long-life specification (Example A)

In use case B, shown in Figure 3, circuit (1) has a load that is more concentrated compared to that of other circuits. But with our long-life option, the lifespan of the circuit can be extended (Figure 4).

Key features of the long-life option include:

(1) Up to twice as effective in extending the service life compared to conventional products[1]. Table 1 shows an example of simulation results from a sample specifications.
(2) Even with the long-life option, the nut's dimensions remain fully compatible with conventional designs and maintain the usability of the ball screw while also facilitating easy replacement.
(3) With the longer lifespan, it is possible to consider the advantages of downsizing (Figure 5).

3. Applications

The long-life option is suitable for applications that require high load capacity and load carrying capacity, such as electric injection molding machines and servo presses. The corresponding ranges are shown below.

· Screw shaft outer diameter:
  ϕ100 to ϕ200 mm
· Model: HTF-SRC type (to be expanded sequentially)

4. Conclusion

The long-life option introduced here will enhance the reliability and productivity of industrial machinery. Expanding the available range will further drive the electrification of industrial machinery and reduce environmental impact.
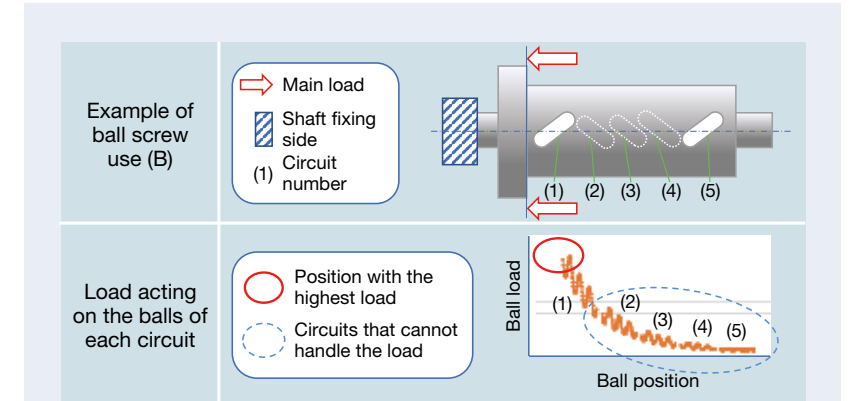

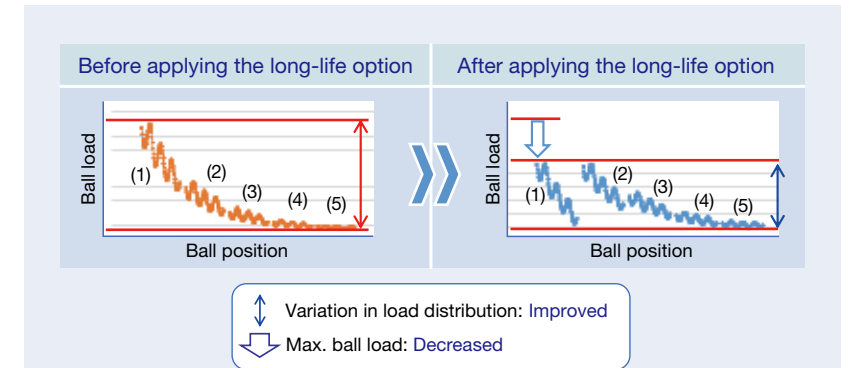Fig. 3 Relationship between load direction and load distribution (Example B)

Fig. 4 Effects of long-life specification (Example B)

Fig. 5 Possible advantages of downsizing

Table 1 Simulated life-extending effects

Mounting direction	Ball screw specifications	Working load, kN	Specifications	Service life
	Screw Shaft O.D.: ϕ 100 Lead: 20 mm	600	Standard	1
			Long-life option applicable	1.4
	Screw Shaft O.D.: ϕ 100 Lead: 20 mm (with options for high load capacity, S-HTF)	525	Standard	1
			Long-life option applicable	2.0

Ball Screw Unit for Electric Hydraulic Brake Systems

The electrification of powertrains, mandatory collision damage mitigation brakes, and increasingly sophisticated automated driving are all pushing up demand for electric brake boosters. Also, safer and more advanced vehicle control requires that these boosters deliver faster, more precise motion. For this reason, ball screws, which offer a superior response, efficiency, and positioning accuracy compared to sliding screws, are being increasingly used for a range of applications. The ball screw converts the rotational motion of the motor into a linear motion and generates the thrust required to boost the brake fluid pressure in the master cylinder.

NSK has been developing a broad selection of ball screws for automotive use. These include a ball screw unit for electric brakes that has a circulating mechanism with an internal deflector and is integrated with a bearing, which we introduce in this article.

1. Composition, Structure, and Specifications

Figure 1 shows the structure of the developed ball screw unit. The screw section includes a screw shaft and a nut with a spiral groove, a ball that rolls between them, a plastic internal deflector that circulates the ball within the nut, and a sleeve that holds the deflector in place. The inner ring of the bearing that supports the nut's rotation is integrated into the outer circumference of the nut. An anti-rotation device is mounted on the screw shaft to prevent the nut and screw shaft from rotating in unison.
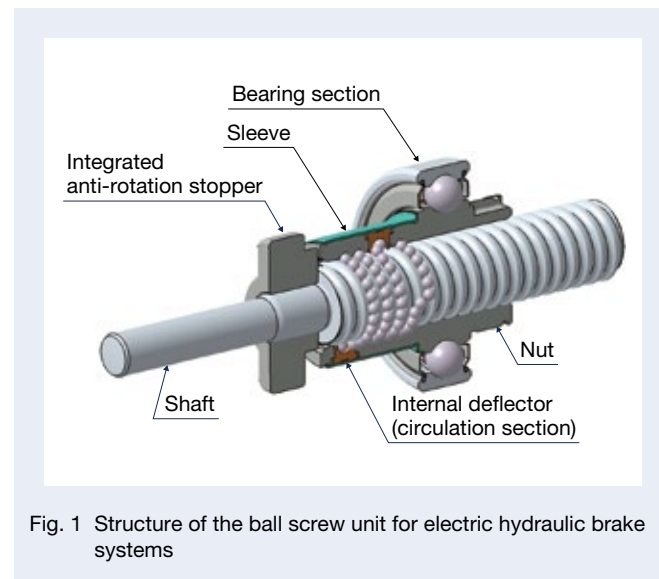

Fig. 1 Structure of the ball screw unit for electric hydraulic brake systems

2. Features

(1) Integrated bearings

The product features an integrated bearing section that supports the nut's rotation. By forming the bearing's inner ring raceway grooves directly on the outer diameter of the nut, a compact radial design is achieved (Figure 2). Press-fitting the bearing also reduces variations in ball screw clearance, significantly enhancing quality.
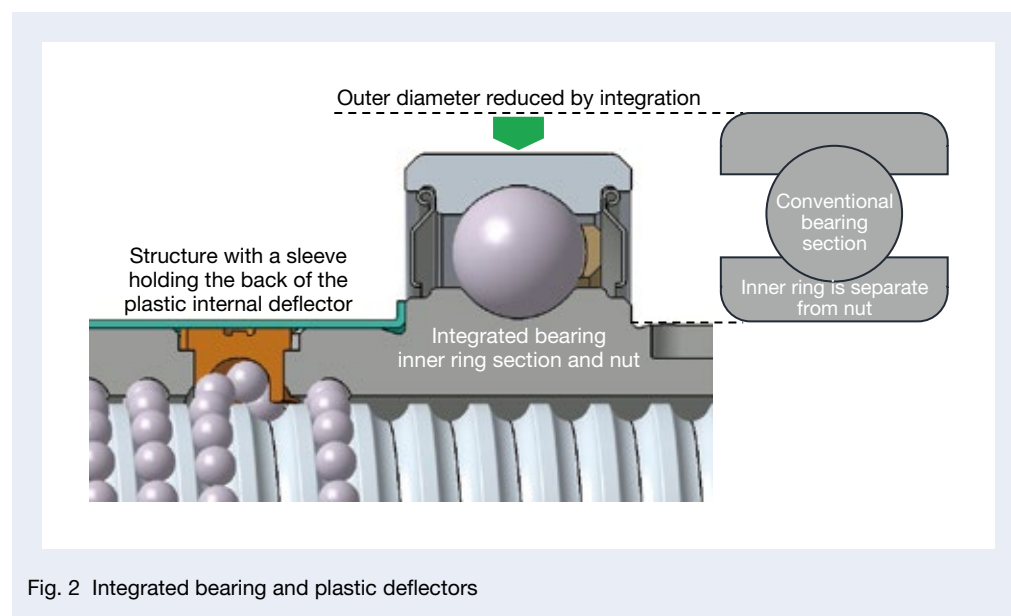
(2) Plastic internal deflector and sleeve

The product uses plastic internal deflectors for ball circulation. The cylindrical sleeve prevents the internal deflector from falling out of the nut (Figure 2). eliminating the need for press-fitting or press-tightening to secure the deflector. This simplifies assembly and supports low-cost, high-volume production.

(3) Integrated anti-rotation stopper

An anti-rotation component on the screw shaft prevents the nut and screw shaft from rotating in unison.

This "anti-rotation" also acts as a rotation stopper. When the screw shaft returns to its origin, a protrusion at the nut's end comes into contact with the anti-rotation component, stopping the nut's rotation and preventing the shaft from moving further in the opposite direction (Figure 3).
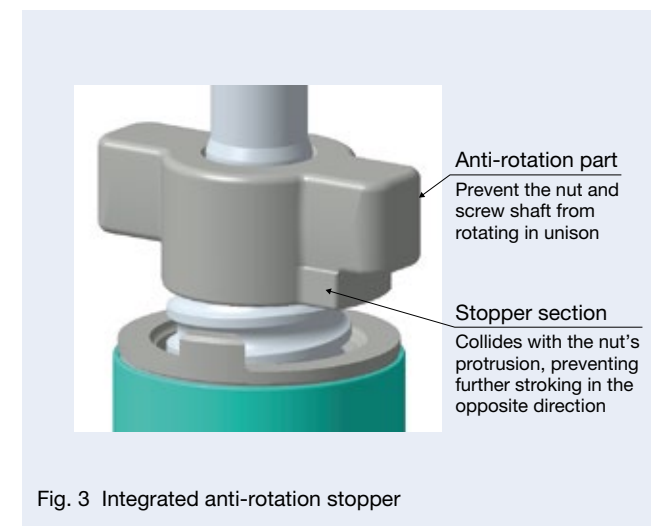

Fig. 3 Integrated anti-rotation stopper

3. Conclusion

The new product has already been adopted for electric hydraulic brake boosters for vehicles, mainly light trucks. This bearing-integrated ball screw unit with an internal deflector circulation mechanism adds to our existing lineup of mass-produced ball screw products.

Looking ahead, we aim to continue developing products that meet market demand and contribute to greater safety and comfort in the automotive industry.

Photo 1 Mass-produced ball screw for electric hydraulic brake boosters

Fig. 2 Integrated bearing and plastic deflectors

Integrated Bearing and Resolver

With the critical need to save vehicle space and extend the navigation range by reducing vehicle weight, demand is increasing for compact and lightweight motor/reducer units for electric vehicles such as HEVs and EVs. Meanwhile, the installation of a resolver, mounted on the shaft of the motor that powers the vehicle, to determine the angle of rotation for motor control, requires a certain amount of axial space due to magnetic forces and assembly constraints.

To address these issues, we have developed the integrated bearing and resolver that allows for a more compact and lightweight motor unit with a shorter shaft. The bearing even simplifies manufacturing, as the resolver and bearing are assembled to the unit at the same time.

1. Composition, Structure, and Specifications

Figure 1 shows the components of the integrated bearing and resolver. The resolver stator is riveted to a plastic holder, which is then press-fitted into a groove in the bearing outer ring, thus integrating it with the bearing. This design eliminates the need for conventional through-holes on the resolver periphery and thus allows for a significant reduction in the radial dimensions. The axial dimensions can also be reduced through the modified layout (described in the next section), which contributes to an overall lighter and more compact unit.

Photo 1 Integrated bearing and resolver

Fig. 1 Structure of the integrated bearing and resolver
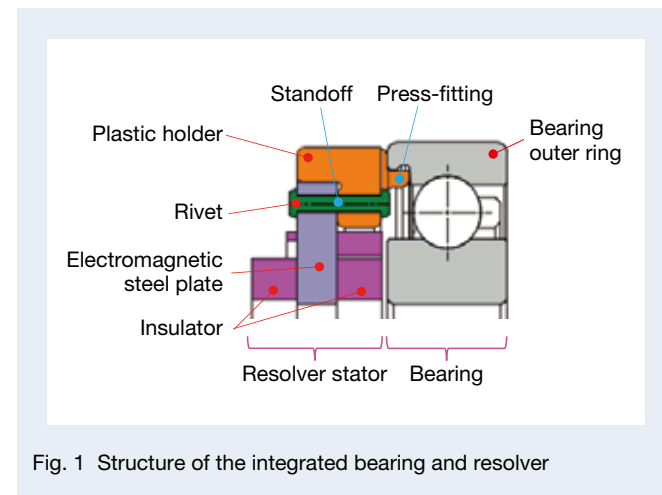
2. Features

Figures 2 and 3 illustrate the conventional resolver and bearing configurations. As for the structure, layout methods are generally divided into two types. The order of arrangement for Type A, shown in Figure 2, is resolver, bearing, and motor rotor, whereas the order for Type B, shown in Figure 3, is bearing, resolver, and motor rotor.

Both layouts require additional space due to clearance requirements. Furthermore, Type A requires additional space for mounting the resolver, while in Type B, the resolver is positioned farther away to avoid the magnetic influence of the motor rotor, and the bearing is placed on the motor cover side, contributing to an increase in the shaft length of the unit.

On the other hand, if the resolver is integrated with the bearing, the arrangement is similar to that of Type A (Figure 4), but downsizing through integration can reduce the shaft length. In addition, compared to Type B, this structure keeps the resolver in nearly the same position but relocates the bearing, originally on the motor cover side, to between the resolver and rotor, which leads to further shortening of the shaft length. As the reduction of shaft length that can be carried out is, from the results of benchmarking current market products, estimated to be about 60 mm, a significant effect of reducing shaft length is expected.
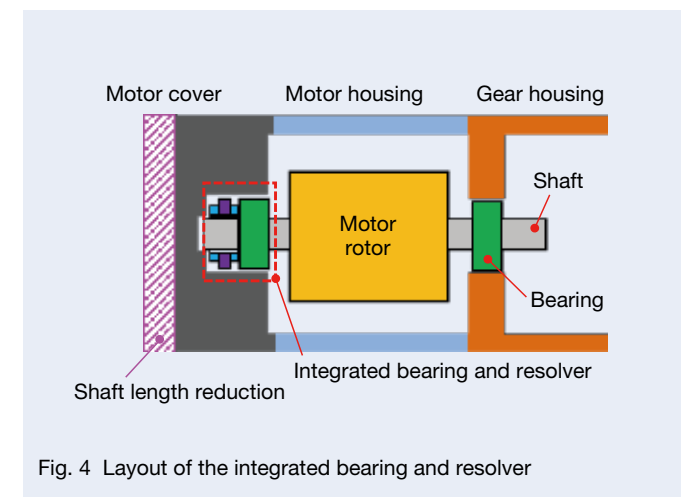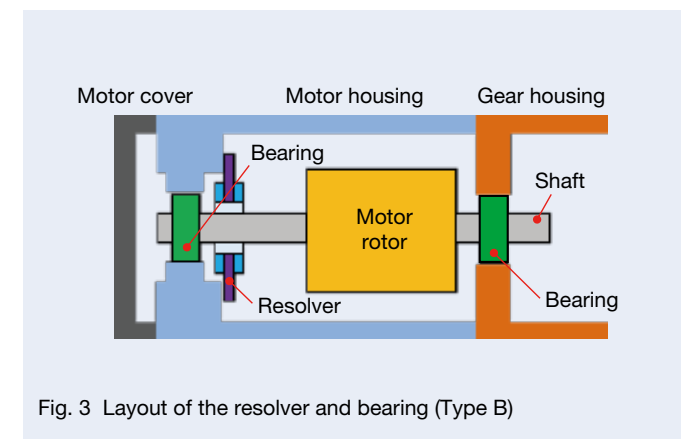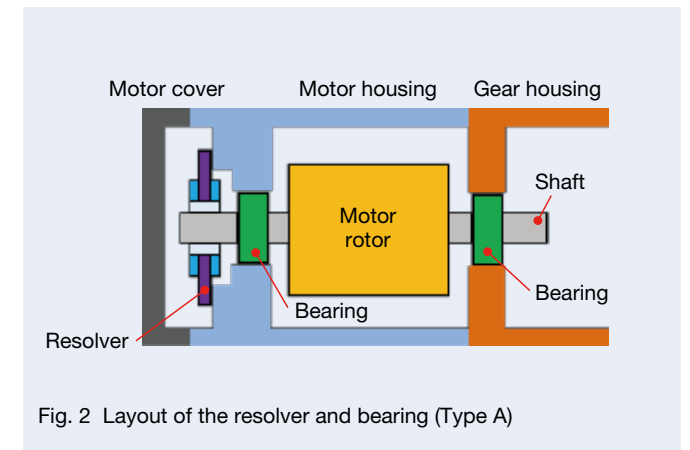
Furthermore, the new structure's compactness and lightweight design resulted in a 40% reduction in both the inner and outer diameters and a 75% reduction in weight within the resolver stator section. By integrating the bearing (supporting component) and resolver (sensor component) into a single unit, the impact of shaft runout is minimized, which improves resolver sensing accuracy by 36%.

3. Applications

The integrated bearing and resolver facilitates the downsizing of drive motor units for electric vehicles, thereby improving fuel efficiency, reducing electricity costs, extending navigation range, and enhancing comfort.

4. Conclusion

The integrated bearing and resolver is a development that can contribute to smaller drive motor units. We aim to continue developing new products that meet market needs, further improving electric vehicle efficiency.

Fig. 2 Layout of the resolver and bearing (Type A)

Fig. 3 Layout of the resolver and bearing (Type B)

Fig. 4 Layout of the integrated bearing and resolver

Deep Groove Ball Bearing with Enhanced Overhang Strength for EVs

Concerns about global warming and other environmental issues are driving social movements toward carbon neutrality, making electric vehicles (EVs) increasingly appealing due to their lower environmental impact. For EVs to gain broader acceptance, extending their driving range by reducing energy consumption is essential, and this is creating demand for compact, lightweight, and low-friction bearings in EV drive units, also known as eAxles.

One approach to reduce bearing friction in eAxles is by replacing conventional tapered roller bearings with deep groove ball bearings on high-load gear shafts. However, deep groove ball bearings typically have a smaller load capacity, necessitating larger bearings—a specification contrary to the goals of downsizing and weight reduction.

To address this, NSK has developed a deep groove ball bearing with a unique groove shoulder design and enhanced overhang strength. This innovation allows for a more compact, lightweight deep groove ball bearing with higher load capacity.

1. Composition, Structure, and Specifications

The new deep groove ball bearing enhances overhang strength by incorporating the following two key design changes:
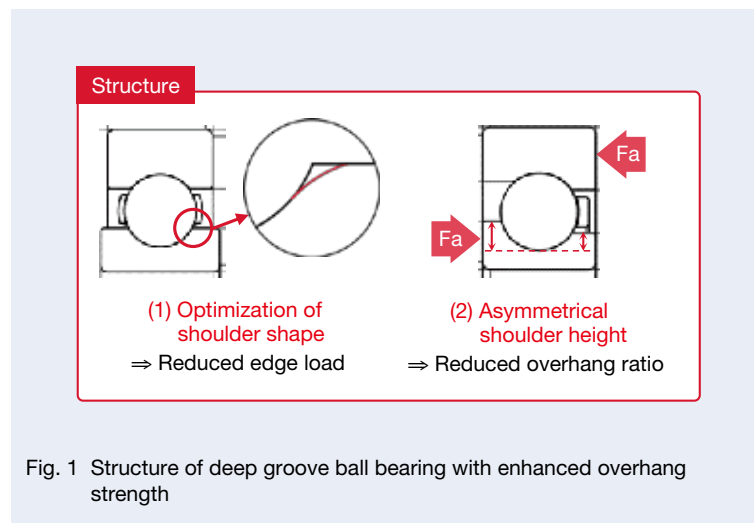
(1) Optimization of the groove shoulder shape to reduce the edge surface pressure when the contact ellipse of the ball overhangs on the groove shoulder
(2) Increased height of the axial load-loaded groove shoulder to reduce its overhang

The amount of the contact ellipse's overhang on the groove shoulder varies with the raceway groove's curvature, and this has a trade-off with the contact pressure, which impacts bearing life. Therefore, the new product optimizes the groove curvature and enhances overhang strength, allowing for reduced contact pressure and consequently extending the bearing's lifespan.

2. Features

· Special groove shoulder specification enhances groove shoulder overhang strength
· Optimized groove curvature reduces contact pressure and extends service life
⇒ Contributes to the downsizing and weight reduction of deep groove ball bearings

Fig. 1 Structure of deep groove ball bearing with enhanced overhang strength

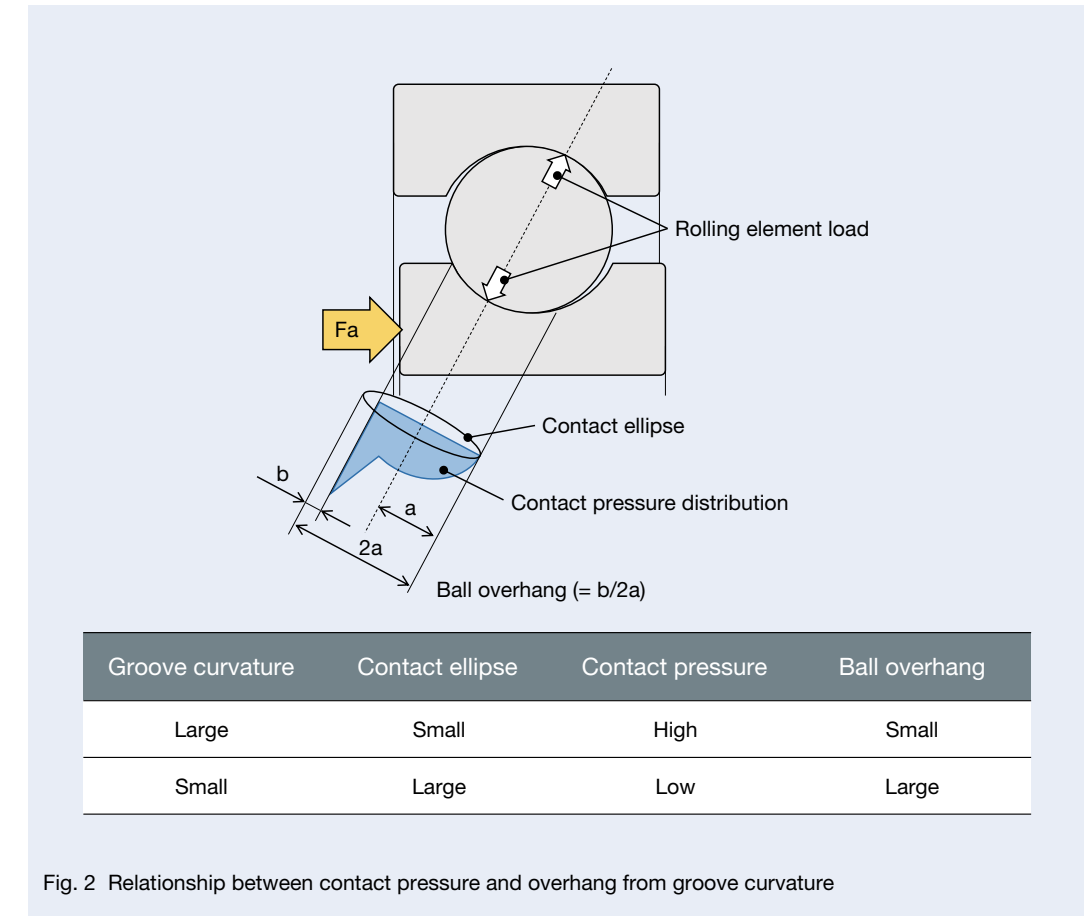| Groove curvature	Contact ellipse	Contact pressure	Ball overhang
Large	Small	High	Small
Small	Large	Low	Large

Fig. 2 Relationship between contact pressure and overhang from groove curvature

3. Applications

This technology allows for smaller, lighter deep groove ball bearings, reducing the size and weight of the eAxle. In addition, by replacing tapered roller bearings with deep groove ball bearings, bearing friction is reduced, potentially extending EV driving range and lowering electricity costs.

4. Conclusion

As a result of optimizing the groove curvature and reinforcing overhang strength by applying a special groove shoulder shape, the new bearing offers a greater load capacity while maintaining low-friction characteristics.

Looking ahead, NSK will remain committed to developing products that meet market needs and to contributing to the realization of carbon neutrality while supporting the proliferation of EVs and other environmentally friendly vehicles.

Table 1 Downsizing and weight reduction for the new bearing

	Standard	Spec. 1	Spec. 1 + 2
Outer diameter	ϕ105 mm	ϕ100 mm	ϕ91 mm
Bearing weight	1.06 kg	0.94 kg	0.91 kg

Compact and Lightweight Redundant Column-Type EPS

As cars become increasingly sophisticated, electric power steering (EPS) systems are expected to surpass conventional safety standards to meet the demand for critical components for advanced driver-assistance systems (ADAS). This includes ensuring continued power assistance even during malfunctions, so the EPS is required to achieve higher safety standards, lower failure rates, and quantifiable performance indicators.

In the EPS motor and ECU, the systems responsible for detecting steering force and generating assist force should operate independently to ensure reliability. This has involved adding redundant input/output systems, which means more components. However, it has also led to such issues as increased size, weight, and cost compared to conventional systems.

To address these issues, we have developed a compact, lightweight, and low-cost motor control unit (MCU) that integrates the motor and ECU, allowing for continued operation even when a malfunction occurs (Figure 1).

1. Composition, Structure, and Specifications

Figure 2 shows the structure of the new MCU. In conventional MCUs, the motor and ECU are separate units. With our new MCU design, however, the motor cover acts as the ECU case, housing the circuit board. This structure allows for heat from both the motor and ECU to dissipate through a common heat sink integrated into the ECU case. The motor rotation angle sensor is mounted on the ECU circuit board instead of the motor board. This design features a motor section with the same diameter as a conventional product but is multi-pole. Enlarging the rotor diameter increases the amount of radial flux linkage and shortens the shaft length.
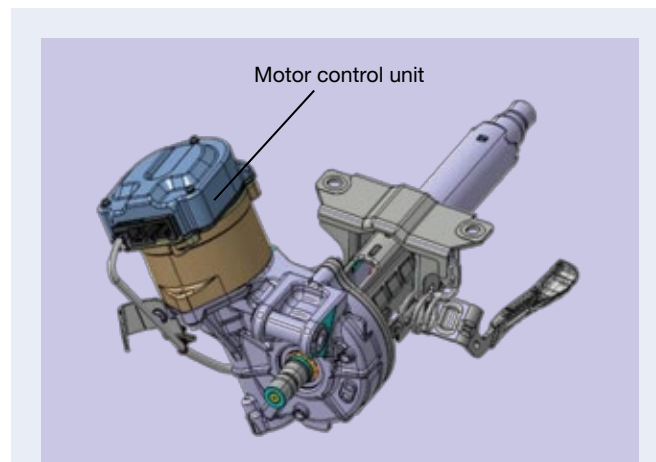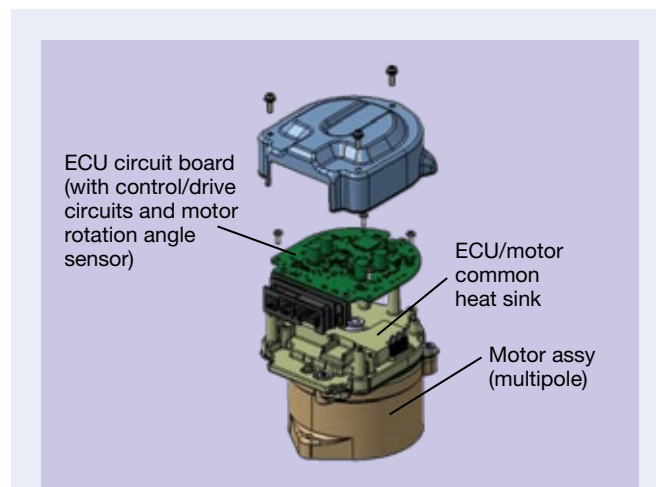

Fig. 1 Redundant column-type EPS

Fig. 2 Configuration of new motor control unit

2. Features

2.1 Integrated motor and ECU

Compared to conventional MCUs, our new design achieves the following three advantages in reduced size and weight. (Figure 3)

(1) A heat sink in the motor cover dissipates heat from both the motor and ECU, eliminating the need for a separate ECU case.
(2) Motor busbars are directly connected to the circuit board, removing the need for a connection structure with a terminal block.
(3) Relocating the motor rotation angle sensor to the ECU circuit board eliminates the need for internal wiring harnesses.

2.2 Motor multi-polarization

Motor torque is determined by the product of the number of poles, flux linkage, and current, and can be expressed by the following formula.

Motor torque: $T = pN$ (number of poles) $\times \phi$ (flux linkage) $\times Iq$ (current)

Increasing the number of poles reduces the magnetic flux per magnet, allowing for a thinner magnetic path in the stator. The back yoke can also be made thinner, so the winding section can be expanded on the stator's outer diameter side (Figure 4). Consequently, increasing the rotor diameter boosts radial flux linkage, resulting in higher output with the same size. Also, the shaft length can be shortened, making possible a reduction in the overall motor mass (Figure 5).

3. Applications

This new MCU design makes the EPS more compact and lightweight while ensuring continued functionality and easy installation. It supports the column-type EPS with a redundant design for functional continuity while reducing size and weight.

4. Conclusion

As vehicles with ADAS become mainstream and technology advances, there is a growing demand for more sophisticated features. To address this, our focus is on developing column-type EPS units that offer higher performance in a compact, lightweight design, creating a full product line to meet market demands.
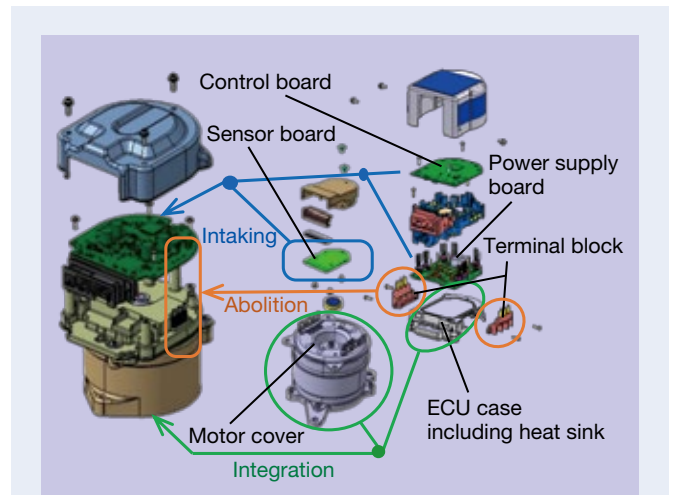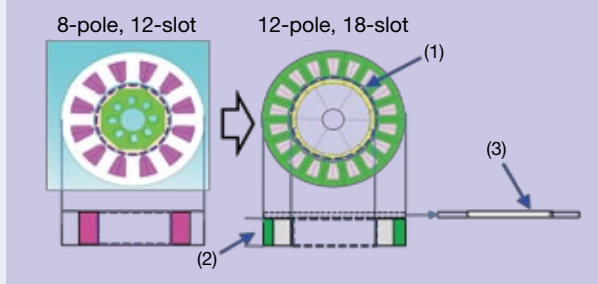

Fig. 3 Integrated motor and ECU

Fig. 4 Optimization by multi-polarization

Fig. 5 Configuration of multi-polarization core

Worldwide Sales Offices

NSK LTD.-HEADQUARTERS, TOKYO, JAPAN

Nissei Bldg., 1-6-3 Ohsaki, Shinagawa-ku, Tokyo 141-8560, Japan
P: +81-3-3779-7111   F: +81-3-3779-7431

●Africa

South Africa:
NSK SOUTH AFRICA (PTY) LTD.
SANDTON   25 Galaxy Avenue, Linbro Business Park, Sandton 2146, South Africa
P: +27-011-458-3600   F: +27-011-458-3608

●Asia and Oceania

Australia:
NSK AUSTRALIA PTY. LTD.
MELBOURNE ☆   100 Logis Boulevard, Dandenong South, Victoria, 3175, Australia
P: +61-3-9765-4400   F: +61-3-9765-4466

SYDNEY   Suite A315, 20 Lexington Drive, Bella Vista, New South Wales, 2153, Australia
P: +61-2-9839-2300   F: +61-2-8824-5794

BRISBANE   1/69 Selhurst Street, Coopers Plains, Queensland 4108, Australia
P: +61-7-3347-2600   F: +61-7-3345-5376

PERTH   Unit 1, 71 Tacoma Circuit, Canning Vale, Western Australia 6155, Australia
P: +61-8-9256-5000   F: +61-8-9256-1044

China:
NSK (SHANGHAI) TRADING CO., LTD.
JIANGSU   No.8 NSK Rd., Huaqiao Economic Development Zone, Kunshan, Jiangsu, China (215332)
P: +86-512-5796-3000   F: +86-512-5796-3300

NSK (CHINA) INVESTMENT CO., LTD.
JIANGSU ☆   No.8 NSK Rd., Huaqiao Economic Development Zone, Kunshan, Jiangsu, China (215332)
P: +86-512-5796-3000   F: +86-512-5796-3300

BEIJING   Room 1906, Beijing Fortune Bldg., No.5 Dong San Huan Bei Lu, Chao Yang District,
Beijing, China (100004)
P: +86-10-6590-8161   F: +86-10-6590-8166

TIAN JIN   Unit 4604, 46/F., Metropolitan Tower, 183 Nanjing Road, Heping District,
Tianjin, China (300051)
P: +86-22-8319-5030   F: +86-22-8319-5033

CHANGCHUN   Room 902-03, Changchun Hongwell International Plaza, No.3299 Renmin Street,
Changchun, Jilin, China (130061)
P: +86-431-8898-8682   F: +86-431-8898-8670

SHENYANG   No.7, 15 Street, Shenyang Economic & Technological Development Area,
Shenyang, Liaoning, China (110141)
P: +86-24-2550-5017   F: +86-24-2334-2058

DALIAN   Room 1805 Xiwang Tower, No.136 Zhongshan Road,
Zhongshan District, Dalian, Liaoning, China (116001)
P: +86-411-8800-8168   F: +86-411-8800-8160

NANJING   Room A1 22F, Golden Eagle International Plaza, No.89 Hanzhong Road, Nanjing,
Jiangsu, China (210029)
P: +86-25-8472-6671   F: +86-25-8472-6687

FUZHOU   Room 1801-1811, B1#1A Class Office Building, Wanda Plaza, No.8 Aojiang Road,
Fuzhou, China (350009)
P: +86-591-8380-1030   F: +86-591-8380-1225

WUHAN   Room 1512, No.198Yuncai Road, Office Building, Oceanwide City Square,
JiangHan, District, WuHan, China (400039)
P: +86-27-8556-9630   F: +86-27-8556-9615

QINGDAO   Room 802, Farglory International Plaza, No.26 Xianggang Zhong Road, Shinan District,
Qingdao, Shandong, China (266071)
P: +86-532-5568-3877   F: +86-532-5568-3876

GUANGZHOU   Room 1011-16, Yuexiu Financial Tower, No.28 Zhujiang Road East, Zhujiang
New Town, Guangzhou, Guangdong, China (510627)
P: +86-20-3817-7800   F: +86-20-3786-4501

CHANGSHA   Room 3209, Huayuan International Center, No.36, Section 2, Xiangjiang Middle
Road, Tianxin District, Changsha, Hunan, China (410002)
P: +86-731-8571-3100   F: +86-731-8571-3255

LUOYANG   Room 955, HUA-YANG PLAZA HOTEL, NO.88 Kaixuan W.Rd., Jian Xi District,
Luoyang,Henan Province, China (471003)
P: +86-379-6069-6188   F: +86-379-6069-6180

XI'AN   Room 1007, B Changan Metropolis Center, No.88 Nanguanzheng Steet, Xi'an,
Shanxi, China (710068)
P: +86-29-8765-1896   F: +86-29-8765-1895

CHONGQING   Room 612, Commercial Apartment, Athestel Hotel, No.288, Keyuan Rd.4,
Jiulongpo District, Chongqing, China (400039)
P: +86-23-6806-5310   F: +86-23-6806-5292

CHENGDU   Room1117, Lippo Tower, No.62 North Kehua Road, Chengdu, Sichuan, China (610041)
P: +86-28-8528-3680   F: +86-28-8528-3690

NSK CHINA SALES CO., LTD.
JIANGSU   No.8 NSK Rd., Huaqiao Economic Development Zone, Kunshan, Jiangsu, China (215332)
P: +86-512-5796-3000   F: +86-512-5796-3300

NSK HONG KONG LTD.
HONG KONG ☆   Suite 705, 7th Floor, South Tower, World Finance Centre, Harbour City, T.S.T,
Kowloon, Hong Kong, China
P: +852-2739-9933   F: +852-2739-9323

SHENZHEN   Room 624-626, 6/F, Kerry Center, Renminnan Road, Shenzhen, Guangdong, China
P: +86-755-25904886   F: +86-755-25904883

Taiwan:
TAIWAN NSK PRECISION CO., LTD.
TAIPEI ☆   10F-A6, No.168, Sec.3, Nanjing East Rd., Zhongshan Dist., Taipei City 104,
Taiwan
P: +886-2-2772-3355   F: +886-2-2772-3300

TAICHUNG   3F. -2, No. 540, Sec. 3, Taiwan Blvd., Xitun Dist., Taichung City 407, Taiwan
P: +886-4-2708-3393   F: +886-4-2708-3395

TAINAN   Rm. A1, 9F., No.189, Sec. 1, Yongfu Rd., West Central Dist., Tainan City 700,
Taiwan
P: +886-6-215-6058   F: +886-6-215-5518

India:
NSK BEARINGS INDIA PRIVATE LTD.
CHENNAI ☆   TVH Beliciaa Towers, 2nd Floor, Block I, No.71/1, MRC Nagar Main
Road, MRC Nagar, Chennai, Tamil Nadu, India - 600028
P: +91-44-28479600

GURGAON   Unit No. 202, 2nd Floor, 'A' Block, Iris Tech Park, Sector-48, Sohna Road,
Gurgaon, Haryana, India-122018
P: +91-124-4838000

MUMBAI   91 Spring Board Business Hub Private Limited, Godrej & Boyce, Gate No 2,
Plant No 6, LBS Marg, Opposite Vikhroli Bus Depot, Vikhroli West, Mumbai,
Maharashtra 400079, India
P: +91-9987617968

JAMSHEDPUR 36, Maharani Mansion Ground Floor, Circuit House Area P.O.- Bistupur, East
Singhbhum, Jamshedpur, Jharkhand, India-831011
P: +91-657-2421144

Indonesia:
PT. NSK INDONESIA
JAKARTA   Summitmas II, 6th Floor, Jl. Jend Sudirman Kav. 61-62, Jakarta 12190, Indonesia
P: +62-21-252-3458   F: +62-21-252-3223

Korea:
NSK KOREA CO., LTD.
SEOUL   Posco Center (West Wing) 9F, 440, Teheran-ro, Gangnam-gu,
Seoul, 06194, Korea
P: +82-2-3287-0300   F: +82-2-3287-0345

Malaysia:
NSK BEARINGS (MALAYSIA) SDN. BHD.
SHAH ALAM ☆   No. 2, Jalan Pemaju, U1/15, Seksyen U1, Hicom Glenmarie Industrial Park,
40150 Shah Alam, Selangor, Malaysia
P: +60-3-7803-8859   F: +60-3-7806-5982

PRAI   No.24, Jalan kikik, Taman Inderawasih, 13600 Prai, Penang, Malaysia
P: +60-4-3902275   F: +60-4-3991830

JOHOR BAHRU   88 Jalan Ros Merah 2/17, Taman Johor Jaya, 81100 Johor Bahru, Johor, Malaysia
P: +60-7-3546290   F: +60-7-3546291

IPOH   No.10&10A, Jalan Industri Paloh, Kawasan Perindustrian Ringan Paloh,
30200 Ipoh, Perak,Malaysia
P: +60-5-2555000   F: +60-5-2553373

Philippines:
NSK REPRESENTATIVE OFFICE
MANILA   8th Floor The Salcedo Towers 169 H.V. Dela Costa St.,Salcedo Villege Makati
City, Philippines 1227
P: +63-2-893-9543   F: +63-2-893-9173

Singapore:
NSK INTERNATIONAL (SINGAPORE) PTE LTD.
SINGAPORE   238A, Thomson Road, #24-01/05, Novena Square Tower A, Singapore 307684
P: +65-6496-8000   F: +65-6250-5845

Thailand:
NSK BEARINGS (THAILAND) CO.,LTD.
BANGKOK   26 Soi Onnuch 55/1 Pravet Subdistrict, Pravet District, Bangkok 10250, Thailand
P: +66-2320-2555   F: +66-2320-2826

Vietnam:
NSK VIETNAM CO., LTD.
HANOI   Techno Center, Room 204-205, Thang Long Industrial Park, Dong Anh District,
Hanoi, Vietnam
P: +84-24-3955-0159   F: +84-24-3955-0158

NSK REPRESENTATIVE OFFICE
HO CHI MINH CITY   Unit 609, The Landmark Building, 5B Ton Duc Thang Street,District 1,
Ho Chi Minh City, Vietnam
P: +84-28-3822-7907   F: +84-28-3822-7910

Worldwide Sales Offices

●Europe

United Kingdom:
NSK EUROPE LTD. (EUROPEAN HEADQUARTERS)
MAIDENHEAD   Belmont Place, Belmont Road, Maidenhead, Berkshire SL6 6TB, U.K.
P: +44-1628-509-800   F: +44-1628-509-808

NSK UK LTD.
NEWARK   Northern Road, Newark, Nottinghamshire NG24 2JF, U.K.
P: +44-1636-605-123   F: +44-1636-605-000

France:
NSK FRANCE S.A.S.
PARIS   Quartier de l'Europe, 2 Rue Georges Guynemer, 78283 Guyancourt, France
P: +33-1-30-57-39-39   F: +33-1-30-57-00-01

Germany:
NSK DEUTSCHLAND GMBH
DUSSELDORF ☆   Harkortstrasse 15, D-40880 Ratingen, Germany
P: +49-2102-4810   F: +49-2102-4812-290

STUTTGART   Liebknechtstrasse 33, D-70565 Stuttgart-Vaihingen, Germany
P: +49-711-79082-0   F: +49-711-79082-289

WOLFSBURG   Tischlerstrasse 3, D-38440 Wolfsburg, Germany
P: +49-5361-27647-10 F: +49-5361-27647-70

Italy:
NSK ITALIA S.P.A.
MILANO   Via Garibaldi 215, Garbagnate Milanese (Milano) 20024, Italy
P: +39-299-5191   F: +39-299-025778

Netherlands:
NSK EUROPEAN DISTRIBUTION CENTRE B.V.
TILBURG   Brakman 54, 5047 SW Tilburg, Netherlands
P: +31-13-4647647   F: +31-13-4641082

Poland:
NSK POLSKA SP.Z O.O.
WARSAW   Ul. Migdalowa 4/73, 02-796, Warsaw, Poland
P: +48-22-645-1525   F: +48-22-645-1529

Spain:
NSK SPAIN S.A.
BARCELONA   C/Tarragona, 161 Cuerpo Bajo, 2a Planta, 08014, Barcelona, Spain
P: +34-93-289-2763   F: +34-93-433-5776

Turkey:
NSK RULMANLARI ORTA DOGU TIC. LTD. STI.
ISTANBUL   Cevizli Mahallesi. D-100 Güney Yanyolu, Kuriş Kule İş Merkezi No:2 Kat:4, P.K.:
34846, Cevizli-Kartal-Istanbul, Turkey
P: +90-216-5000-675 F: +90-216-5000-676

United Arab Emirates:
NSK BEARINGS GULF TRADING CO.
DUBAI   JAFZA View 19, Floor 24 Office LB192402/3, PO Box 262163, Downtown Jebel Ali,
Dubai, U.A.E
P: +971-(0)4-804-8200   F: +971-(0)4-884-7227

●North and South America

United States of America:
NSK AMERICAS, INC. (AMERICAN HEADQUARTERS)
ANN ARBOR   4200 Goss Road, Ann Arbor, Michigan 48105, U.S.A.
P: +1-734-913-7500   F: +1-734-913-7511

NSK CORPORATION
ANN ARBOR   4200 Goss Road, Ann Arbor, Michigan 48105, U.S.A.
P: +1-734-913-7500   F: +1-734-913-7511

NSK PRECISION AMERICA, INC.
FRANKLIN ☆   3450 Bearing Drive, Franklin, Indiana 46131, U.S.A.
P: +1-317-738-5000   F: +1-317-738-5050

SAN JOSE   780 Montague Expressway, Suite 505, San Jose, California, 95131, U.S.A.
P: +1-408-944-9400   F: +1-408-944-9405

NSK LATIN AMERICA, INC.
MIAMI   11601 NW 107 Street, Suite 200, Miami Florida, 33178, U.S.A.
P: +1-305-477-0605   F: +1-305-477-0377

Canada:
NSK CANADA INC.
TORONTO ☆   317 Rutherford Road South, Brampton, Ontario, L6W 3R5, Canada
P: +1-888-603-7667   F: +1-905-890-1938

MONTREAL   2150-32E Avenue Lachine, Quebec, Canada H8T 3H7
P: +1-514-633-1220   F: +1-800-800-2788

Argentina:
NSK ARGENTINA SRL
BUENOS AIRES   Garcia del Rio 2477 Piso 7 Oficina "A" (1429) Buenos Aires-Argentina
P: +54-11-4704-5100   F: +54-11-4704-0033

Brazil:
NSK BRASIL LTDA.
SUZANO ☆   Av. Vereador João Batista Fitipaldi, 66, Vila Maluf, Suzano-SP-Brazil-CEP 08685-000
P: +55-11-4744-2500

JOINVILLE   Rua Blumenau, 178, sala 910, Centro, Joinville-SC-Brazil-CEP 89204-250
P: +55-47-3422-2239

Peru:
NSK PERU S.A.C.
LIMA   Calle Teniente Enrique Palacios 360 Oficina 311 Miraflores, Lima, Peru
P: +51-493-4385

Mexico:
NSK RODAMIENTOS MEXICANA, S.A. DE C.V.
SILAO, GUANAJUATO   Circuito Mexiamora Oriente No. 331, Parque Industrial Santa Fe I, Puerto
Interior, Silao, Guanajuato, Mexico, C.P. 36275
P: +52-472-500-9500   F: +52-472-103-9403

Motion & Control

No. 35 June 2024

Published by NSK Ltd.